

AD-A265 415



2

①

**Microinstabilities in High-Power MPD Systems: Preliminary
Diagnostics**

Erik C. Bowman

In fulfillment of the requirements of AAE 590 for the Masters of
Science.

School of Aeronautical and Astronautical Engineering
Purdue University, West Lafayette, IN 47907
9 Dec 1992

DTIC
ELECTE
JUN 07 1993
S E D

Prof. S.N.B Murthy
Co-Chair

Prof. Stephen Heister
Co-Chair

Prof. W.A. Gustafson
Committee Member

STRIPED STATEMENT
Approved for public release
Distribution Unlimited


DISCLAIMER NOTICE



THIS DOCUMENT IS BEST QUALITY AVAILABLE. THE COPY FURNISHED TO DTIC CONTAINED A SIGNIFICANT NUMBER OF COLOR PAGES WHICH DO NOT REPRODUCE LEGIBLY ON BLACK AND WHITE MICROFICHE.

REPORT DOCUMENTATION PAGE

Form Approved
DATE NO. 01-4-0188

1. AGENCY USE ONLY (Leave blank)		2. REPORT DATE 9 Dec 1992	3. REPORT TYPE AND DATES COVERED THESIS/DOSSERTATION	
4. TITLE AND SUBTITLE Microinstabilities in High-Power MPD Systems: Preliminary Diagnostics			5. FUNDING NUMBERS	
6. AUTHOR(S) Erik, C. Bowman, 2nd Lt				
7. PERFORMING ORGANIZATION NAME(S) AND ADDRESS(ES) AFIT Student Attending: Purdue University			8. PERFORMING ORGANIZATION REPORT NUMBER AFIT/CI/CIA- 92-137	
9. SPONSORING/MONITORING AGENCY NAME(S) AND ADDRESS(ES) AFIT/CI Wright-Patterson AFB OH 45433-6583			10. SPONSORING/MONITORING AGENCY REPORT NUMBER	
11. SUPPLEMENTARY NOTES				
12a. DISTRIBUTION/AVAILABILITY STATEMENT Approved for Public Release IAW 190-1 Distribution Unlimited MICHAEL M. BRICKER, SMSgt, USAF Chief Administration			12b. DISTRIBUTION CODE	
13. ABSTRACT (Maximum 200 words)				
<div style="text-align: right;"> 93-12644  171pk </div>				
14. SUBJECT TERMS 93 6 04 070			15. NUMBER OF PAGES 98	
			16. PRICE CODE	
17. SECURITY CLASSIFICATION OF REPORT	18. SECURITY CLASSIFICATION OF THIS PAGE	19. SECURITY CLASSIFICATION OF ABSTRACT	20. LIMITATION OF ABSTRACT	

Microinstabilities in High-Power MPD Systems: Preliminary
Diagnostics

Erik C. Bowman

In fulfillment of the requirements of AAE 598 for the Masters of
Science.

School of Aeronautical and Astronautical Engineering
Purdue University, West Lafayette, IN 47907

9 Dec 1992

Accession For	
NTIS CRA&I	<input checked="checked" type="checkbox"/>
DTIC TAB	<input type="checkbox"/>
Unannounced	<input type="checkbox"/>
Justification	
By	
Distribution /	
Availability Codes	
Dist	Avail and/or Special
A-1	

DTIC QUALITY INSPECTED 2

Abstract

The saturation of microinstabilities has been theorized to cause anomalous transport in MPD thrusters. However, calculation of anomalous transport properties is an area which is still in its infancy. It is the object of this paper to discuss the importance of anomalous transport in MPD thruster operation, how microinstabilities are related to anomalous transport, the types of microinstabilities most likely to occur, and at what locations in the MPD thruster. First, preliminary measurements were made of mean plasma properties and fluctuations using imbedded probe techniques in the plume and internal locations of a MW level MPD thruster operating near, but below, global onset conditions using probe techniques. Analysis of these results as well as significant incidental results are discussed. Next, a kinetic theory method for calculating plasma transport properties in a two-temperature, multiple species, non-equilibrium plasma has been modified to account for anomalous transport. The differences between transport coefficients calculated using that method and a method based on the mean free path formula for conductivity have been compared. In addition, as an illustrative example of application of the kinetic method, anomalous and classical properties have been calculated at different spatial locations in the MW level MPD thruster plasma using the mean plasma properties acquired through measurements in the preliminary experiments.

The experimental results did not show oscillations to support the presence of microinstabilities with characteristic frequencies near the lower hybrid frequency, which, theoretically, should have been present. However, much lower frequency oscillations were observed, which have been theorized to be associated with the onset phenomenon. In addition, the insertion of the Langmuir probe into the thruster current path appeared to induce onset at operating conditions where onset should not normally occur. Based on the measured mean plasma properties in the MW thruster, the computational work shows that anomalous conductivity does not appear to be as significant as previously suspected. This difference appears to stem from the inclusion of more particle interactions in the kinetic model, specifically electron-electron interactions.

Acknowledgements

First, I would like to express my appreciation to my primary research advisor, Professor S.N.B. Murthy, for not only clarifying concepts in our discussions, but more importantly, showing me how little I really knew; as a result, I delved deeper into my weaker areas. Also, I would like to thank Mr. Dennis Tilley, my experimental partner, not only for helping me with my experimental work, but for being a great "quick reference guide" when I could not understand something relating to microinstabilities. Thanks also go to Professor Stephen Heister, my other advisor who gave some unique insights into problem-solving through other areas. In addition, I would like to thank Professor W. A. Gustafson, who improved my understanding of high temperature gas dynamics immensely.

Of course, I would like to thank my Mom and the rest of my family and friends. Although they did not really understand what I was doing, they gave me much needed moral support when I was away doing research and also during my more humbling experiences at Purdue University.

This material is based upon work supported under a National Science Foundation Research Fellowship, while I was an officer in the United States Air Force. I would like to thank the National Science Foundation and the U.S. Air Force for allowing me the opportunity to earn the Masters of Science degree.

Table of Contents

Abstract	i
Acknowledgements	ii
List of Tables and Figures	v
Nomenclature	vii
I. Introduction	1
I.1 Definition of Microinstability	4
I.2 Previous Work	6
I.3 Thruster efficiency	7
I.4 Saturating Instabilities	10
I.5 Outline of Report	14
II. Classifications of Microinstabilities	16
II.1 Description of Relevant Microinstabilities	17
II.1.1 Electron Acoustic Instability (EAI)	17
II.1.2 Ion Acoustic Instability (IAI)	18
II.1.3 Electron Cyclotron Drift Instability (ECDI)	19
II.1.4 Drift Cyclotron Instability (DCI)	20
II.1.5 Generalized Lower Hybrid Drift Instability	21
(GLHDI)	
II.1.5.1 Lower Hybrid Drift Instability (LHDI)	22
II.1.5.2 Modified Two Stream Instability (MTSI)	22
II.1.6 Two Stream or Bunemann Instability (TSI)	24
II.2 Linearized Dispersion Relation	24
II.3 Relations between Microinstabilities	28
III. Experimental Work	33
III.1 Data Acquisition	33
III.1.1 Characterization of Thruster Performance	33
III.1.2 Testing	37
III.1.3 Probes	38
III.1.3.1 Magnetic Probes	38
III.1.3.2 Langmuir Probes	39
III.1.4 Calibration	41
III.2 Measurements	41
III.2.1 Magnetic Field	41
III.2.2 Langmuir Probe Measurements	44

III.2.2.1 Number density fluctuations	44
III.2.2.2 Mean Plasma properties	46
III.3 Interpretation of Results	48
III.3.1 Magnetic Field	48
III.3.2 Langmuir Probe	50
IV. Calculation of Plasma Transport Properties	67
IV.1 Bose Method	67
IV.2 Caldo-Choueiri Model	70
IV.3 Modification of Code	71
IV.4 Comparison of Results	75
IV.4.1 Comparison between mean free path and Bose methods	75
IV.4.2 Illustrative example	82
V. Discussion and Recommendations	90
V.1 Tentative Conclusions	90
V.2 Recommendations	91
References	95
Appendices	
A. Facility	
B. Magnetic Probe Theory	
C. Langmuir Probe Theory	
D. Documentation for Computer Code	

List of Tables and Figures

Tables

Table III.1: Characteristic frequencies.	55
Table III.2: Mean plasma properties.	56

Figures

Figure I.1: Schematic depiction of self-field MPD thruster operation.	2
Figure II.1: Enclosed current contours for operation at 6.8 kA and 2 g/sec mass flow.	31
Figure II.2: Pictorial depiction of microinstabilities existing in parameter space.	32
Figure III.1: Gas pulse with spark trigger.	57
Figure III.2: Sample current and voltage traces before and after onset.	58
Figure III.3: V-I curve (good data)	59
Figure III.4: Thruster test pattern	60
Figure III.5: Sample magnetic probe voltage trace	61
Figure III.6: Spatial map of average magnetic field with contours for 6.8 kA of current.	62
Figure III.7: Sample high frequency oscillation signal from the triple Langmuir probe.	63
Figure III.8: Sample probe voltage and current traces (absolute values).	64
Figure III.9: Contour map of electron temperature for a current of 6.8 kA.	65
Figure III.10: Contour map of electron number density at a current of 6.8 kA.	66
Figure IV.1: Electrical conductivity vs. electron temperature for a one temperature plasma at a pressure of 10 Pa.	86
Figure IV.2: Ratio of effective/classical electrical conductivity vs. electron temperature for both the Bose and mean free path methods.	86

Figure IV.3: Electrical conductivity vs. Hall parameter for a one temperature plasma at a pressure of 10 Pa.	87
Figure IV.4: Ratio of effective/classical conductivity vs. Hall parameter for pressure = 10 Pa, single temperature plasma at 31500 K.	87
Figure IV.5: Classical electrical conductivities vs. ratio of electron to heavy particle temperature by both the Bose method and mean free path method	88
Figure IV.6: Effective electrical conductivity vs. ratio of electron to heavy particle temperature by both the Bose and mean free path methods.	88
Figure IV.7: Ratio of effective to classical electrical conductivity vs. ratio of electron to heavy particle temperature.	89
Figure A.1; Diagram of MPD facility.	A-7
Figure A.2: Schematic of pulse forming network.	A-8
Figure A.3: Self-field MPD thruster	A-9
Figure C.1: Schematic diagram of Langmuir probe electrodes and potentials.	C-11

Nomenclature

A_{eff}	effective cross sectional area
A_j	Area of electrode j
B	magnetic field
B_z	Coefficient in Peterson-Talbot Curve fit
B_θ	magnetic field in azimuthal direction
B_\perp	magnetic field strength perpendicular to probe cross-section
b	electromagnetic thrust coefficient $= \frac{\mu_0}{4\pi} \ln \frac{r_a}{r_c}$
$[D_{ee}]_4$	fourth order electron-electron diffusion coefficient
E	electric field
E_1	first order electric field perturbation
e	charge of an electron
F	Force
I	total input current
I_{ij}	ion current to electrode j
I_{probe}	current coming from triple Langmuir probe
I_{ion}	current required for full ionization
J_{e0}	electron current at sheath edge $= n_e e \sqrt{\frac{KT_e}{2\pi m_e}}$
J_i	ion flux at electrode surface = $\exp(-0.5) en_e \sqrt{\frac{KT_e}{M_i}}$
K	Boltzmann Constant
k	wave number
k_z	component of wave number in direction of magnetic field

(l, s)	Notation used in Hirschfelder [47] to denote angular and speed dependence for the evaluation of omega integrals used in collision cross sections. It represents deviations from a rigid sphere model.
L_y	gradient length scale
L_p	Length of probe
M	atomic mass
\dot{m}	mass flow of propellant
m_e	mass of an electron
M_i	mass of an ion
n	total number density
$ n $	harmonic number
n_0	equilibrium number density
n_e	electron number density
n_i	ion number density
n_s	species number density
p	total plasma pressure
$Q^{(l,s)}_{cl}$	experimentally determined deviations from the rigid sphere model for "classical" cross sections.
$Q^{(l,s)}_{eff}$	cross section representing a deviation from the rigid sphere model for the "effective" transport property
Q^{max}_{cl}	maximum classical cross section (rigid sphere model)
Q^{max}_{eff}	maximum "effective" cross section: $= Q^{max}_{cl} + Q^p_{AI}$

Q_{ex}^2	anomalous momentum exchange collision cross-section
$ q $	determinant of the Sonine polynomial expansion
$ q_{11} $	determinant of the first minor of the Sonine polynomial expansion
R	Radial distance from thruster axis
r_a	anode radius
r_c	cathode radius
r_{eL}	electron Larmor radius
r_{iL}	ion Larmor radius
r_p	radius of probe
S	separation distance between probe wires
T_e	electron translational temperature
T_h	Heavy Particle translational temperature
T_i	Ion translational temperature
U_{e0}	electron drift velocity
U_{i0}	ion drift velocity
V	Volume
V_{12}	Potential difference between electrodes 1 and 2
V_{13}	Potential difference between electrodes 1 and 3
V_i	induced voltage
V_j	potential of electrode j
V_p	plasma potential
V^{tot}	total input voltage
v_0	relative drift velocity at equilibrium
v_{e1}	first order electron velocity perturbation

x

v_{i1}	first order ion velocity perturbation
v_s	species velocity
v_{si}	ion sonic velocity
v_{te}	electron thermal velocity
v_{ti}	ion thermal velocity
x	spatial position
x_e	electron mole fraction
Z_i	charge of ion
α	coefficient in Peterson-Talbot Curve fit
β	ratio of plasma pressure to magnetic pressure = $\frac{2\mu_0 nKT}{B^2}$
β_p	parameter for Peterson-Talbot Curve fit = $\frac{e\eta}{KT_e}$
$\Delta V_{cont.}$	contact potential difference
ϵ_0	permittivity of free space
e_i	ionization potential
ϕ	dimensionless voltage = $\frac{V}{V_{fi}^{emf}}$
Λ	maximum impact parameter
λ	mean free path
λ_d	debye length
λ_{de}	electron debye length
λ_{ii}	ion-ion mean free path
ν_e	electron collision frequency
$(\nu_e)^P_{AN}$	anomalous momentum exchange collision frequency
ν_{eH}	electron-heavy particle collision frequency

ν_{ei}	electron-ion collision frequency
Ω_e	electron Hall parameter
ω_{ce}	electron cyclotron frequency
ω_{LH}	lower hybrid frequency
ω_p	overall plasma frequency
ω_{pe}	electron plasma frequency
σ	electrical conductivity
σ_c	classical electrical conductivity
σ_{eff}	effective electrical conductivity
τ	end effect parameter = $\frac{L_p}{r_p} \sqrt{\frac{\epsilon_0 K T_e}{M_i}} \frac{1}{U_{di}}$
μ	magnetic permeability constant
μ_0	permeability of free space
θ	angle of propagation with respect to magnetic field
χ_j	dimensionless potential of electrode j = $\frac{e(V_j - V_p)}{K T_e}$
χ_{d2}	dimensionless potential between electrodes 1 and 2
χ_{d3}	dimensionless potential between electrodes 1 and 3
χ_f	dimensionless floating potential
ξ	dimensionless total current = $\frac{I}{I_{fi}}$
η	thruster efficiency
η_{probe}	parameter in probe curve fit - see eqns. (C.15-16)

I. INTRODUCTION

In the past, the movement of objects in the vacuum of space has relied on the use of chemical rocket engines. Unfortunately, the majority of the mass in a chemically propelled spacecraft consists of the chemical propellants themselves. In order to reduce the mass of the spacecraft without reducing thrust, the exhaust velocity of the exiting gases must be increased.

Currently, chemical rocket engines are limited to exhaust velocities between 4 and 5 km/sec due to temperature and pressure limitations on the combustion chambers, as well as the limitations on energy which propellants can add to the flow through exothermic chemical reactions. Thrusters using an external power supply to increase the thermal energy of the propellant are generally limited to exit velocities of 10 km/sec before temperatures threaten the structure of the engine [1].

However, if electromagnetic body forces are used to accelerate the propellant instead of the conventional means of heating and expanding through a nozzle, exhaust velocities an order of magnitude greater than chemical or electrothermal devices are possible. One type of device which uses electromagnetic body forces to produce thrust is the self-field magnetoplasmadynamic (MPD) thruster.

Figure I.1 shows a schematic depiction of a self-field MPD thruster. The self-field thruster is very simple in its basic design. Propellant is injected at the back of the thruster, and a high current electric arc is produced between a cathode and a

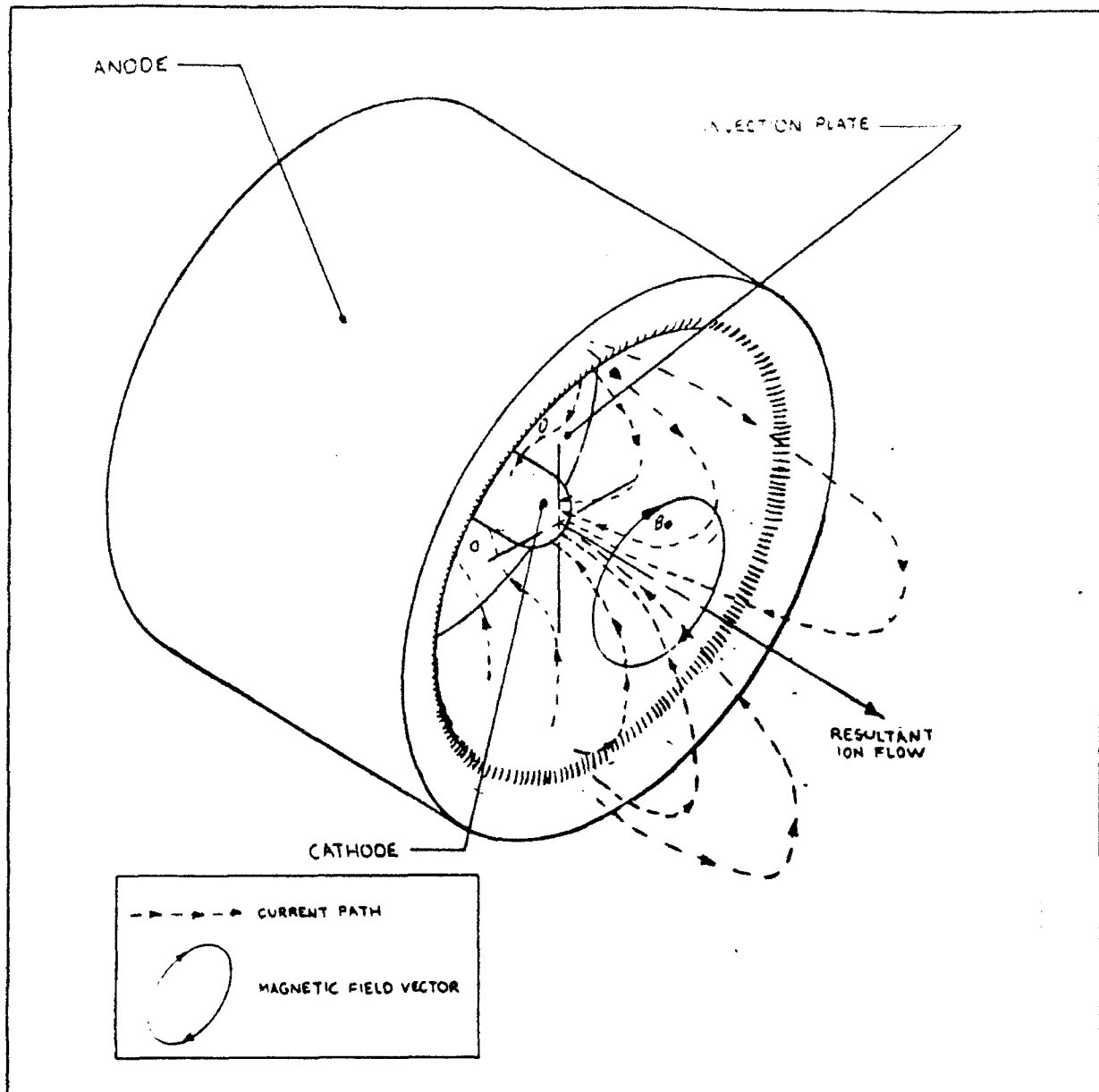


Figure I.1 - Schematic depiction of self-field MPD thruster operation.

coaxial anode. When the anode and cathode are coaxial, the current produces a magnetic field, B , primarily in the azimuthal direction while ionizing the propellant. As the current, I , travels radially, the $I \times B$ interaction provides an electromagnetic body force which accelerates the ionized plasma

in an axial direction while simultaneously pushing the plasma radially inward. This type of acceleration may also be referred to as Lorentz force acceleration [2]. The resultant exhaust velocities are in the range of 10-50 km/sec, depending on the current level and propellant used [3]. For a steady-state device, a separate power supply provides the current, while in the case of a quasi-steady thruster, a large capacitor bank provides the current. A quasi-steady, MW level self-field MPD thruster is the device examined in this research.

Currently, an MPD thruster has very low efficiencies, on the order of 30 per cent at most, where a minimum 60 per cent efficiency is required to make the MPD thruster competitive with propulsion systems currently in use [3]. What this means is that only 30 per cent of the input energy is becoming converted into directed kinetic energy, which is the energy used to produce thrust. The question is, what happens to the other 70 per cent of the energy? Recently, Choueiri, et. al. has suggested that a portion of the energy which is not converted into thrust provides the energy source for microscopic plasma instabilities, or microinstabilities [4].

The primary concern about microinstabilities is that they have been theorized to dictate anomalous transport. Anomalous transport may be defined as additional effects not accounted for in the classical kinetic theory of gases that increase such properties as viscosity, while decreasing others such as electrical conductivity. This anomalous transport leads to

electrical conductivity. This anomalous transport leads to undesirable plasma heating due to additional viscous dissipation, more ohmic heating, etc. As the MPD thruster uses primarily electromagnetic, rather than electrothermal energy, to provide thrust, the energy going into heating the plasma is essentially wasted. This wasted energy results in the very low efficiencies associated with the MPD thruster. It is hoped that a better understanding of microinstabilities will enable the scientific community to determine the significance of the impact which microinstabilities have on these energy losses.

I.1 Definition of Microinstability

An instability may be described as an oscillation or other disturbance in one or more parameters of a system that changes in time and space [2]. The progression of an instability is easy to understand in a continuum flow. For example, turbulent flow may be considered as resulting from an instability; eddies can be said to form and grow with time and distance downstream. Such descriptions of fluid turbulence are based on the existence of a continuum of particles. In contrast, a plasma can be considered as either a continuum when the plasma state is highly collisional, or it may be considered as a group of independent particles, for example when the plasma state indicates that it is collisionless. In the latter case, internal electric fields can play a role in creating and propagating disturbances.

A microinstability can be described simply as a plasma

instability that occurs on a very small scale. For continuum state instabilities, the smallest eddies are still much larger than a mean free path between molecular or atomic collisions; the eddies and their interactions can be considered to occur on a macroscopic scale. In a plasma, electric fields can play a role in instabilities. A plasma typically observes the quasi-neutrality condition, that is there are an equal number of negative and positive charges in a plasma and macroscopically the plasma appears to be neutral. However, because the charge in a plasma is associated with different species, there may be specific locations where effects due to a net electric field appear. These effects do not extend very far; they most likely occur only in small zones where there is a local charge separation. As a result, these effects occur on a length scale that is often less than the mean free path, λ [4], which is on the order of a millimeter for a plasma with a number density, n_e , of about 10^{19} m^{-3} and electron temperature, T_e , about 3 eV. This diminutive length scale gives microinstabilities their name.

One general class of microinstabilities is the category of streaming instabilities. A streaming instability may exist whenever a relative drift between different species occurs [6]. As the current which provides the electromagnetic acceleration also produces a relative drift between electrons and ions, streaming instabilities are expected to occur in the MPD thruster. A further discussion of streaming instabilities is presented in Chapter II.

I.2 Previous Work

Microinstabilities in $I \times B$ plasmas have been studied extensively by the plasma physics community [7]. Unfortunately, many of these works are not directly applicable to MPD devices because the plasma properties in other plasma devices differ significantly from the MPD thruster [1].

Initial work concerning the effects of instabilities in the MPD plasma concentrated primarily of the prediction of the phenomenon known as "onset". "Onset" is the operating point where various processes detrimental to the MPD thruster, such as cathode erosion, begin to occur. This point is defined as the global current and global voltage level above which high frequency terminal voltage fluctuations are observed, and this point scales with I^2/\dot{m} , where $\dot{m} \equiv$ mass flow of propellant[8,9]. Recently, macroscopic instabilities have been examined as the cause of onset [10-14], where a macroscopic electron acoustic instability [10] or a Pierce instability [13,14] appears to be responsible for onset. Experimentally, inconclusive attempts have been made to identify the instability associated with onset phenomenon by examining the power spectra of both terminal voltage and light intensity fluctuations[15].

In recent years, however, some emphasis has begun to be placed on the investigation of microinstabilities in MPD thrusters operating below the onset current level. Microinstabilities have been studied extensively for other plasma

devices[16-25], but recent work has focused on the theoretical identification of the various instabilities which may occur in the self-field MPD thruster [4,26,27] and the identification of the instability which dictates the anomalous transport properties (e.g. electrical conductivity, viscosity, thermal conductivity, etc.) in the plasma of the MPD thruster. At the time of this study, the generalized lower hybrid drift instability (GLHDI) has been linked to anomalous transport [4,28,29]. A more detailed discussion of the GLHDI, as well as other microinstabilities, is presented in Chapter II.

Experimental verification of both the presence of microinstabilities in the MPD thruster as well as a measurement of the linear dispersion relation of the GLHDI has also been attempted, most notably at Princeton University [1,4,30,31].

I.3 Thruster Efficiency

Before discussing the effects of microinstabilities on efficiency, it is first necessary to look at what defines efficiency. There are two modes of input energy conversion which operate in an electromagnetic thruster: plasma heating and electromagnetic power. Most of the electromagnetic power is converted into thrust with the exception of some undirected flow [2]. However, the plasma heating mode has very little of its portion of total energy go into the form of directed kinetic energy. The majority of the power input for heating is dissipated in electrode, plasma thermal, and internal mode

(vibration, ionization) losses, and also, in undirected kinetic energy [2]. Because the MPD thruster has a low operating pressure, the stabilizing effect of collisions is not readily available. Thus, the flow in a MPD thruster is in a highly non-equilibrium state, and this fact makes it much more difficult to convert heat into propulsive kinetic power [2]. As a result the MPD thruster efficiency becomes reduced. Meanwhile, the thermal energy which does not get converted into propulsive kinetic power serves as the energy source for microinstabilities. If the microinstabilities can be reduced, in principle, more energy will be available for conversion into directed kinetic energy.

Two methods can be used to increase the efficiency, assuming that electromagnetic power losses are negligible in comparison. One method is to try to increase the percentage of electrothermal thrust by incorporating such components as a thrust nozzle. This is attempted in hybrid arcjet-MPD thrusters. In the second method, the overall plasma heating is reduced. One means of accomplishing this is to control the occurrence of microinstabilities. By controlling the microinstabilities, the additional plasma heating associated with anomalous transport is reduced, thus decreasing the wasted input power.

Assuming an azimuthally symmetric, radial discharge, the thruster efficiency can be written as follows [2]:

$$\eta = \frac{1}{1 + \frac{2\dot{m}}{b^2 I^4} \int_V \frac{j^2}{\sigma} dV} \quad (I.1)$$

In the preceding equations, η = efficiency, σ = electrical conductivity, j = current density, V = volume (a volume integral), \dot{m} = mass flow and the electromagnetic thrust coefficient, b , is

$$b = \frac{\mu_0}{4\pi} \ln \frac{r_a}{r_c} \quad (I.2)$$

where r_a = radius of anode, r_c = radius of cathode, and μ_0 = permeability of free space. Considering the expression for efficiency, one can see that as σ decreases, the second term in the denominator, representing the increase in thermal energy due to ohmic heating, will increase, decreasing the efficiency. The classical value of electrical conductivity can be expressed by the mean free path formula:

$$\sigma_{cl} = \frac{e^2 n_e}{m_e \nu_{ei}} \quad (I.3)$$

where σ_{cl} = classical electrical conductivity, e = charge of an electron, m_e = mass of an electron, and ν_{ei} = electron-ion collision frequency.

The microinstabilities can be expected to alter the effective collision frequency, thereby causing changes in the

electrical conductivity. However, these instabilities will not grow indefinitely. Eventually, mechanisms appear which partially or totally drain the energy source fueling the instability. When this occurs, the plasma will reach a new state of equilibrium, and often this steady-state occurs so as to allow both the energy source and the sink (the instability) to exist simultaneously [2]. This new steady-state is known as saturation and is of a turbulent nature [2]. As linearized dispersion relations predict unlimited growth of the instability as time increases, to produce saturation a non-linear damping mechanism must be present which is not accounted for by linearized theory. One type of non-linear damping mechanism is a collision, and its effect is expressed in terms of the particle collision frequency. However, collisions are not always enough to stop the runaway growth of an instability. In that case, an interaction between the electric field produced by the unstable wave and a charged particle must provide the mechanism for saturation of the instability.

1.4 Saturating Instabilities

There are many possible mechanisms by which such saturation can occur. Three of the most common are quasilinear stabilization, saturation due to resonance broadening, and saturation due to electrostatic trapping. The first two are supposed to have a negligible effect on microinstabilities in an MPD thruster [4]. Electrostatic trapping can be described as the situation where a charged particle is travelling at a velocity

near the wave velocity and is trapped in a potential "well" of the wave. Any charged particle which is trapped is forced to slow down when it is travelling upwards in a potential "well", and increases in speed as it travels down the well. Some energy transfer occurs between the wave and particle, tending to equalize the two velocities [4]. One can think of a ball in a bowl. If the ball is let go near the top, it will roll almost as high up on the other side, and then roll back, and so on. Eventually the initial potential energy is dissipated through friction and the ball settles to the bottom of the bowl. In a similar manner, some of the particle excess energy is transferred to the wave, and vice versa in an oscillating manner, until eventually the particle velocity matches the wave phase velocity. In addition, the wave of one species acts on the other species in the plasma, effectively transferring energy from one particle to another. This may explain plasma heating: energetic electrons transfer their energy to ions through wave interactions as the instability saturates in an attempt to produce a plasma in thermal equilibrium.

In general, the effective collision frequency depends on the method of non-linear damping assumed to offset the linear growth. Choueiri has professed that if ion trapping is the method of damping, collision frequencies can be as much as two orders of magnitude higher than the classical collision frequency [4]. This is the mode of non-linear damping which he expects to produce anomalous transport in the MPD thruster [4]. On the

other hand, Choueiri has also shown that if resonance scattering or electron trapping is the damping method, the anomalous collision frequency can become much less than the classical value. Thus, the change in transport with these types of damping mechanisms becomes fairly insignificant [4].

Whichever type of non-linear damping mechanism is used to account for anomalous transport, the primary conditions under which the microinstability is expected to occur must be known. The ratio of electron drift velocity to ion thermal velocity is a key parameter in the conditions for the occurrence of microinstabilities [4,15]. As current increases above a critical value of electron drift to ion thermal velocity (about 1.5)[4,15], the collision frequency stays fairly constant. The mechanism of ion trapping is characterized more by the ratio of electron collision frequency over the lower hybrid frequency, or as the inverse of the Hall parameter scaled by the square root of the mass ratio. Thus, the high Hall parameter regions of the discharge are the regions where anomalous dissipation is more likely to occur [4]. One such region would be near the anode, where the number density, and consequently, collision frequency is much lower. The electron Hall parameter is defined as [19]:

$$\Omega_e \equiv \frac{\omega_{ce}}{v_{eH}} \quad (1.4)$$

where ω_{ce} = electron cyclotron frequency (hz), and v_{eH} = electron-heavy species collision frequency. Thus lower collision frequencies lead to higher hall parameters, which would result in

stronger anomalous transport effects due to ion trapping. It has also been found that collisional processes tend to disrupt these non-linear collisionless damping mechanisms, allowing ion-trapping also to produce effective collision frequencies below the classical value even in collision dominated regions [4].

The saturation of microinstabilities seems to be the major player in producing anomalous transport, and thus decreasing the plasma electrical conductivity below the classically predicted values. This reduced electrical conductivity produces a larger voltage drop for a given current, which means more power must be added to the system to keep it operating at its current level.

If the plasma is fully ionized, the ratio of electron drift velocity, U_{de} , to ion thermal velocity, v_{ti} , usually exceeds the threshold value of 1.5 for the occurrence of microinstabilities. Thus, another condition which for all practical purposes may be considered as a necessary, but not sufficient condition for the presence of microinstabilities, is that the plasma is fully ionized. Introducing the dimensionless total current[20]

$$\xi = \frac{I}{I_{fi}} \quad (1.5)$$

where I_{fi} = current required for full ionization of the plasma, microinstabilities may occur if $\xi > 1$ [20]. The utility of using this parameter is that the occurrence of microinstabilities can be predicted to some degree based on global parameters, expressed in an alternate form of (1.5)[4,20]:

In the above equation, e_i = ionization potential, M = atomic

$$\xi = \left(\frac{M}{2\epsilon_0} \right)^{\frac{1}{2}} \left[\frac{\mu}{4\pi m} \ln \frac{r_d}{r_p} \right]^{\frac{1}{2}} \quad (I.6)$$

mass, and μ is the magnetic permeability constant, which for all practical purposes is the permeability of free space [4]. An additional use of ξ is to determine how much voltage is required to produce electromagnetic acceleration. This relationship is expressed as:

$$\begin{aligned} &\text{for } \xi < 1, \phi \propto \xi \\ &\text{for } \xi > 1, \phi \propto \xi^3 \\ \phi &= V^{tot} / V_{emf}^{fi} \end{aligned} \quad (I.7)$$

where $V^{tot} \equiv$ total input voltage and $V_{emf}^{fi} \equiv$ the portion of total voltage which produces electromagnetic acceleration at a current of I_{fi} . As thrust scales linearly with current ($F \propto I \times B$), the more voltage which is required to produce that thrust causes the input power required to increase as well. Thus, an increase in input power without a corresponding increase in thrust will result in a lower thruster efficiency. Consequently, efficiency decreases as ξ increases above 1. Since microinstabilities are likely to occur when ξ is above 1, and efficiency drops at that condition as well, one may infer that microinstabilities may be a cause for the loss of engine efficiency once the plasma becomes fully ionized.

I.5 Outline of Report

The current investigation is designed to accomplish two major tasks: 1) To measure mean plasma properties and plasma

fluctuations to determine if and where microinstabilities appear in the thruster, and 2) to develop an improved method for calculation of anomalous transport properties based on mean plasma properties measured inside the thruster.

To accomplish these two tasks, experiments were performed on a MW level MPD device to gain spatial maps of the magnetic field, the electron number density, the electron temperature, and the relative magnitudes of electron number density oscillations. These measurements were obtained using magnetic and Langmuir probes to examine the possible occurrence of microinstabilities. The data also serves as inputs to a kinetic theory computer code for determining plasma transport properties taking into account microinstabilities, for example those that occur at the lower hybrid frequency.

Chapter II will discuss the types of microinstabilities which are expected to occur in an MPD thruster as well as discuss the relationships between them. Chapter III presents the results of experiments performed in a quasi-steady MW level self-field MPD device. Chapter IV examines the modification of a plasma transport code to account for anomalous transport, and conditions from two spatial locations determined through the experimental work discussed in chapter III are examined. Finally, chapter V discusses ways to improve the experiments and computer program, points out avenues of possible future research and draws some tentative conclusions from this work.

II. CLASSIFICATIONS OF MICROINSTABILITIES

There are several type of microinstabilities which may be present in an MPD plasma. The ones which are most likely to occur are those classified as cross-field microinstabilities [4]. The name cross-field is derived from the energy source for the instabilities, namely the current arc, which is generally perpendicular to the magnetic field in a self-field MPD thruster. The cross-field microinstabilities fall under the broader category of streaming instabilities. Streaming instabilities are caused either by a beam of energetic particles travelling through the plasma, or by a current driven through the plasma; both result in different species suffering drifts relative to each other. The drift energy (or current) provides the source for the instability. Experimental measurements have shown that the electron drift velocity, U_{de} , is typically 1-100 times larger than the ion thermal velocity, v_{ti} [31]. On this basis, it was assumed that current driven instabilities are the dominant instability in MPD thrusters [31]. The cross-field microinstabilities which are most likely to be observed are the electron-acoustic instability (EAI) (not to be confused with the macroscopic electron-acoustic instability which has been postulated by Rempfer, et. al. to play a role in onset phenomena[10]), ion-acoustic instability (IAI), electron-cyclotron drift instability (ECDI), drift-cyclotron instability (DCI), generalized lower hybrid drift instability (GLHDI), and the two-stream instability (TSI) (otherwise known as Bunemann or

hydrodynamic instability).

II.1 DESCRIPTION OF RELEVANT MICROINSTABILITIES

II.1.1 Electron acoustic instability (EAI)

The electron acoustic instability propagates longitudinally. Its direction of propagation and temperature operation regime is given by [4]:

$$\frac{T_i}{T_e} > 1 + \frac{k^2 \cos^2 \theta v_{ti}^2}{\omega_{UH}} \quad (\text{II.1})$$

where $\theta \equiv$ angle of propagation with respect to the magnetic field, $\omega_{UH} \equiv$ lower hybrid frequency, $k \equiv$ wave number, and $T_i \equiv$ ion temperature. In the limit of $\theta = \pi/2$ (propagation perpendicular to the magnetic field) this equation simplifies to $T_i/T_e \gg 1$. If the wave is propagating at an angle oblique to the magnetic field, the T_i/T_e value required for the existence of the instability must be even larger. Although it is possible that this mode could be present in extreme cases, it is not very likely to occur because in the MPD thruster T_e is on the order of T_i . In any event, this instability will not exist unless the dot product of the wave number and the electron drift velocity is less than zero[4,17].

$$\mathbf{k} \cdot \mathbf{U}_e < 0 \quad (\text{II.2})$$

In other words, the instability will only occur if the electrons flow in the opposite direction of the wave.

Examining figure II.1 to see the likely flow pattern of

current in the MPD thruster, one can see that for the instability to exist, the wave must have a component in the direction of the contour lines going from anode to cathode. As the instability propagates in a longitudinal, or acoustic, manner it can only propagate upstream at subsonic flow velocities. Because the ion drift velocity is hypersonic in the MPD thruster, the EAI is only expected in the inter-electrode space and near the anode. In any event, this instability is not likely to be observed because it is damped in most experimental situations [17].

II.1.2 Ion Acoustic Instability (IAI)

The ion-acoustic instability (IAI) occurs if [17]

$$\frac{KT_i}{KT_e} < 1 + k^2 r_{Le}^2 \quad (\text{II.3})$$

where $r_{Le} \equiv$ electron Larmor radius, and

$$\frac{U_{de}}{v_{si}} - 1 \geq \frac{k_z}{k} \left(\frac{T_e}{T_i} \right)^{\frac{1}{2}} \left(\frac{M_i}{m_e} \right)^{\frac{1}{2}} \alpha e^{-\left(\frac{T_e \alpha^2}{2T_i} \right)} \quad (\text{II.4})$$

$$\alpha = \left(1 + \frac{k^2 v_{te}^2}{\omega_{pe}^2} \right)^{-\frac{1}{2}}$$

where $v_{si} \equiv$ ion sonic velocity, $k_z/k \equiv$ cosine of angle of wave propagation with respect to magnetic field, $M_i \equiv$ mass of ion, $v_{te} \equiv$ electron thermal velocity, and $\omega_{pe} \equiv$ electron plasma frequency. In the limit of an infinitely strong magnetic field ($r_{Le} = 0$) the thermal criteria for existence of the instability reduces to

$T_e/T_i \ll 1$. If k_z/k is as small as $(m_e/M_i)^{1/2}$ (nearly perpendicular to the magnetic field) the condition for existence of the microinstability is $U_{de} \geq (1-2) v_{te}$ in the whole range $T_e \geq T_i$ [17]. This instability may occur in the MPD thruster although the thruster is considered largely isothermal because of an extreme sensitivity to the actual electron and ion temperature distributions. Due to lack of dependence on the direction of the drift velocities, theoretically it could occur anywhere in the thruster. Higher electron velocities are expected near the cathode, though, which makes the cathode the most likely region of existence of the IAI. However, like the electron-acoustic mode, the ion-acoustic mode is damped for most experimental situations, so it is unlikely to be seen in MPD plasmas.

II.1.3 Electron Cyclotron Drift Instability (ECDI)

The electron-cyclotron drift instability (ECDI) operates at discrete frequencies near the harmonics of the electron cyclotron frequency. The criteria for the instability to exist is [18]

$$k < |n| \frac{\omega_{ce}}{|U_{de}|} \quad (\text{II.5})$$

where $|n|$ = the number of the harmonic of the electron cyclotron frequency. This is the range where Bernstein harmonics have a negative energy. A Bernstein wave is an electrostatic wave which propagates perpendicular to the magnetic field at harmonics of the cyclotron frequencies, and there are both ion and electron modes of this wave. When this negative energy wave comes into

contact with a frequency resonance or sink to which it can lose its energy, an instability will result [18]. What happens, looking at the dispersion relation, is that the branch corresponding to Bernstein waves intersects the ion acoustic branch when the energy of the wave is negative. Thus, the instability will probably appear in the same regions as the IAI, namely in the cathode region. Lashmore-Davies gives a solution for the ECDI which is valid for [18]

$$kr_{De} > \frac{|n|^{\frac{1}{2}}}{(8\pi)^{\frac{1}{4}}} \left(\frac{M_i}{m_e} \right)^{\frac{1}{4}} \left(1 - \frac{k|U_{de}|}{n \omega_{ce}} \right)^{\frac{1}{2}} \quad (\text{II.6})$$

It has been theorized that these waves may be connected with anomalous resistivity [20]. Part of the problem associated with this instability is the non-linear mechanism which saturates the instability. It turns out that the collective friction force produced by the instabilities does not always stabilize them (e.g. for $U_{de} \gg v_{ti}$). Vortical instabilities in an electron gas and anomalous viscosity could be some means of saturation[20].

II.1.4 Drift Cyclotron Instability (DCI)

The drift-cyclotron instability (DCI), first considered by Mikhailovsky and Timofeev [16], is caused by gradients in the plasma properties, and operates at discrete frequencies near the ion cyclotron frequency. Because it is gradient driven, one might be tempted to classify this microinstability as a Rayleigh-Taylor instability. However, the instability energy source is

the cross-field current, not a non-electromagnetic body force; therefore, it still falls under the category of streaming instabilities. The instability exists if [23]:

$$\frac{U_{di}}{v_{ti}} \geq \sqrt{\frac{2m_e}{M_i}} \quad (\text{II.7})$$

where U_{di} = ion drift velocity. Thus, this instability would most likely exist where the ion drift velocity is relatively high, such as near the thruster exit plane and out into the plume. Finite β (ratio of plasma pressure to magnetic pressure) increases the frequency and decreases the growth rate but does not completely stabilize the instability. When

$$\frac{r_{Li}}{L_N} \geq \left(\frac{m_e}{M_i} \right)^{\frac{1}{4}} \quad (\text{II.8})$$

where r_{Li} = ion larmor radius and L_N = length scale of density gradient, the DCI transitions to become the lower hybrid drift instability (LHDI), or the lower hybrid gradient driven instability (LHGDI), discussed in the next section.

II.1.5 Generalized Lower Hybrid Drift Instability (GLHDI)

The generalized lower hybrid drift instability (GLHDI) actually incorporates other microinstabilities as limiting cases. This instability can occur at relatively low U_{de} and operates near the lower hybrid frequency. This instability is thought to be the primary reason for anomalous resistivity, and thus turbulent plasma heating. The general solution does not have an

analytic representation for the range of stability. Therefore, the limiting cases will be discussed.

II.1.5.1 Lower Hybrid Drift Instability (LHDI)

The lower hybrid drift instability (LHDI), alternatively named as the lower hybrid gradient driven instability (LHGDI) by Choueiri [2,4] occurs when gradients in the plasma parameters (inhomogeneities) exist. Numerically, this exists as k_z goes to zero and $|U_{\phi e} - U_{\phi i}|$ goes to zero [24]. In other words, the waves in this instability travel in a "flute" mode, perpendicular to the local magnetic field vector. Thus, in the MPD thruster, one would expect to see this instability near the cathode where the electrons and ions move roughly in the same direction. The primary gradients responsible for this instability are density, temperature, and magnetic field gradients. The instability itself can be attributed to a coupling between a negative energy drift wave and positive energy lower hybrid wave for moderate gradients, and by an inverse Landau damping caused by a resonance between the drift wave and ions which are near the drift wave velocity for strong gradients [4]. This instability's length scale is on the order of an electron larmor radius [4].

II.1.5.2 Modified two-stream instability (MTSI)

The modified two-stream instability (MTSI), alternatively named as the lower hybrid current driven instability (LHCDI) by Choueiri [2,4], is the instability which results due to a

relative streaming of charged particles due to the $E \times B$ drift (E = electric field vector) or the presence of charged beams being the major source of free energy. This is also referred to as the kinetic cross-field streaming instability by Wu et. al [25]. Numerically, this case is represented as $d(\ln n)/dx$ goes to zero and $d(\ln B)/dx$ goes to zero, while $U_{ie} \gg v_{te}$. In the collisionless limit, this wave propagates at small but finite angles from the local perpendicular to the local magnetic field vector. In the MPD thruster, this translates into a wave which travels either radially or axially, but has a slight azimuthal component. The azimuthal component is on the order of the square root of the mass ratio times the perpendicular components. It most likely occurs near the anode region where density gradients and magnetic field gradients are small, but electron drift velocities are fairly high.

This instability does not depend on resonance between the wave and a small number of particles in the velocity distribution for the electrostatic limit, and it becomes more kinetic (resonant) in nature as electromagnetic effects becomes important (when Alfvén velocity is exceeded)[25]. The instability results from a coupling of the negative energy beam of particles and a positive energy lower hybrid wave. As electromagnetic effects become more important, a coupling with an electromagnetic mode, such as a whistler mode, may become significant[25]. Although it is damped by electromagnetic waves when operating below the Alfvén velocity, it is not stabilized when the drifts are above

this level.

Lastly, the instability's length scale is larger than the electron Larmor radius. This means that it is possible to measure the lower hybrid oscillations of this mode by a probe with dimensions smaller than an electron Larmor radius.

II.1.6 Two-stream instability (TSI)

The two-stream instability (TSI), or Bunemann instability, is actually a limiting case of the MTSI, but as it lends itself to discussion based on hydrodynamic as opposed to kinetic theory, it is discussed separately. It is the modified two-stream instability in unmagnetized plasmas or plasmas where the current is aligned with the magnetic field. For small β , if k_z is sufficiently large, a uniform magnetized plasma with a cross field drift will reduce to the unmagnetized case. In this case, the instability will operate near the electron plasma frequency if $kr_{De} \gg 1$ and $U_{de} > v_{te}$. Although this instability is not likely to be present in the MPD thruster due to the large azimuthal magnetic fields, its relative simplicity allows one to get a basic understanding of more complex microinstabilities. This instability is used to demonstrate the technique of linear analysis to determine dispersion relations in the next section.

II.2 Linearized derivation of dispersion relation

Considering a uniform plasma in which the ions are stationary and the electrons have drift velocity v_0 relative to

the ions, a dispersion relation may be deduced under the assumptions of a cold plasma ($KT = 0$ for both species, and no magnetic field. Starting with the equations of motion,

$$\begin{aligned} m_s \left[\frac{\partial \mathbf{v}_s}{\partial t} + (\mathbf{v}_s \cdot \nabla) \mathbf{v}_s \right] &= -en_s \mathbf{E} \\ \frac{\partial n_s}{\partial t} + \nabla \cdot (n_s \mathbf{v}_s) &= 0 \end{aligned} \quad (\text{II.9})$$

for both ions and electrons, where $n_0 \equiv$ equilibrium number density, $\mathbf{v}_s \equiv$ velocity vector of species s , $n_s \equiv$ number density of species s , and $\mathbf{E} \equiv$ electric field vector. Letting density, electric field and velocity of each species be represented by a sum of perturbation and equilibrium values, the gradient term in the ion equation is dropped since the ions are stationary. Also neglecting one of the two gradient terms because the equilibrium velocity, \mathbf{v}_{s0} , is uniform yields the linearized equations:

$$M_i n_0 \frac{\partial \mathbf{v}_{i1}}{\partial t} = en_0 \mathbf{E}_1 \quad (\text{II.10})$$

$$m_e n_0 \left[\frac{\partial \mathbf{v}_{e1}}{\partial t} + (\mathbf{v}_{e0} \cdot \nabla) \mathbf{v}_{e1} \right] = -en_0 \mathbf{E}_1 \quad (\text{II.11})$$

where $\mathbf{v}_{i1} \equiv$ first order ion velocity perturbation, $\mathbf{E}_1 \equiv$ first order electric field perturbation, and $\mathbf{v}_{e1} \equiv$ first order electron velocity perturbation. Looking for electrostatic waves of the form $e^{i(kx - \omega t)}$, where $\omega \equiv$ wave frequency and $i \equiv \sqrt{-1}$,

$$\frac{\partial}{\partial t} = -i\omega, \quad \nabla = ik \quad (\text{II.12})$$

Next, it is necessary to solve for both species density

perturbations and both species velocity perturbations. Since the instability causes high frequency plasma oscillations, the plasma approximation, that is $n_i = n_j$, cannot be used, which means Poisson's equation must be used instead:

$$\epsilon_0 \nabla \cdot \mathbf{E} = e(n_i - n_j) \quad (\text{II.13})$$

where ϵ_0 = permittivity of free space and n_i = ion number density. This equation must be linearized. Substituting the solutions for the densities and velocities evaluated earlier yields the dispersion relation.

$$1 = \omega_p^2 \left[\frac{M_j}{M_i} \frac{1}{\omega^2} + \frac{1}{(\omega - kv_0)^2} \right] \quad (\text{II.14})$$

where ω_p = overall plasma frequency.

If the dispersion relation is multiplied through to get a common denominator, a fourth order polynomial for ω results. Theoretically both k and ω could be complex. However, to find if a plasma is unstable one must first look at the situation. If the plasma merely exists, disturbance waves must be considered across a whole spectrum due to the randomness of nature; a specific disturbance cannot be readily predicted. Thus k is typically treated as an independent, real parameter, while ω is allowed to be complex. Solving the above equation, there can exist both real and imaginary roots of ω . If all the roots are real, no instability exists. However, if complex roots are present, they exist as complex conjugates. The conjugate with a negative imaginary term will indicate an exponentially damped

wave. The conjugate with a positive imaginary term will have an exponential growth. These two effects do not cancel out when added; all that is seen will be exponential growth. Thus, if complex roots exist, the plasma is unstable. As kv_j decreases there exists a point where it finally yields complex roots. What this translates to is that for the Bunemann instability, for sufficiently small kv_j , the plasma is unstable. This means that since wavelength is inversely proportional to k , for any given v_j , the plasma is unstable to long wavelength oscillations. If the plasma has a finite temperature, the fluid equations cannot be used to predict the instability; kinetic theory, however, can take into account finite temperature plasmas, although the analysis is also more complex. Kinetic theory predicts that Landau damping will occur for $v_j \leq$ thermal velocity, so no instability will exist if v_j is too small.

This instability can be physically explained as follows. Both electrons and ions have their own natural frequencies. What happens is that for the right value of kv_j , these frequencies coincide due to the doppler shift of the moving electron plasma fluctuations. Also, these electron oscillations have negative energy. In other words, the electrons have less kinetic energy when the oscillations occur than they did when they were absent. In contrast, the ions have positive energy, meaning they have more energy when the oscillations are present than when they are absent. What this means is that both waves can continue to grow while conservation of energy is satisfied because the total

energy remains constant.

As an aside, when a plasma is excited by a specific wavelength disturbance, say by a microwave beam, ω stays real, and k is considered to be complex. Thus if the imaginary part of k is positive, the wave will be damped, while if the imaginary part is negative, exponential growth will occur.

II.3 Relationships between Microinstabilities

Now that a foundation for a physical and mathematical understanding of what a microinstability has been laid, relationships may be explored. The GLHDI can be viewed as the most basic instability, where most of the other instabilities are special cases, depending on limits of key parameters. In fact, the most frequently cited frequencies of microinstabilities in the MPD thruster has been at the lower hybrid frequency [1,30]. The EAI may be viewed as the limit of the GLHDI for $T_i/T_e \gg 1$, while the IAI is the case where $T_i/T_e \ll 1$. The LHCDI or MTSI is the instability which results when current is the primary energy source for the instability, where the TSI is the limit of this instability in the case of a cold plasma with no magnetic field. The LHGDI or LHDI is the instability which results when gradients in plasma properties are the energy source for the instability.

The only instabilities which are not exactly limits of the GLHDI are the cyclotron instabilities. However, they are related. Although they operate at a different characteristic frequency (either the ion or electron cyclotron frequency rather

than the lower hybrid frequency), limits of the GLHDI are linked to the cyclotron instabilities. The dispersion relation of the ECDI intersects the ion-acoustic branch of the GLHDI when equation (II.5) is met, and the DCI actually becomes the LHGDI when equation (II.8) is met. The main difference between all of these instabilities, with the exception of the ECDI, is the conditions of the plasma which cause them; they can all be analyzed in the same manner by using the linearization method to find the dispersion relation as demonstrated in the section II.2, although particle kinetics rather than hydrodynamic theory must be used.

Figure II.2 gives a graphical depiction of the relationships between microinstabilities. The cube represents all lower hybrid instabilities (the GLHDI), the dots represent the electron-cyclotron drift instability, and the cylinder represents the drift-cyclotron instability. All of these oscillations can simultaneously occur in the same parameter space, but not necessarily at the same spatial location. The colored panels of the cube represent limiting cases of the GLHDI for the plasma parameters listed on the three axes. The location of the colored sections should give the reader an idea under what conditions that particular microinstability can occur. It may be noticed that the dots and circles are denser in some portions of the cube than others. This is because theoretically, these instabilities can occur anywhere in the parameter space, but are much more likely to occur where the circles or dots are thickest. Lastly,

when a colored surface shows a brighter color where one of the circles intersects that surface, it indicates a linkage between the two microinstabilities. As the DCI is known to transition to the LHDI for large gradients, the intersection between the circles representing the DCI and the plane representing the LHDI is colored a brighter green than the rest of the LHDI plane. However, the ECDI has no direct linkage to the GLHDI or DCI in this parameter space.

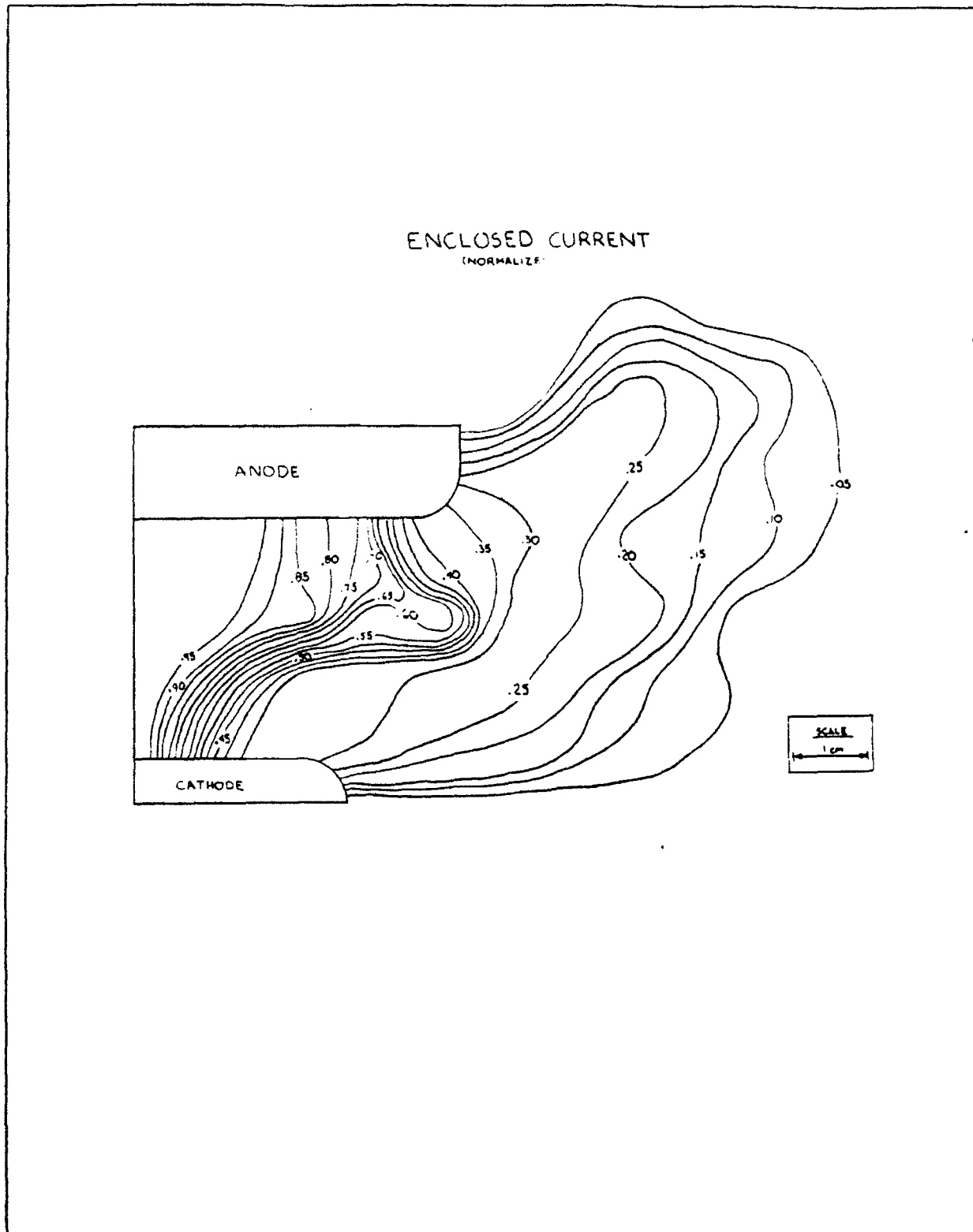


Figure II.1 - Enclosed current contours for operation at 6.8 kA and 2 g/sec mass flow

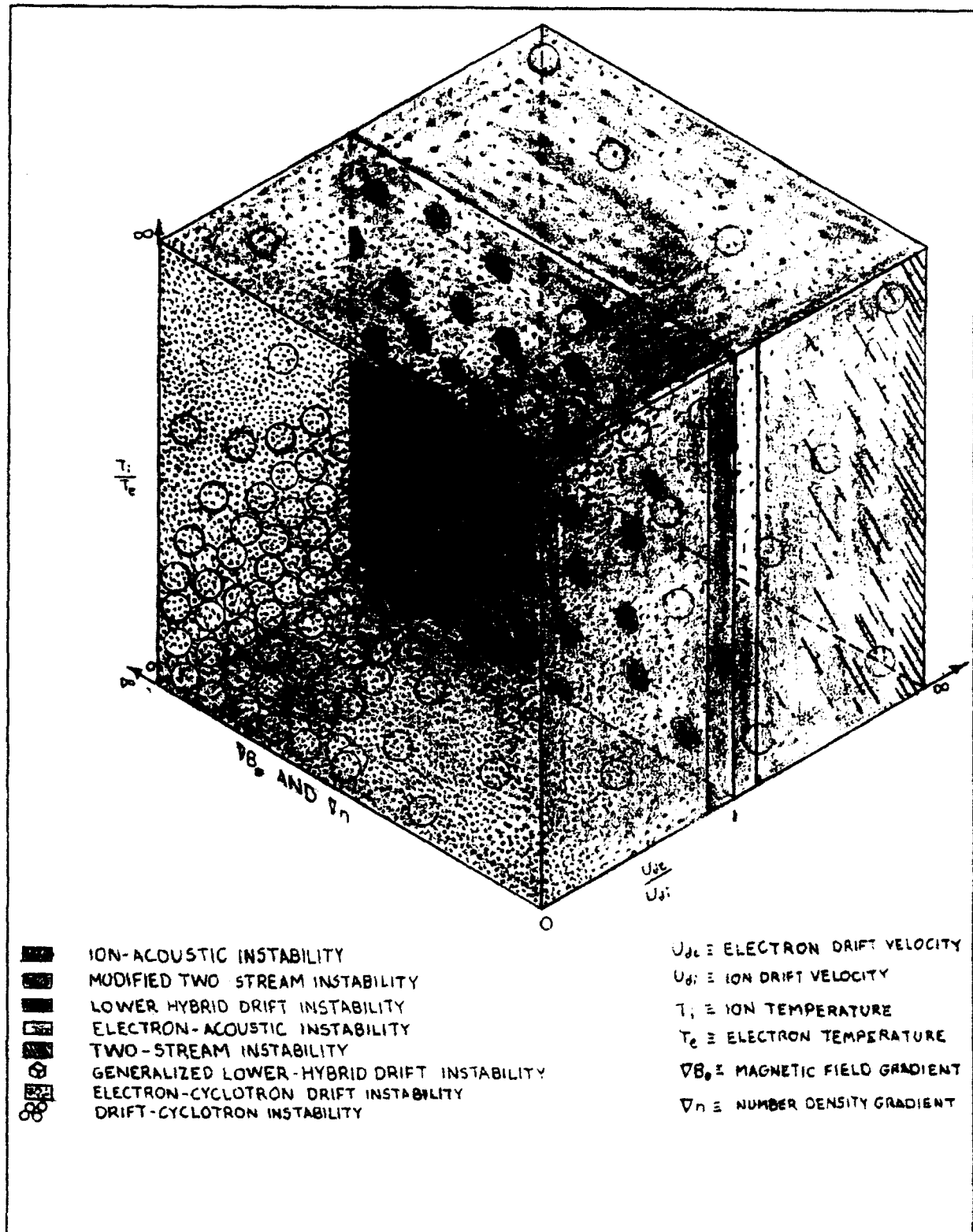


Figure II.2 - Pictorial depiction of microinstabilities existing in parameter space.

III. Experimental Work

Experiments were performed on a MW level, quasi-steady self-field MPD thruster with a 1 millisecond pulse duration at the Electric Propulsion Laboratory at the Philips Laboratory at Edwards Air Force Base in California. A quasi-steady device produces a current pulse which achieves a stable, constant value of current for a long enough duration to approximate steady-state behavior. The global operating characteristics of the thruster, the azimuthal magnetic field, number density and electron temperature were measured. A complete description of equipment used to take measurements as well as information about the thruster, and the chamber in which the thruster was operated is presented in Appendix A.

III.1 Data Acquisition

III.1.1 Characterization of thruster performance

In order to acquire the desired properties, it was first necessary to characterize the performance of the thruster. The thruster is fired by first injecting propellant into the thruster, and subsequently initiating a high-voltage spark in order to ionize the propellant. This ionized propellant provides a conducting path for the high current discharge which produces thrust. The high current discharge was supplied by a 10 section LC (Inductor-Capacitor) pulse forming network (PFN), which is capable of producing a 1 millisecond current pulse of up to 40 kA

and 400 V to the MPD thruster assuming a perfectly matched load [34]. As the gas pulse and spark determine when and how the thruster fires, the first tests conducted were the propellant gas pulse and spark timing measurements. A plot of a typical gas pulse, with the spark trigger shown as a noise spike, is shown in figure III.1.

The gas pulse had an exponential rise and decay portion with a relatively flat steady state portion was reached in approximately 20 milliseconds after triggering the valve and lasted approximately 65 milliseconds. The gas pulse was marred by a small dip in the quasi-steady mass flow shortly after the quasi-steady state had been reached, but this variation was less than 5% of the pulse magnitude and does not appear to have much of an effect on the thruster operation.

The finite rise time of the gas pulse does not cause many complications in a quasi-steady firing. However, a 20 millisecond delay in the initiation of the spark trigger was added to ensure that the engine fired while in the steady state portion of the gas pulse.

Before testing, it was believed that microinstabilities would be more noticeable if the MPD thruster were operated at a point near, but below onset. In order to determine the input parameters (power supply voltage and current) corresponding to a point slightly below onset, measurements of the global thruster voltage and current were conducted. The signals were acquired on the DSA-601 digital oscilloscope, acquiring the voltage and

current simultaneously. Figure III.2 shows sample voltage and current traces at levels before and after onset.

The voltage trace was characterized by a large noise spike at the trigger time, followed by a steady state region of approximately 1.4 msec. It then decayed to a second or even third voltage level depending on the particular firing. In the steady state region, noise was very small for low power settings. When the PFN voltage was in the range 350-550 V, large voltage fluctuations were observed, on the order of 10 per cent of steady state voltage or larger. Malliaris, et. al has indicated that these large voltage fluctuations indicate onset [9]. These fluctuations occurred at a current level of about 8 kA, with widely varying voltages. Figure III.3 shows a plot of global voltage vs. current, referred to hereafter as a V-I curve. In this plot, a near infinite slope was present at a current of 8 kA, leading to the observation that onset can be also defined as the region of discontinuity in a V-I curve. Above 550 V, the voltage fluctuations drop below 10 per cent of the steady state value. Although the oscillations are greater than at low power levels, it appears that the instabilities seen earlier have saturated. However, at these power levels, erosion seems to become significant.

Current responses were relatively free of noise and had an initial overshoot of no more than 10 per cent. The steady state portion was extremely flat, especially at lower power levels, and the current pulse itself had exponential growth and decay. The

current traces were almost identical at all voltages in the onset regime. However, two forms of traces occurred above the onset regime. In the majority of cases, the current increased by a steady, but slight amount over the steady state portion. However, in a few cases, a large peak occurred in the steady state region just before the current decayed. This corresponds to the voltage drop seen in the voltage readings on the same firings. The most likely explanation is that erosion caused additional mass from the copper electrodes, boron-nitride from the injection plate, etc., to enter the thruster, increasing the number of charge carriers, and consequently, current. If the tests with these types of curves are plotted on a V-I curve, there is a clear separation of data from the majority of firings. This set of data has a smaller slope than the other cluster of points, seeming to indicate a regime of higher performance. This makes sense if the above explanation is accepted; the additional mass of eroded materials is expelled, increasing thrust at a given power level. Obviously, though, this type of operation is not desired because parts of the thruster erode.

Tests were also made at 1.0 and 0.5 g/sec up to the onset condition. Based on the V-I curves, an operation point with a current level of about 6.8 kA at a mass flow of 2 g/sec was chosen for the remaining experiments. These conditions corresponded to a point slightly below onset.

III.1.2 Testing Performed

Further testing was designed to produce spatial maps of magnetic field strengths (azimuthal direction), electron number density, electron temperature, and the frequency of number density fluctuations. Measurements were desired both in the near plume and inside the thruster, so a 22 point test pattern involving locations in the thruster plume and inside the thruster was used. This test pattern, which is shown in Figure III.4, was formulated assuming that the plasma discharge would be axially symmetric; only axial and radial positions were varied.

Measurements of the magnetic field were then taken at each of these grid locations by magnetic probes. Only between one and three measurements were able to be taken at each point due to time constraints, with one point being retested after the entire sequence to check hysteresis. Magnetic field measurements were desired because the magnetic field strength is required to calculate the cyclotron frequencies and hybrid frequencies.

After magnetic probe measurements were concluded, measurements with the Langmuir triple probe were conducted. Due to the possibility of probe contamination, only one firing was made at each grid location, except at positions which produced anomalous signal traces; these points were retested. To further reduce contamination, the probes were cleaned by glow discharge after every 5 firings. At each grid location, the probe's mean voltage and current, fluctuations in the probe's voltage and current, and global voltage and current were measured

simultaneously. Electron number density and electron temperature measurements were calculated based on these measurements. These two properties were desired because they characterize the plasma state, while the plasma fluctuations were measured to determine if the plasma oscillations corresponded to a characteristic frequency of suspected microinstabilities. Unfortunately, after the first test sequence was completed, the facility became unavailable for further tests.

III.1.3 Probes

III.1.3.1 Magnetic Probes:

Two different types of magnetic probes were used to measure magnetic fields, although only one type worked successfully. The first type was a Hall probe. The theory governing the operation of this probe is explained in Appendix B. This was the preferred type of probe to be used because of the linear relation between magnetic field strength and probe voltage, and it has been used with a great deal of success in steady state MPD devices. Unfortunately, it did not work well in the quasi-steady MPD device used in this work. One disadvantage of the Hall probe is that the output voltage is on the order of a few microvolts. Extremely large noise spikes at start-up of the quasi-steady thruster drowned out any signal the Hall probe produced. This phenomenon will be discussed further in section III.2.1 and in great detail in Appendix B.

In order to get a discernible signal, an induction type

probe with an analog integrator circuit was used. The induction probe itself produces a voltage which is proportional to the change in magnetic field with time. Thus, to get a voltage which is proportional to the magnetic field strength, the signal must be integrated. This type of probe is a little more complex on account of the presence of an integrator circuit, but much higher signal-to-noise ratios can be achieved. This type of device has been used almost exclusively in pulsed devices up to this time, and it was used successfully in these experiments. The construction and use of the induction probe is discussed in Appendix B.

III.1.3.2 Langmuir Probes:

In order to measure number density and electron temperature, the triple Langmuir probe was used. This probe can measure voltage and current simultaneously, which allows simultaneous measurements of electron temperature and number density based on the application of the probe theory. In these calculations, Laframboise's method with the Peterson-Talbot curve fits [35,36], and Bohm's thin sheath criteria [35,37] were used to calculate electron number density and electron temperature. A more detailed discussion of probe theory and construction is given in Appendix C.

In order to get mean values of plasma properties at the time in the pulse when the frequency data of plasma fluctuations were acquired, two separate oscilloscopes were used. The high

frequency oscilloscope was triggered about halfway through the steady state portion of the current pulse. Because the probe current is directly proportional to electron number density using thin-sheath probe theory [35], the frequency spectra of the current oscillations can be assumed to be identical to the frequency spectra of the number density oscillations. Likewise, the frequency spectra of probe voltage oscillations can be assumed to be identical to the frequency spectra of electron temperature oscillations because voltage is directly proportional to the electron temperature in the thin sheath limit [35]. However, the absolute magnitudes of the oscillations for both plasma properties are merely proportional to the measured voltage and current, and depend on the mean properties of the plasma. Fast fourier transforms were used to convert voltage and current oscillations into frequency spectra. Although the frequency oscillations without wave vector and amplitude distribution is not sufficient to identify the types of instabilities [15], they do give an indication of a range of instabilities which may be occurring.

Probe contamination became a problem by causing apparently erroneous mean values to be calculated inside the thruster. Cleaning the Langmuir probes by means of a glow discharge helped to some extent, but for measurements inside the thruster, Langmuir probes will have to be replaced after a few firings in the future.

III.1.3 Calibration:

Calibration of the magnetic probes was accomplished by placing the magnetic probe at a radius just inside the anode and very close to the back plate of the thruster, and measuring global current while firing the thruster. It was assumed that all of the measured current would pass through a circle enclosed by the radius the probe was placed at. As a result, the actual magnetic field was determined based on

$$B_{\theta} = \frac{\mu_c I}{2\pi R} \quad (\text{III.1})$$

where $B_{\theta} \equiv$ azimuthal magnetic field, and $R \equiv$ radius the magnetic field is measured at. The voltage of the probe was then acquired after passing through the integrator. The thruster current was varied and readings taken at each of these points to produce a calibration curve. A more detailed discussion of calibration is given in Appendix B

No calibration of the triple Langmuir probe was required, although the frequency response of the probe was checked. However, this was actually a check of the electronics of the probe circuit more than a check of the probes themselves, as the operational amplifiers used to amplify the signal were the limiting factor, not the probe itself.

III.2 Measurements

III.2.1. Magnetic Field

Initial attempts to make magnetic field measurements

employed a Hall probe. However, due to very low signal-to-noise ratios (SNR) which made results indiscernible, an induction type probe with an integrator circuit was used instead to measure the magnetic field. After some initial calibration problems, usable signals from this type of probe were acquired because the signal levels on this type of probe were a few orders of magnitude above the signals produced by the hall probe. However, the initial start-up spike still caused some problems. A sample magnetic field trace is shown in Figure III.5.

This noise appears in the start up and dissipates fairly rapidly with time. By the time the current pulse begins its downward swing, this noise has largely disappeared. Therefore, when determining the voltage level of the probe, the voltage level after the thruster had finished firing was defined as the reference level, rather than the voltage level before the thruster fired. This technique of measurement seemed to yield consistent results, within the range of noise still present. A fairly steady variation of magnetic field strength with axial and radial positions resulted. In contrast, when the voltage before firing was defined as the reference level, the magnetic field strengths fluctuated wildly with position. This was not consistent with results observed by other experimenters [12,38-41].

Only one magnetic field measurement was made at most locations due to time constraints. The voltage trace of the probe was expected to look similar to the global current trace

because of the relationship between magnetic field and current, defined in equation (III.1). If the voltage trace behaved as expected, the probe was moved to the next location. However, if unexpected voltage traces occurred, a few additional measurements were made to determine if the unexpected trace was repeatable. At these locations, the magnetic fields determined from the voltage traces are averaged. A spatial map of the average magnetic field at each grid location is shown in figure III.6. Based on the magnetic field measurements shown in figure III.6, an enclosed current contour map was generated, shown in figure II.1. This map was used in chapter II to determine the location of certain microinstabilities because the contour lines may be interpreted as actual current paths inside the thruster. However, the primary purpose of the magnetic field measurements was to provide data for the calculation of some characteristic frequencies of the plasma. These frequencies are tabulated in Table III.1.

It should be noted that positions (17) and (23) in the test pattern (shown in figure III.4) are actually the same location. As both values of B_0 are fairly close, it appears that hysteresis is negligible within the consistency of thruster firings. The major trend noticeable here and in the contour maps is that B_0 increases significantly as the position moves towards the rear of the thruster, with the sharpest gradients occurring inside the thruster. However, the region of strongest magnetic field for a given axial position was about halfway between the electrodes.

As the characteristic frequencies are directly proportional to B_0 , they follow the same general trends. The characteristic frequencies listed in Table III.1 will be important in the next section.

III.2.2.2 Langmuir Probe Measurements

III.2.2.2.1 Number Density Fluctuations:

The triple Langmuir probe was used to measure number density fluctuations, while simultaneously measuring the mean electron temperature and electron number density. However, to accomplish this, an additional oscilloscope was required to record signals on two different time scales. Global current and voltage were also monitored at the same time, using the same time scale used for measurement of mean plasma properties. Sample probe traces for the high frequency oscillations are shown in figure III.7, and sample traces of the absolute values of probe current and voltage used for calculation of mean plasma properties are shown in figure III.8. Both voltage and current traces from the probe were expected to look similar; namely, to have a fast initial transient, a steady state region, and a slower final transient because the temperature and number densities will increase as the thruster fires, and return to zero when the firing is over. The probe traces behaved according to expectations in the plume region and were only slightly different inside the thruster along the cathode. However, the last six locations (near the anode and inter-electrode area) examined appeared to produce questionable

data. The values for voltage and current of the probes no longer seemed to have a steady variation with position. Instead the values were a great deal higher, which produced unreasonable electron temperature and electron number density values when the probe theory was applied to the measured mean values. In addition, the strength of fluctuations seemed to increase significantly.

Looking at the fast-fourier transforms (FFT) of the current traces at all locations, there is a large, broad band peak centered between 100 kHz and 1.5 MHz depending on the grid location. It can also be noted that the magnitude of this peak increases significantly at the locations where onset occurred. However, this peak is of relatively low frequency, and is on the order of the frequency expected of the global hydrodynamic instabilities associated with onset [10,15], which have been postulated to be either macroscopic electron acoustic instabilities [10], Pierce instabilities [13,14], or electro-thermal instabilities[10].

However, the experiments performed in this paper were based upon expectations of oscillations at the lower hybrid frequency of the plasma, determined by the magnetic field strength at the same location. The values of the lower hybrid frequency at each location are compiled in table III.1, where the numbered locations are shown in figure III.4. However, a clear peak in the frequency spectra at the lower-hybrid frequency at any location in the thruster was not observed. There might have been

an indication of lower hybrid oscillations at one point near the cathode at the exit plane, but the observed peak was so close to the noise level as to be inconclusive.

III.2.2.2.2 Mean Plasma Properties

Mean plasma properties were obtained by acquiring the absolute values of the current and voltage of the probe at the time the plasma fluctuations were measured. A larger time scale was used to allow average values of voltage and current to be obtained in the neighborhood of the time at which plasma fluctuations were recorded. A more detailed discussion on how plasma properties were acquired from voltage and current traces is explained in Appendix C. Table III.2 shows various plasma properties at each measured location, where the numbered locations are shown in figure III.4

It can be noted that the last six locations have abnormally high electron temperatures, with position (19) having an extremely high value. The reasons for these abnormal results will be discussed in section III.3. As stated earlier, points (17) and (23) comprise a check for hysteresis, giving an indication of the error in the last six points. Not only was there a significant difference between the values at points (17) and (23), but all of the points in between were so far beyond the range of expected results that Laframboise's theory could not be used to calculate T_e and n_e . Instead, Bohm's thin sheath theory was used.

Examining spatial variations of the properties for the good locations, the trends generally follow what would be expected. A contour map of electron temperature is shown in Figure III.9. Examining the map, there appears to be a low temperature pocket starting at the exit plane near the anode, and extending radially outward. In general, electron temperature increases at locations toward the rear of the thruster, and increase as position approaches the anode. The sharp gradients in T_e apparent in Figure III.9 are due to the abnormally high results acquired in the anode region inside the thruster.

A contour map of electron number density is shown in Figure III.10. Examining the map, the number densities are highest near the cathode, with fairly steep gradients in this region as well. In general, there is a strong decrease in number density with radial position, and a weaker increase in number density as the position approaches the rear of the thruster.

The other two properties in the Table III.2 are shown primarily for illustrative purposes. The electron debye length, λ_{de} , was calculated according to

$$\lambda_{de} \equiv \left(\frac{\epsilon_0 K T_e}{n e^2} \right)^{1/2} \quad (\text{III.2})$$

where ϵ_0 is the permittivity of free space, n is total number density, and K is the Boltzmann constant. This is an important parameter in probe theory, and typically the electron debye length is assumed to be about the same as the total debye length. The electron collision frequency is the sum of the electron-ion

and electron-electron collision frequencies using the formula [6]:

$$\nu_{ee} = 7 \times 10^{-6} \frac{n \ln \Lambda}{T_{ev}^{3/2}} \quad (\text{III.3})$$

where $\ln \Lambda$ is the natural log of the maximum impact parameter. In using this formula, it is assumed that n is approximately equal to n_0 and only singly charged ions are present. In addition, collision frequency is necessary to find the electron Hall parameter. Anomalous conductivity has been seen to scale strongly with the electron Hall parameter [4].

III.3 Interpretation of Results

III.3.1 Magnetic Field

The magnetic field results seemed, in general, quite reasonable and without spurious values. Steep gradients occurred inside the thruster, but the magnetic field strengths increased monotonically as the probe moved further back into the thruster. In addition, errors which would be caused in measurements due to effects such as probe ablation, plasma cooling, and displacement of the current path due to the presence of the probe were examined for plasma conditions which were expected in the near plume, and were found to be negligible. However, there are some factors which introduce errors into these measurements.

Because the actual signal is integrated, the error resulting from the noise should be reduced because a positive and negative spike will come close to cancelling each other out. However, as

the operational amplifier only had a frequency response of about 10 MHz, very high frequency, large amplitude noise spikes may have been only partially eliminated. In other words, a positive noise spike may have been "seen" by the integrator, but its opposing negative spike which occurred only a few nanoseconds later may have been missed or severely attenuated. Thus, to the integrator, it appears as if there is a net positive signal, rather than just noise.

At some locations, namely inside the thruster near the anode, there was no actual flat portion of the trace. Coupled with rather extreme effects of electrical noise in these regions, there is a fairly significant amount of error in these regions. At these points, three firings were made and the measurements were averaged in an attempt to get a mean value of magnetic field strength. The results shown in figure III.6 and table III.1 indicate that the magnetic field at the anode locations inside the thruster still seem to vary smoothly with position, but the absolute values of the strength may be somewhat questionable.

Looking at these undesired effects, one may question the calibration technique, as the probe was placed very close to the anode. However, the voltage traces with the probe near the back plate were flat in the steady state portion of the current pulse, in contrast to the greatly sloped trace in the steady state portion of the current pulse that was seen during firings near the anode about halfway into the thruster. When the probe is in these locations, it appears to cause a significant disturbance in

the plasma. Due to a lack of digitizers in the oscilloscope, a global voltage trace of the thruster while making magnetic field measurements was not acquired. As will be discussed in the next section, when the triple Langmuir probe was placed in these same locations the global voltage showed that onset was occurring, although no indication of onset was apparent when the probe was in other locations.

III.3.2 Langmuir Probe

Most langmuir probe measurements made in the plume and near the cathode seemed fairly reasonable. It should be noted, however, that there is an over prediction of measured electron temperatures at outer radii where the probe was not aligned with the probe. This effect will be discussed later in this section and in Appendix C. However, all of the firings with the probe in the anode region inside the thruster were highly questionable. Two of the major reasons for this are probe contamination and perturbation of the plasma by the probe.

To prevent probe contamination, after every five firings, a glow discharge was performed in order to clean the probes by ion bombardment. When the probe was in the plume, this technique was very successful in keeping the contaminants off the probe, as evidenced by the lack of spurious results. The "good" behavior of the signals probably resulted because, in the plume, the probe is farther away from the sources of contaminants, and the flux of contaminant particles is correspondingly reduced. However, as

the probe was moved inside the thruster, it moved closer to the sources of contamination, namely the electrodes and the back plate.

Although the probe voltage and current traces are reasonable, the absolute magnitudes of the probe current trace may be over predicted slightly at locations near the back of the thruster. The overprediction results because tungsten from the cathode ablates, and may attach to the triple probe. This tungsten coating increases the effective collection area of the probe, which will of course, increase the current to the probe. The coating is cumulative for a constant flux of contaminants.

Near the cathode, this effect may have been alleviated somewhat by the contamination of an insulating species, boron nitride. This is the material of which the back plate is made, and the flux of contaminant particles will increase as the back plate is approached. Thus the increase of collecting area resulting from the deposition of tungsten on the probe electrodes may have been reduced by the deposition of insulation material on the probe as well. What all this means, is that by the time the probe approached the anode in the test sequence, there was a great deal of uncertainty in the actual collection area of the probe. As the probe collection area is a parameter used in the calculation of electron number density and electron temperature from the voltage and current readings, a great deal of uncertainty was introduced into the calculated values of those plasma properties. Although glow discharges were still

performed, inside the thruster the mass flux of contaminants was high enough to cause concentrations of contaminants on the probe which were unable to be completely removed by ion bombardment.

Another factor which resulted in strange results inside the thruster was the perturbation of the plasma and current paths by the triple Langmuir probe. As mentioned earlier, when the magnetic probe was placed in certain locations, the signal traces did not behave as expected. The same phenomenon was observed with the triple Langmuir probe, especially in the region near the anode at the axial location corresponding approximately to the cathode tip. This point shall be referred to as the "mid-anode" position. Due to the lack of oscilloscope digitizers in the magnetic probe measurements, monitoring of the global voltage at the same time as magnetic probe voltage was not possible. However, with the addition of a second oscilloscope for the triple Langmuir probe measurements, global values were monitored.

When the triple Langmuir probe was placed in the mid-anode location, the global voltage trace indicated that onset occurred. Two other locations showed indications of onset, but they were not as "full-blown" as at the mid-anode position. In addition the other two points of significant global voltage oscillations were not contiguous. Looking at the enclosed current contours shown in Figure II.1 earlier, these locations have many current paths pass through them. When the exposed wires of the Langmuir probe were positioned in these locations, onset was induced. However, when the insulated portion of the probe was in the same

location no significant effect on the global voltage was observed. In addition, when the bare wires were at locations nearer the cathode which had a comparable number of current paths, onset was not observed.

At the locations where onset was induced, the voltage traces were as much as an order of magnitude higher than at other locations. Probe contamination can account for small increases in current and/or voltage values, but not of this scale. Obviously, the absolute magnitude of any number density or electron temperature calculations in these regions is extremely suspect. Further investigation of the perturbation effects of conducting materials placed in the discharge current paths is necessary to determine the reason for the erroneous probe measurements.

However, probe contamination will not affect the frequency of the fluctuations to the probe, merely the amplitude. Thus, the frequency data even in these highly questionable regions can probably be accepted, albeit with some skepticism. In fact, examining the frequency data at these highly questionable points, the characteristic frequencies are indicative of those which are expected to occur at onset.

These results were unexpected. Previous work by other experimenters had suggested that lower hybrid frequency oscillations would be present at some locations [1,30]. However, calculation of U_{de}/V_{ti} based on mean electron temperature, mean number density, and magnetic field gradients, the values range

from .92 to 4.75. According to Choueiri, microinstabilities are supposed to occur when $U_{i0}/v_{ti} > 1.5$ [28]. As stated earlier, some locations will yield questionable results due to contamination and perturbation of the plasma, and there may be errors of as much as a factor of 2 in both T_e and n_e due to the non-alignment of the probe with the ion flow vector [35]. Consequently, although the above ratios appear to indicate that microinstabilities will occur at some locations, all of these ratios could fall below 1.5 when experimental error is taken into account.

Table III.1 - Characteristic Frequencies				
Point	B_0 (Gauss)	$\omega_{\text{L}}(\text{MHz})$	$\omega_{\text{L}}(\text{kHz})$	$\omega_{\text{H}}(\text{MHz})$
1	30.0	92.3	1.26	0.341
2	16.9	47.1	0.643	0.174
3	44.5	124	1.70	0.460
4	31.6	88.3	1.21	0.326
5	40.0	106	1.45	0.392
6	101	282	3.85	1.04
7	119	332	4.54	1.23
8	70.1	195	2.68	0.723
9	77.4	216	2.96	0.800
10	65.7	184	2.51	0.678
11	224	624	8.53	2.31
12	148	414	5.65	1.53
13	119	333	4.55	1.23
14	238	666	9.09	2.46
15	278	778	10.6	2.87
16	287	802	10.9	2.96
17	464	1300	17.7	4.80
18	384	1070	14.7	3.97
19	321	897	12.3	3.32
20	181	507	6.92	1.87
21	324	906	12.4	3.35
22	314	879	12.0	3.25
23	498	1390	19.0	5.15

Table III.2 Mean Plasma Properties

Point	T_e (eV)	n_e ($m^{-3} \times 10^{20}$)	λ_{pe} (μm)	v_e ($s^{-1} \times 10^4$)
1	2.99	6.76	0.494	7.36
2	2.72	3.75	0.633	4.80
3	3.34	1.79	1.02	1.82
4	3.29	0.672	1.64	0.736
5	3.14	0.258	2.60	0.316
6	3.39	6.71	0.528	6.2
7	3.11	4.56	0.614	4.83
8	2.79	2.68	0.759	3.38
9	2.33	1.45	0.943	2.4
10	2.11	0.802	1.21	1.56
11	4.16	6.84	0.58	4.81
12	3.03	4.76	0.594	5.18
13	5.22	1.83	1.26	1.02
14	4.81	7.07	0.613	4.09
15	5.41	14.0	0.463	6.67
16	5.29	18.6	0.397	8.96
17*	7.25*	1.74*	1.52*	0.626*
18*	8.37*	1.4*	1.82*	0.419*
19**	59.9**	3.77*	2.96*	0.073*
20*	8.83*	2.18*	1.5*	0.594*
21*	9.76*	4.84*	1.06*	1.11*
22*	12.2*	4.14*	1.27*	0.71*
23*	9.79*	3.82*	1.19*	0.882*

* questionable data point

** erroneous data point

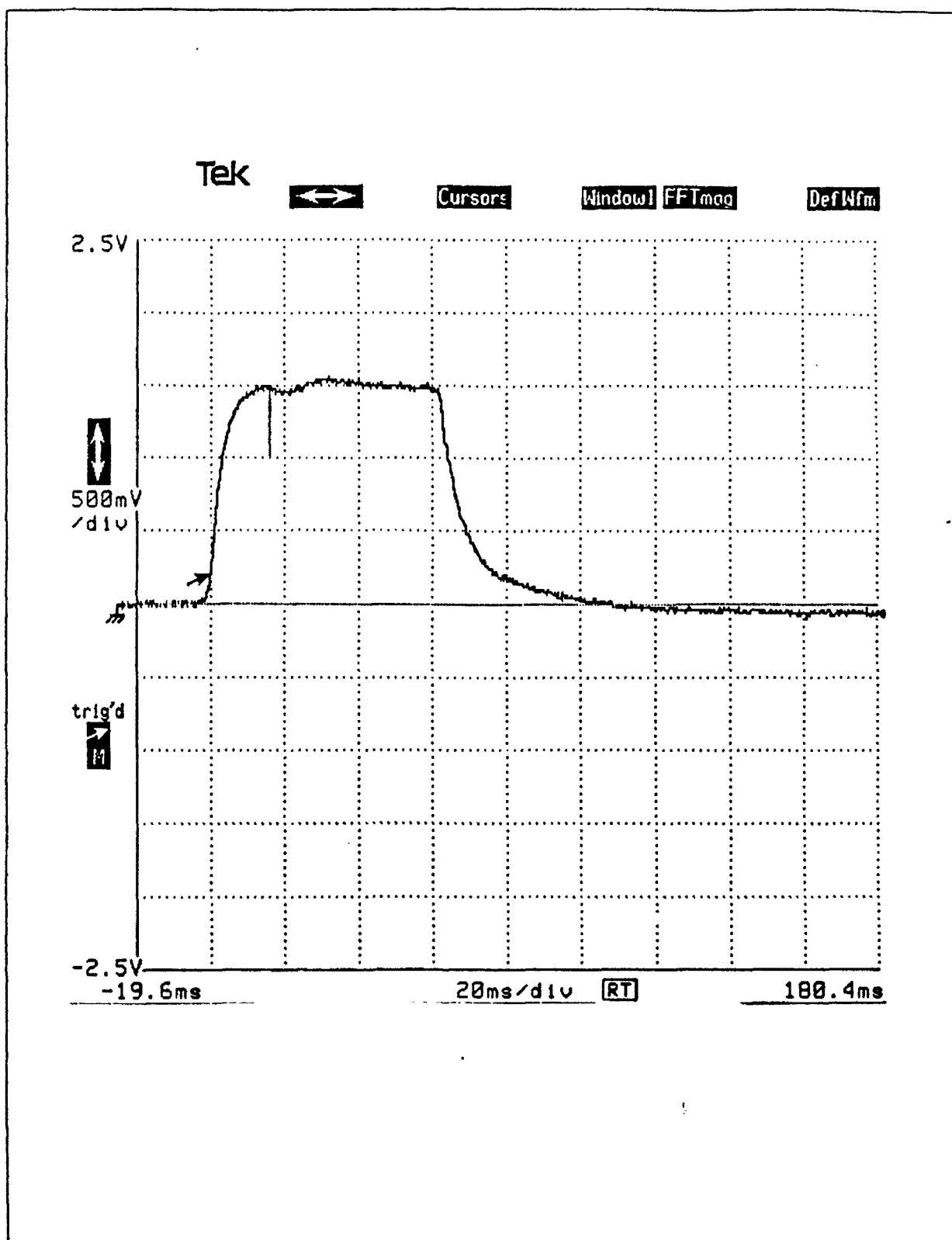


Figure III.1 - Gas Pulse with Spark trigger

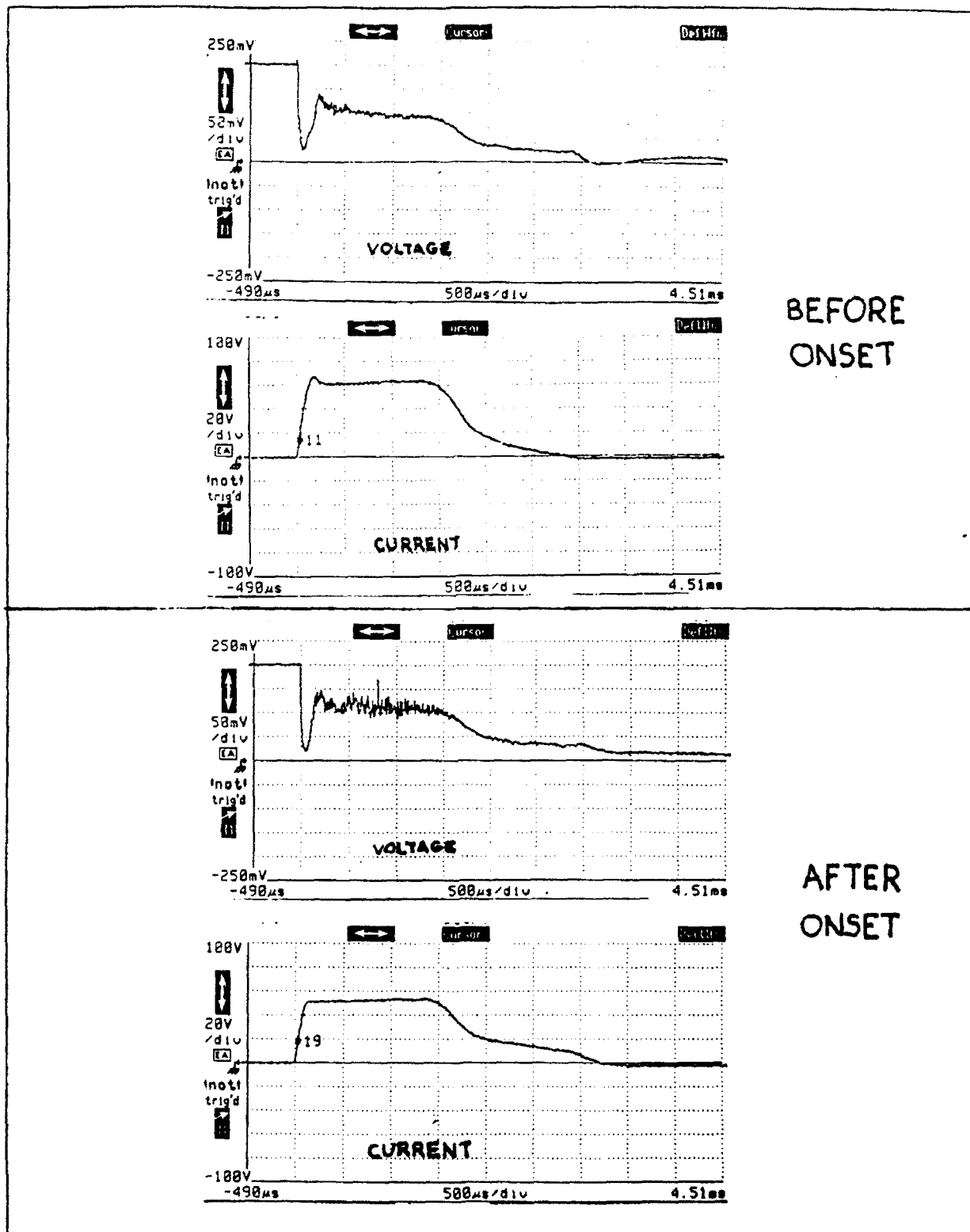


Figure III.2 - Sample current and voltage traces before and after onset

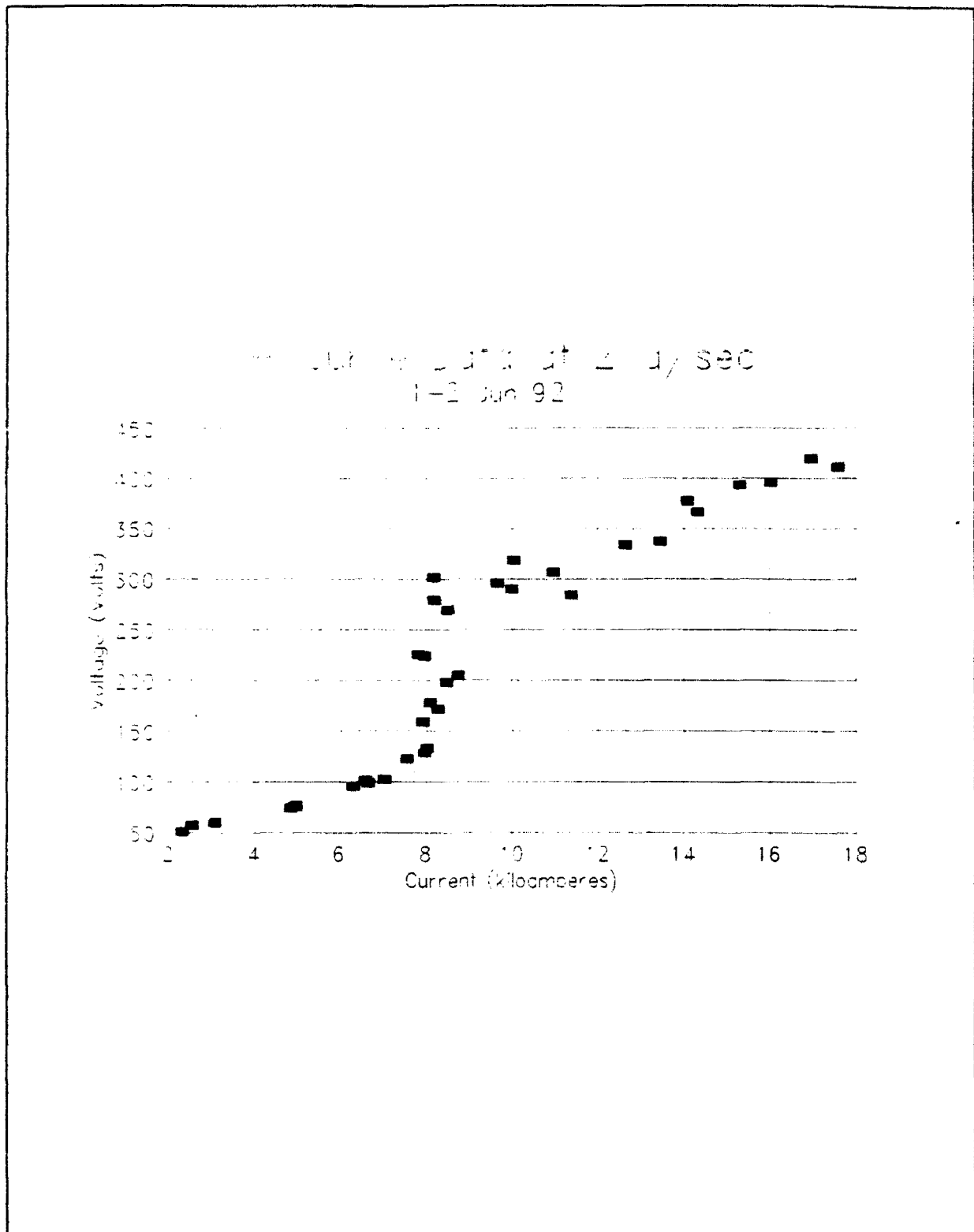


Figure III.3 - V-I curve (good data)

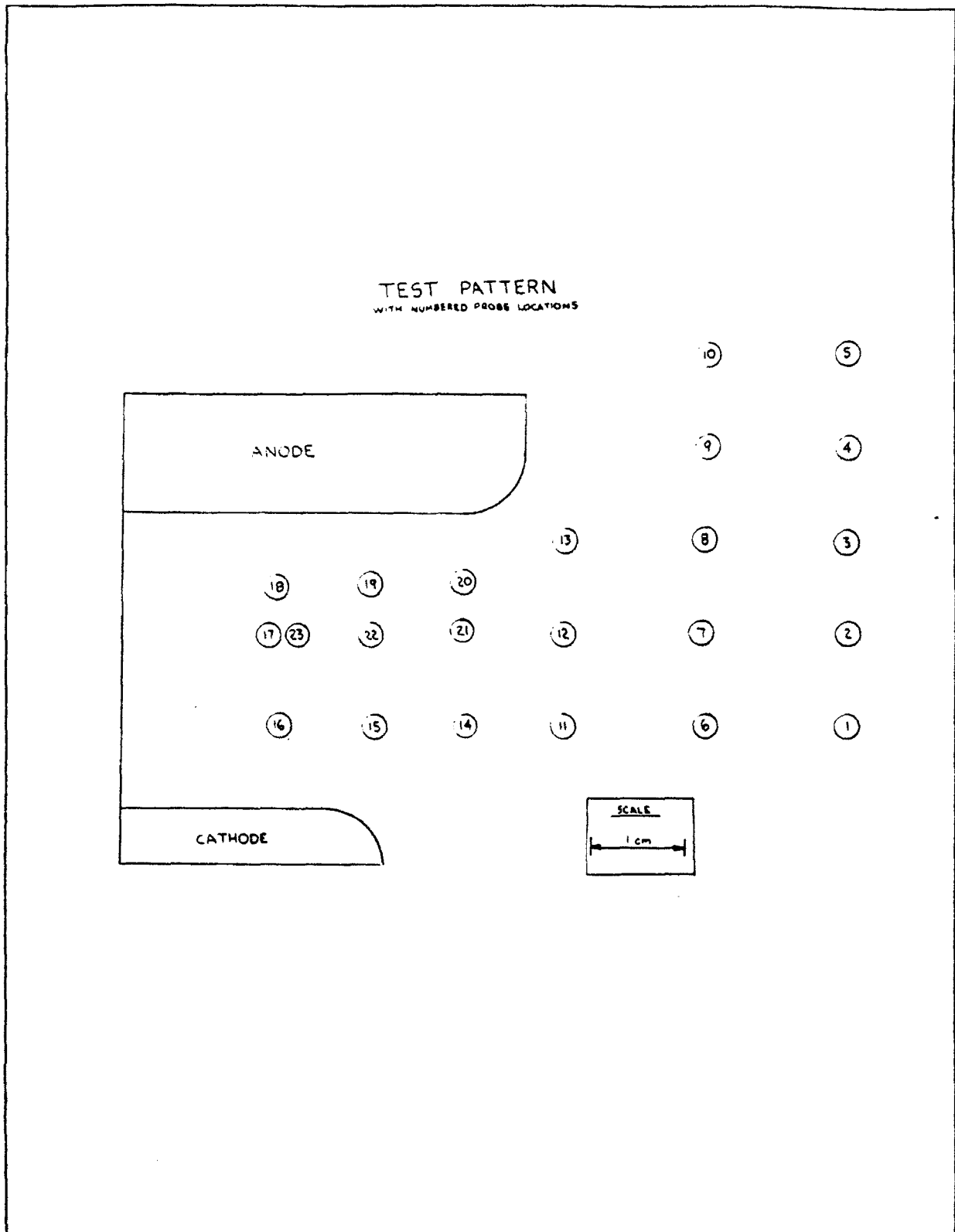


Figure III.4 - Thruster Test Pattern

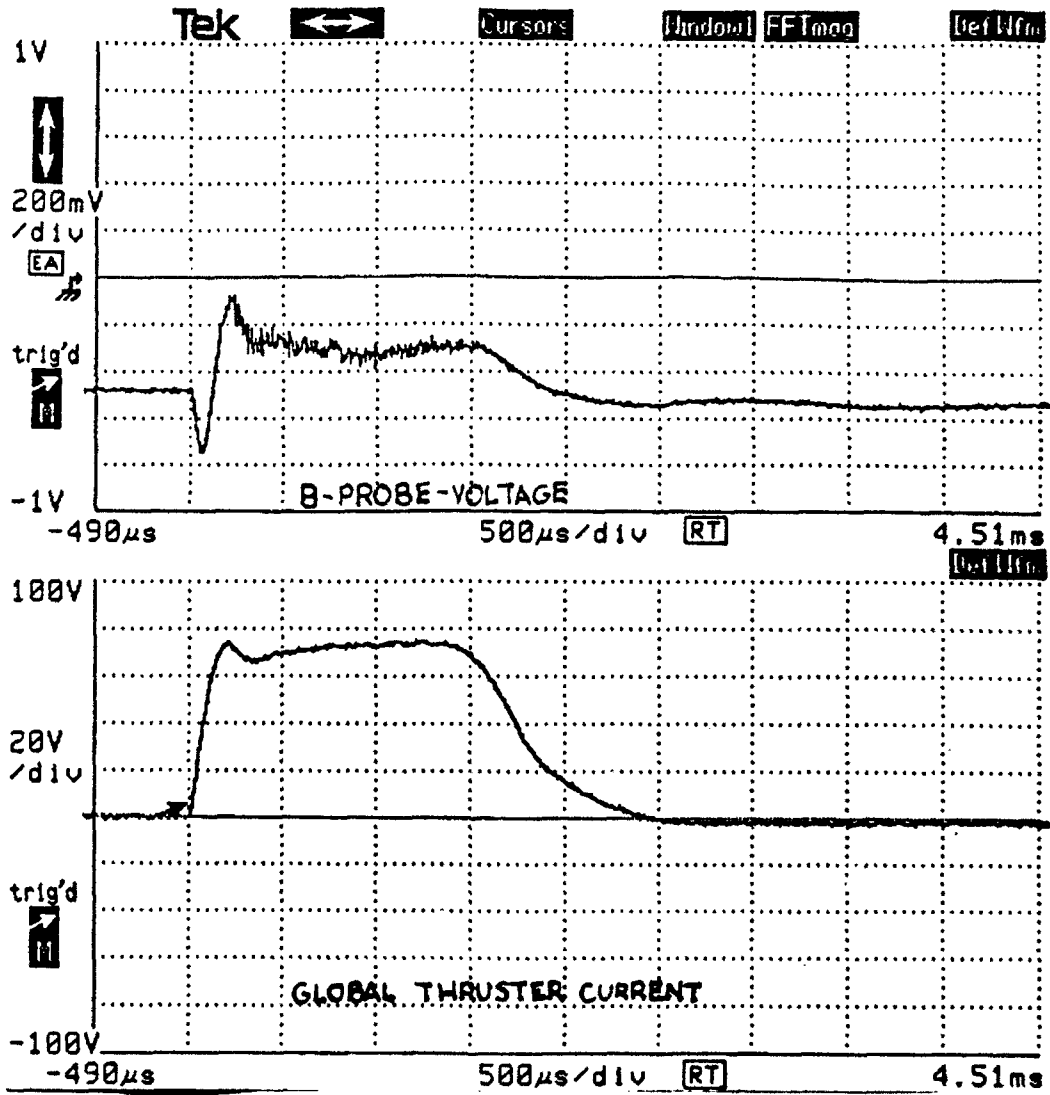


Figure III.5 - Sample magnetic probe voltage trace

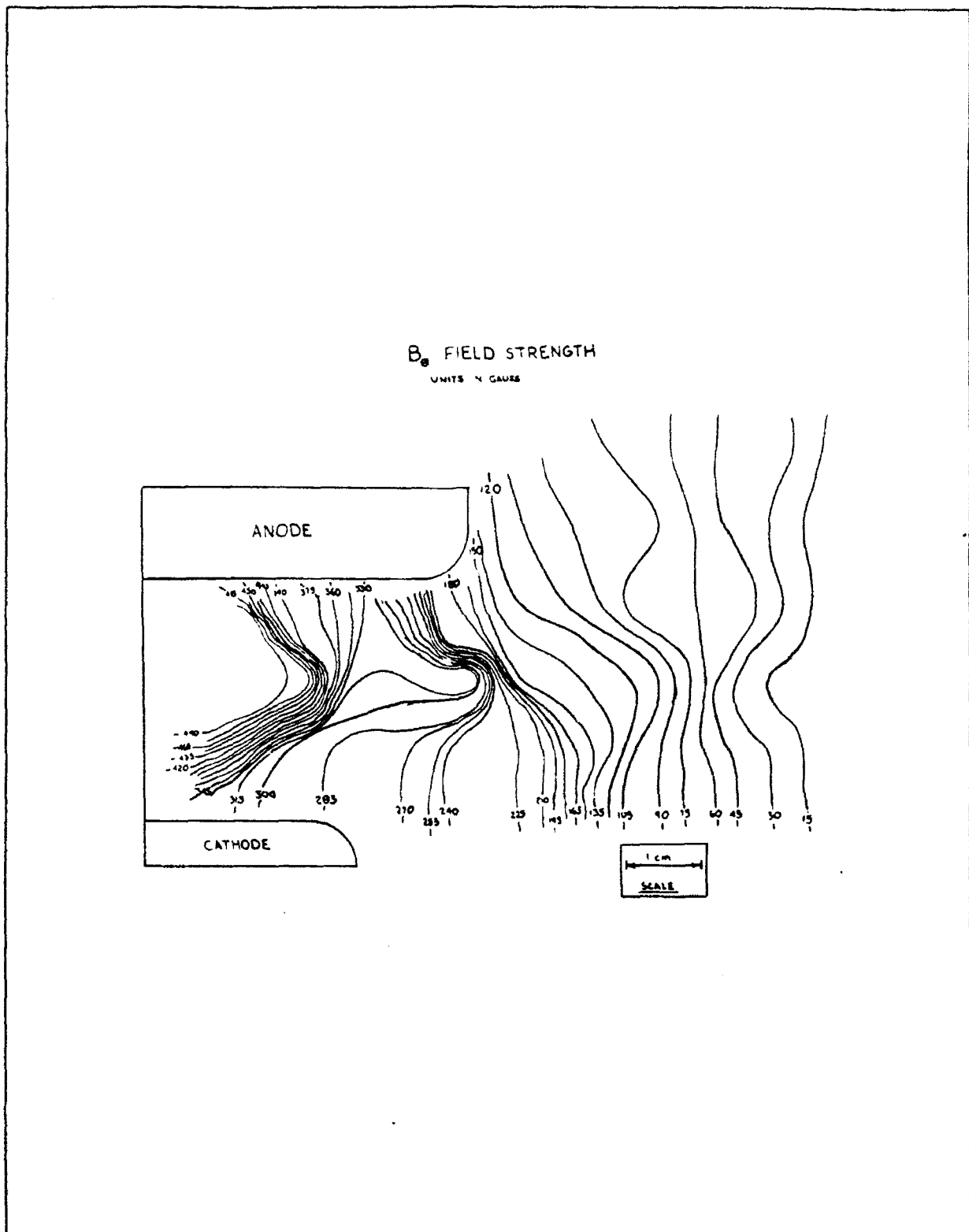


Figure III.6 - Spatial Map of average magnetic field with contours for 6.8 kA of current.

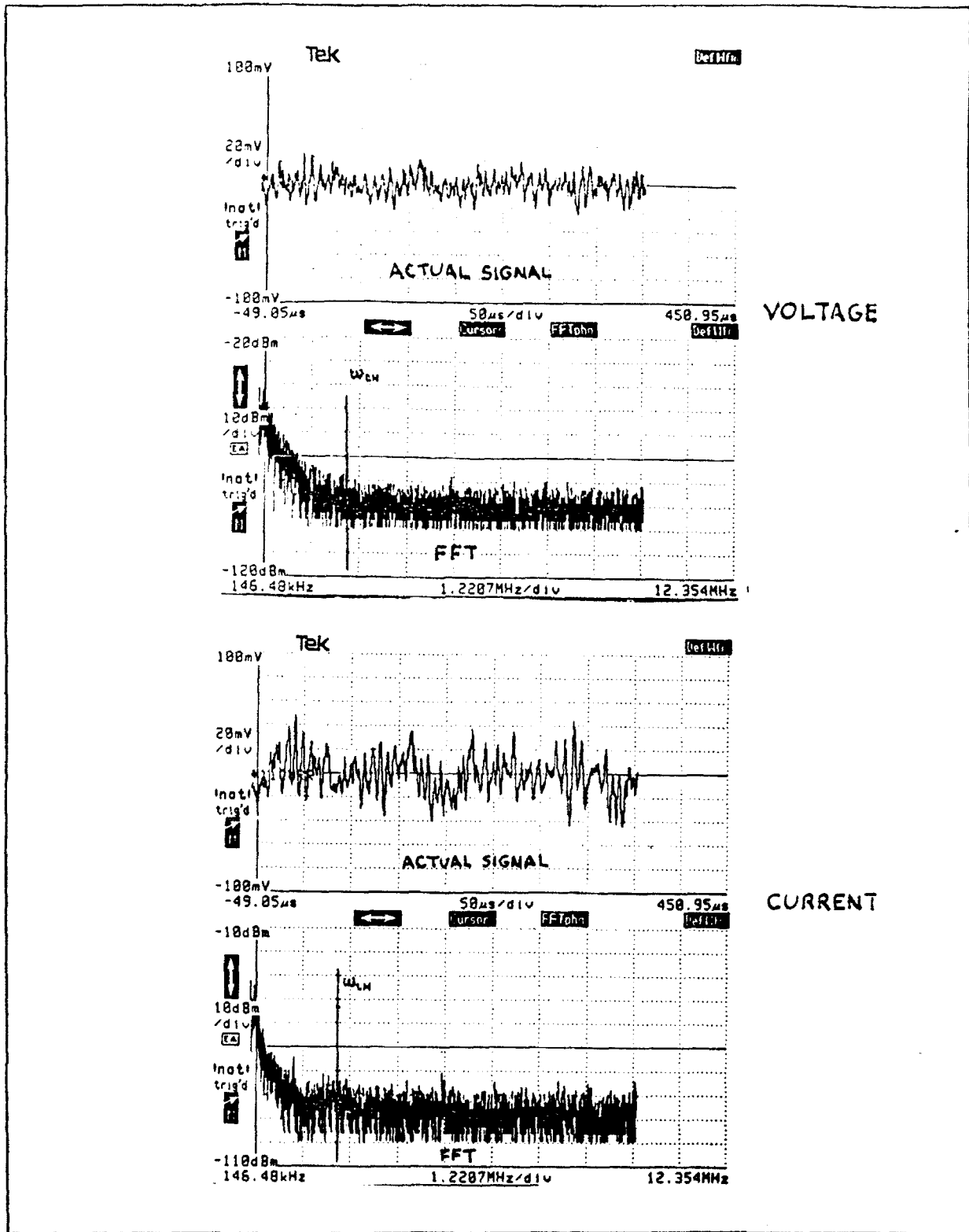


Figure III.7 - Sample high frequency oscillation signal from the triple Langmuir probe

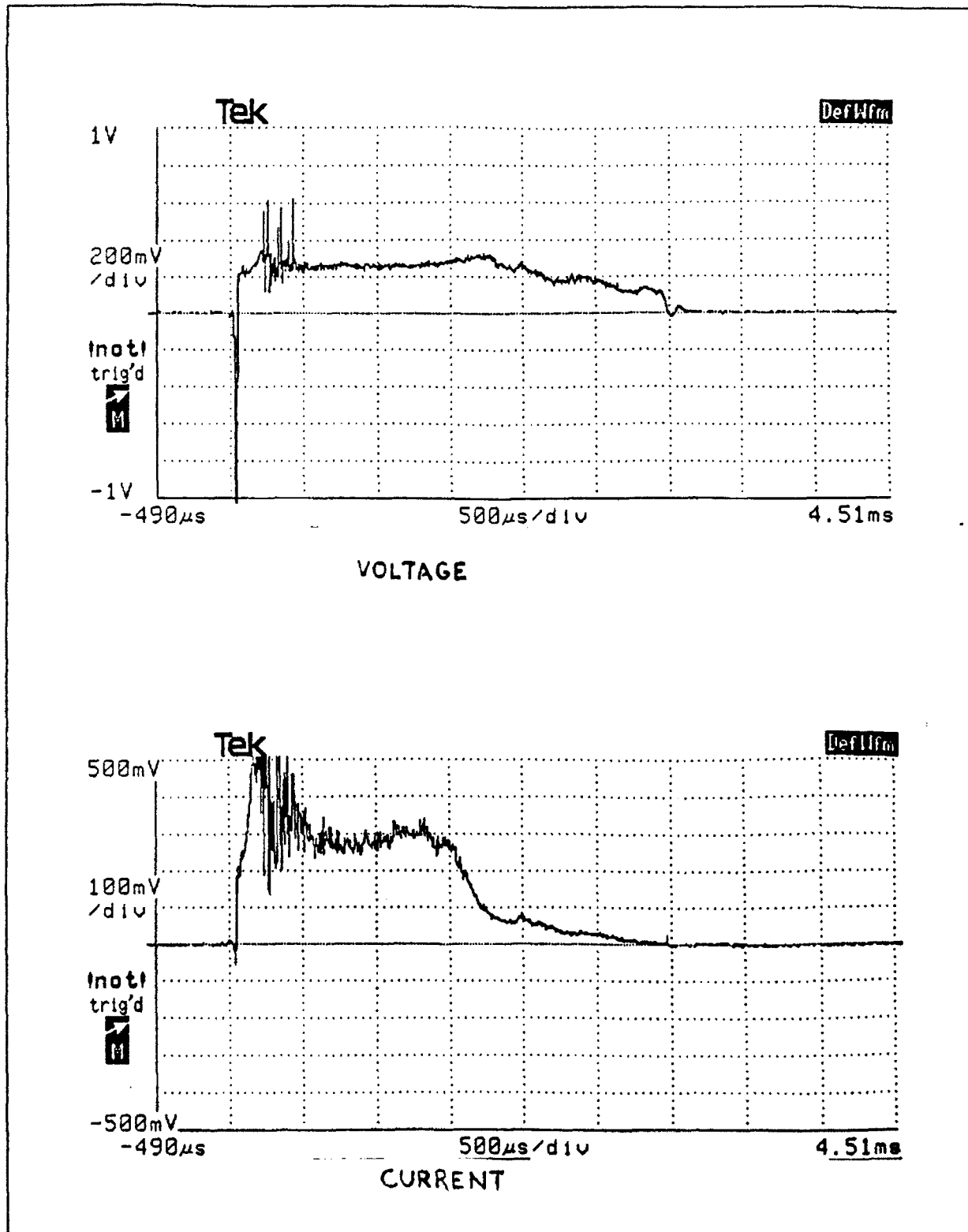


Figure III.8 - Sample probe voltage and current traces (absolute values)

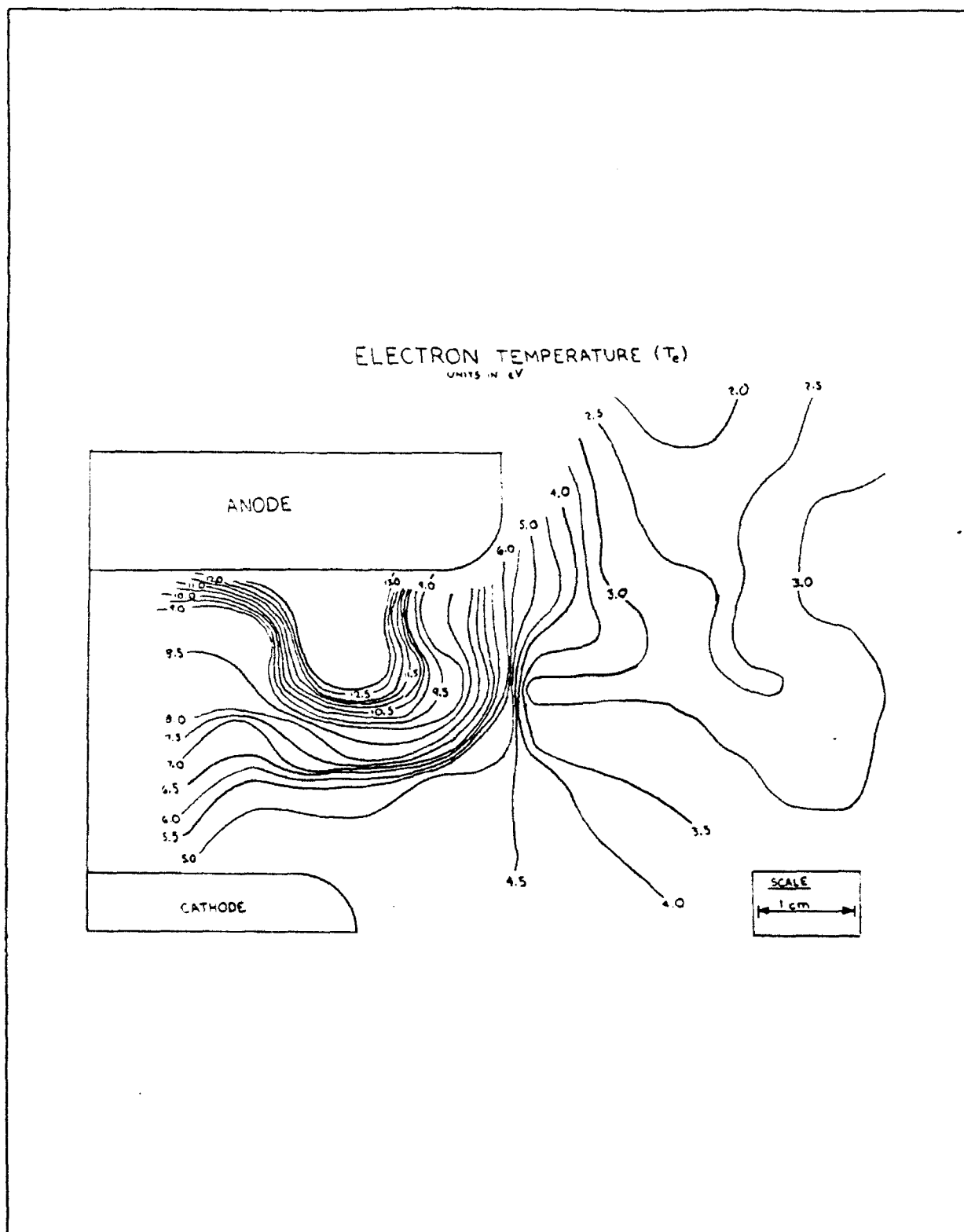


Figure III.9 - Contour map of electron temperature for current of 6.8 kA.

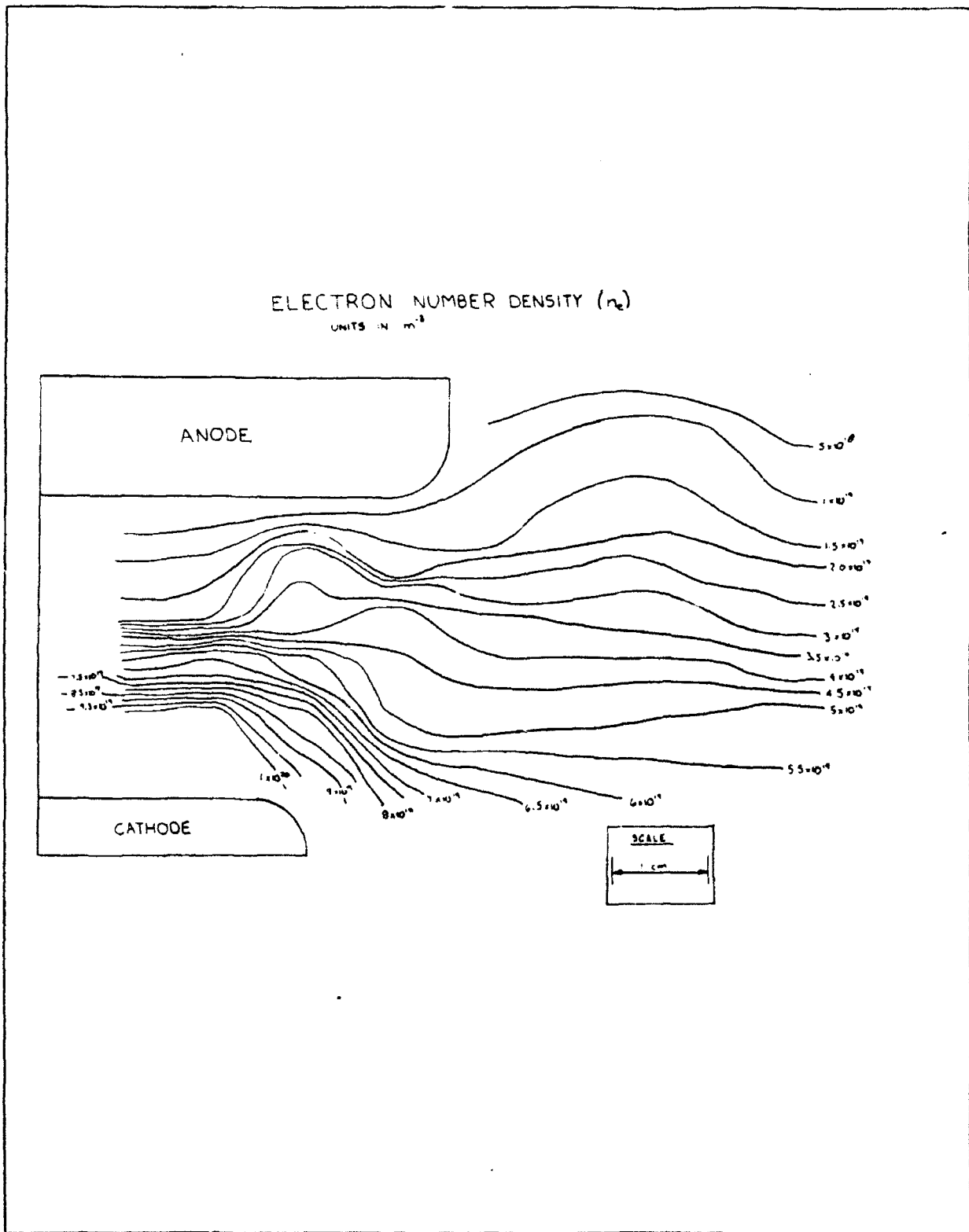


Figure III.10 - Contour map of electron number density at a current of 6.8 kA

IV. Calculation of Plasma Transport Properties

IV.1 Bose Method

To illustrate the effects of microinstabilities on the transport properties inside the thruster, a computer code which calculates transport properties classically according to kinetic theory was modified to account for microinstabilities. The computer code used was developed by Tarit Kumar Bose[42,43], and it assumes a two-temperature, multiple species, multiply ionized plasma. As a two temperature plasma is a thermal non-equilibrium case (which is one reason these instabilities can occur) it is assumed that the particle temperatures are perturbed from equilibrium. This assumption is made because transport properties are derived from a first order perturbation of the equilibrium state.

Thus, a quasi-equilibrium state must be determined, assuming the state can be described in terms of the total pressure, p , the heavy particle translational temperature, T_h , and the translational temperature of the electrons, T_e . Also, it is assumed that the species excitation temperature is equal to T_e . Mole fractions of the various ionized species are determined through the use of generalized Saha equations according to the Monti-Napolitano and Veis model[44,45], which is based on the principle that the total species partial pressure does not change due to chemical reactions. However, it must be noted that the use of the generalized Saha equation assumes a quasi-equilibrium state. In terms of an MPD plasma, this assumes that the time it

takes for a particle to ionize is much less than the ion residence time in the thruster. Unfortunately, it is not known if this condition is met in the MPD thruster due to the high ion drift velocities, on the order of 1-5 km/sec [46]. For the purpose of this analysis, it will be assumed that the particles have time to ionize before they leave the thruster. It can be demonstrated that the transport properties for collisions in which one of the colliding partners is an electron and collisions between only heavy particles can be evaluated separately[42]. Viscosity, translational heat conductivity, and electrical conductivity are those properties which can put this fact to use. Other transport properties must use an ultra-simplified method [47]; however, since the only transport property examined in this report is electrical conductivity, this ultra-simplified theory will not be discussed further. The reason for this emphasis on electrical conductivity is that the current which supplies the thrust for an MPD device is dissipated directly by electrical resistivity.

To calculate the electrical conductivity, a fourth order Sonine polynomial expansion was used. Chapman and Cowling have shown that transport properties can be expressed exactly as ratios of infinite determinants [47]. However, these ratios converge fairly rapidly as more rows or columns are added to the determinant. Thus, one can get a good approximation of the actual transport properties using a ratio of finite determinants. In this paper and in Bose's code, a fourth order expansion was

deemed sufficient.

The equation used to calculate electrical conductivity is

$$\sigma = \frac{e^2 n_e [D_{ee}]_4}{kT_e} \quad (\text{IV.1})$$

$$[D_{ee}]_4 = \frac{3x_e}{2n} \left(\frac{2\pi kT_e}{m_e} \right)^{1/2} \frac{|q_{11}|}{|q|} \quad (\text{IV.2})$$

where $|q|$ is the determinant of the Sonine polynomial, $|q_{11}|$ is the first minor of the Sonine polynomial, x_e is the electron mole fraction, and n is total number density. $[D_{ee}]_4$ is defined as the fourth order electron-electron diffusion coefficient.

In order to calculate the determinants, it is first necessary to calculate the Sonine polynomials, which, in turn, depend on the collision cross sections. Bose's code uses different collision potentials for different type of collisions. The only gas which is examined in this study is argon, as that is the gas that was used in the experimental work of chapter III. For argon the following potentials are used to determine collision cross sections.

Neutral-neutral: exponential repulsive potential
 Electron-Neutral : experimental gas-kinetic cross sections
 Ion-Neutral: charge transfer cross sections
 Ion-Electron: attractive coulomb potential
 Ion-Ion: repulsive Coulomb potential
 Electron-Electron: repulsive Coulomb potential

For the remainder of this paper, the use of the term "Bose method" will refer to Bose's method of calculation of transport properties in a two temperature plasma according to kinetic theory.

IV.2 Caldo-Choueiri Calculation of Transport properties

Giuliano Caldo, Edgar Choueiri, Arnold Kelly and Robert Jahn at Princeton University have developed a numerical code for a two fluid case which takes anomalous transport into account self-consistently for the solution of a two-dimensional MPD thruster flow field [28,29]. It employs a modified finite difference MacCormack code for the solution of the two-fluid conservation equations, while simultaneously solving Maxwell's equations.

Several assumptions are made. First, the plasma is assumed fully ionized, so no neutrals are present. Also, it is assumed that each fluid obeys the ideal gas law separately. Flow is also assumed to be inviscid. The type of microinstability that is expected is the generalized lower hybrid drift instability, which operates at the lower hybrid frequency. Because ion trapping has been postulated to be the mechanism for non-linear saturation of this instability, the calculation of anomalous transport assumes that ion trapping is the means of saturation. Lastly, it is assumed that the flow can be modeled by a two fluid model as opposed to kinetic theory.

In addition, calculation of electrical conductivity uses the mean-free path formula to find an effective value of conductivity which accounts for anomalous transport, σ_{eff} :

$$\sigma_{eff} = \frac{e^2 n_e}{m_e (\nu_{ei} + (\nu_e^P)_{AW})} \quad (IV.3)$$

where $(\nu_e^P)_{AW}$ = the anomalous momentum exchange collision frequency. Note that only electron-ion collisions are accounted

for in determining conductivity if this formula is used: electron-electron and electron-neutral collisions are neglected. For the remainder of the paper, this method of calculation of both the classical and effective electrical conductivity will be referred to as the "mean free path method". The anomalous collision frequency is calculated using a curve fit based on calculations by Choueiri[4,28]:

$$\begin{aligned}
 (v_e^p)_{AV} = v_{e1} [& 0.192 + 0.033\Omega_e + 0.212\Omega_e^2 - 8.27 \times 10^{-5}\Omega_e^3 \\
 & + \frac{T_h}{T_e} (0.00123 - 0.0158\Omega_e - 0.00789\Omega_e^2)] \quad (IV.4)
 \end{aligned}$$

IV.3 Modification of Code

The key differences between the Bose method and the mean free path method used by Caldo and Choueiri are that the Bose method uses kinetic theory as opposed to fluid theory; a 4th order Sonine Polynomial expansion is used to calculate electrical conductivity rather than the mean-free path formula, and electron-electron and electron-neutral collisions are taken into account. However, Bose's computer code only calculates point transport properties. If Bose's computer code is modified for microinstabilities, it can be used as a subroutine in a numerical model such as that developed by Caldo and Choueiri in order to get a spatial mapping of transport properties. From this point on, the term "effective" will refer to properties which account for both classical and anomalous effects resulting from the presence of microinstabilities, while the term "anomalous" will

refer to effects stemming only from microinstabilities.

To account for microinstabilities, the collision cross-sections for electron-ion collisions were modified. This modification involves the use of the curve-fit in equation (IV.4) expressing the ratio of anomalous collision frequency to classical electron-ion collision frequency as a function of electron hall parameter. As Caldo and Choueiri used only the electron-ion collision frequency in determining the electron Hall parameter, this author has done the same to maintain compatibility in the results. In any event, for the conditions measured in the MPD thruster, the electron-heavy particle collision frequency is identical to the electron-ion collision frequency because no neutrals are present.

The lower hybrid wave typically has a phase velocity on the order of the ion thermal velocity [4]. Because electrical resistivity is effectively a measure of the "drag" on electrons, usually resulting from collisions, the interaction of the wave with electrons increases resistivity by increasing the "drag". In calculating the effective collision cross section from the collision frequency, the relative velocity between the wave and electrons must be used. However, as the electron thermal velocity is much larger than the wave velocity (ion thermal velocity), the relative velocity between the wave and electron was approximated by the electron thermal velocity. Lastly, since the electrons are the particles which are related to electrical conductivity, the number of electrons has a direct impact on the

collision frequency. Thus, using the formula,

$$\nu_{AN}^p = n_e V_{-e} Q_{AN}^p \quad (\text{IV.5})$$

where $Q_{AN}^p \equiv$ anomalous momentum transfer collision cross section, the anomalous collision cross section can be solved for based on the resulting value of anomalous collision frequency from the curve fit. This collision cross section is then superimposed on the electron-ion collision cross section to create an effective collision cross section. In order to calculate the transport properties by the Bose method for a two temperature plasma while accounting for microinstabilities, this cross section is used.

In order to calculate the transport coefficients according to the Bose method, collision cross section data for collisions which have different speed and angular dependencies than that based on a rigid-sphere model (the maximum cross section) are required for the Sonine polynomial expansion. These additional cross sections are available for use in the classical calculation of transport, but this body of data is non-existent for anomalous transport. A key assumption that was made in the modification of the cross sections to account for microinstabilities is that the additional cross sections used to determine effective electrical conductivity have a similar distribution to the distribution of the classical cross sections. As the Caldo-Choueiri curve fits produce a maximum cross section, the deviations from this cross

section were based upon the following scaling relation.

$$Q^{(1,3)}_{eff} = \frac{Q^{(1,3)}_{cl}}{Q^{max}_{cl}} Q^{max}_{eff} \quad (IV.6)$$

In this equation, $Q^{(1,3)}_{eff}$ = the modified "effective" collision cross section accounting for deviations from the rigid sphere model, $Q^{(1,3)}_{cl}$ = the experimentally determined classical cross sections which deviate from the rigid sphere model, Q^{max}_{cl} = the maximum classical cross section (the one corresponding to a rigid sphere model), and Q^{max}_{eff} = the cross section calculated directly from equations (IV.4) and (IV.5). It must be noted that until reliable values of cross sections used in the Sonine polynomial expansion for anomalous cross sections can be determined experimentally, the results shown in this paper have a degree of uncertainty which cannot be quantified. However, this is the best approximation that can be made at the current time.

In addition, it should be noted that this modification of collision cross-section is only good for wave-electron interactions. If the same method is attempted for modification of wave-ion or wave-neutral interactions, the effective collision cross sections can become extremely large because ions and neutrals move at almost the same speed as the lower hybrid wave, resulting in a relative velocity of zero. To calculate the effective cross section from the Caldo-Choueiri curve fits, the collision frequency must be divided by the relative velocity. This would introduce an almost infinite collision cross section.

This makes sense for ions. The Caldo-Choueiri curve fits

assume that ion trapping is the means of damping the collisions. As a result, the ions do experience an infinite collision cross section with the wave because they cannot escape from it; they are "trapped". However, neutrals should not experience this same effect because there is no net charge on the neutrals, so a potential well should not be able to trap them as easily.

IV.4 Comparison of Results

IV.4.1 Comparison between mean free path and Bose methods

To get an accurate comparison of the mean free path and Bose methods of calculating electrical conductivity, the number densities of each species must be kept the same, regardless of method of calculation. This leads to the use of only one method of calculating the species composition of the gas. Although the mean-free path method only requires the electron number density, heavy species number densities are required for the Bose method. Therefore, the method of calculating species composition of the gas which was used in Bose's computer code was also used to determine species number densities for the mean-free path method as well as the Bose method.

The electrical conductivities calculated by both the Bose and mean-free path methods were calculated for a variety of conditions. The pressure was held approximately constant, while the electron temperature and ratio of electron-to heavy particle temperatures were varied. The range of electron temperatures spanned from 5000 K to 35000 K, and the temperature ratios

spanned from .5 to 1.8. A plot of electrical conductivity vs. electron temperature is shown in figure IV.1 for a one-temperature plasma, Hall parameter of 1, and pressure of 10 Pa.

Examining this figure, one may notice the discontinuities in the electrical conductivities at a few temperatures, regardless of the method of calculation used. As Bose's code takes into account multiply ionized species, there are some discontinuities in electrical conductivities at temperatures where the primary heavy species changes ionization levels. This is the reason for local peaks in the distribution of electrical conductivity vs. temperature.

Looking at the case involving the mean free path method, one can see that the difference between classical and electrical conductivity appears to increase with higher temperature. However, if the ratio of effective to classical conductivity is examined, as shown in figure IV.2, the ratio is constant throughout the entire temperature range, showing the effective conductivity to be approximately 30 per cent lower than the classical conductivity. The reason that this ratio does not vary is that there is no explicit absolute temperature dependence in the calculation of the anomalous collision frequency. Although electron temperature has an effect on the electron-ion collision frequency used in determination of electrical conductivity, this factor is present in both effective and classical conductivity calculations, and cancels out when a ratio is taken.

In contrast, absolute temperature does play a significant

role in the ratio of effective to classical conductivity using the Bose method of calculating transport properties. Comparing these results to the results from the mean-free path method in figure IV.1, one can see that the electrical conductivities follow the same general trend regardless of the method used. That is, both methods show an increase in electrical conductivity with temperature and both methods show local peaks resulting from transition in ionization state of the primary heavy species. However, the absolute values of classical and effective electrical conductivities calculated by the Bose method are both higher than for both the classical and effective values calculated by the mean-free path method.

This discrepancy is due to the methods being used to calculate the conductivity. Mitchener and Kruger state that the mean-free path formula gives a good order of magnitude estimate of electrical conductivity, but can be off by as much as a factor of two [32]. They also state that better values can be obtained by using Sonine polynomial approximations [32]. The higher order the Sonine polynomial approximation, the more accurate the result. However, the Sonine polynomials converge fairly rapidly, so the fourth order approximation used by Bose in the calculation of electrical conductivity is fairly close to the exact result. Examining Figure IV.1 again, it can be seen that the discrepancies between the classical values of electrical conductivity differ by a factor no greater than 2, which is within the uncertainty of the mean-free path formula.

However, the effective conductivity based on the Bose method behaves much differently than that calculated by the mean free path method. In the mean free path method, the effective conductivity diverges from the classical conductivity slightly with increasing temperature, but as explained earlier, this is due to the constant ratio between effective and classical conductivities. In contrast, for the Bose method, the curves actually converge. The effect on the ratio of effective to classical electrical conductivity can be seen figure IV.2.

At first glance, these results appears strange. The same curve fit for anomalous collision frequency was used as the basis for calculations of effective conductivity in both the mean free path and Bose methods. However, the curve fit had no absolute temperature dependence. Thus, one may wonder why the results using the Bose method show a clear temperature dependence.

The answer lies in the interactions which were accounted for in the Bose method, which were not accounted for by the mean free path method. The mean free path method took only electron-ion interactions into account in the determination of electrical conductivity. One reason Caldo and Choueiri limited the scope of their analysis using the mean free path method is because of the assumption that the anomalous effects are a result of ion-electron interactions only, provided ion trapping is the dominant mode of saturation of microinstabilities [28].

The Bose method takes into account several other interactions, though: electron-electron, electron-neutral, ion-

neutral, ion-ion, and neutral-neutral in addition to electron-ion interactions. It appears that these effects "dilute" the effects of the anomalous collision frequency. One may think of the effect of accounting for additional interactions as one may think of adding dye to a glass of water.

Suppose a glass contained some water, and some red dye was added to it so that whatever the initial amount of water, the color of the water would be the same immediately after the dye was added, say a bright red. However, as more and more water is added, the dye becomes harder to see. Using this analogy, the dye represents the effects of anomalous collision frequency, and the additional water represents additional collision types which are accounted for. Obviously, if these additional collision effects are very small compared to the original collisions which are accounted for, the effect of accounting for these collisions will not be very great, just as adding only a little water to the dyed water may not noticeably change the color. However, as these interactions become more significant, the anomalous effects which are associated with only one type of interaction (electron-ion) are less noticeable. Using the above analogy, the color of the water becomes noticeably dimmer. Eventually, enough water may be added such that the dye cannot be seen at all.

This is what happens at very high and at very low temperatures in the MPD thruster plasma. At lower temperatures (about 5000 K), the plasma is only very weakly ionized; in other words, neutrals are the primary species, so electron-neutral,

neutral-neutral, and ion-neutral collisions will dominate the plasma. Electron-ion collisions are very insignificant compared to these interactions because both ion and electron mole fractions are extremely low. As a result, the ratio of effective to classical conductivity should be one. Once again examining figure IV.2, this can be seen to be the case.

However, as the plasma becomes fully ionized, the neutral mole fractions approach zero, and all collisions involving neutrals become negligible. In contrast, the mole fractions of both ions and electrons increase significantly. Around 1 eV, or 11600 K, the mole fractions of ions and electrons are roughly equal. Thus, at this point, electron-electron, electron-ion, and ion-ion interactions are significant, although electron-ion effects should be dominant due to the much larger cross sectional area of an ion as opposed to an electron. In addition, as electrical conductivity involves electrons, the ion-ion interactions are not very important in comparison to the other two interactions. Thus, the effective conductivity should be much lower at this temperature range. Once again, figure IV.2 shows that the ratio of conductivities drops to a much lower value, and it almost reaches the level of the ratio predicted by Caldo and Choueiri. The difference between the two ratios at this fully ionized stage is due to the electron-electron interactions accounted for in the Bose method which are not accounted for in the mean free path method.

However, as the plasma becomes even more highly ionized, the

ratio of conductivities according to the Bose method starts to increase, reaching about 0.92 at about 3 eV (34,800 K). As neutrals are even less likely at these temperatures, some type of interaction must be becoming more important than electron-ion interactions. These dominating interactions are electron-electron collisions. As the plasma becomes more highly ionized, more electrons are present for each ion, so the electron mole fraction increases, while the heavy particle mole fractions decrease. Therefore, if the temperature is raised high enough, electron-ion interactions will be so small compared to electron-electron interactions that anomalous effects will no longer be noticeable.

The effects of Hall parameter on the effective and classical conductivities are shown in Figure IV.3, for a single temperature plasma at 10 Pa, and electron temperature of 31500 K. Unlike the classical case, the Hall parameter has a noticeable effect on the effective electrical conductivity for both methods of calculation. As the Hall parameter increases, the effective conductivity drops. This result makes sense because equation (IV.4) has a strong dependence on Hall parameter.

The ratios of effective to classical electrical conductivity for the above conditions are plotted vs. Hall parameter in Figure IV.4. From this plot it is clear that although electrical conductivity drops significantly with Hall parameter regardless of the method used, this drop is much less drastic if the Bose method is used. This in turn means that electron-electron

collisions appear to have a significant mitigating effect on effective conductivity at low to intermediate values of Hall parameter, although this mitigating effect diminishes at very high values of the Hall parameter. The mean free path case matches the results shown by Caldo and Choueiri [2,4,28], albeit in slightly different form.

The effects of temperature ratio will be discussed in the next section.

IV.4.2 Illustrative Example

Using data acquired at different locations inside the thruster through the experiments described in chapter III, the Bose code was applied to determine electrical conductivity. In the experimental work, microinstabilities were not seen at any locations. However, assuming microinstabilities exist at these locations, the following illustration will show the differences in conductivities which occur due to anomalous effects at two different locations in the thruster and its plume.

The two locations selected had the following properties:

Point #1:

Position: 7.7 cm from the back plate, 2.5 cm from thruster axis.
Pressure = 22 Pa.
Electron Temperature = 31500 K.
Magnetic Field = 17 Gauss.
Hall Parameter = .014

Point #2:

Position: 4.7 cm from the back plate, 1.5 cm from the thruster axis.
Pressure: 57.5 Pa
Electron Temperature = 48200 K
Magnetic Field = 224 Gauss.

Hall Parameter = .128

The pressures were chosen so as to match the measured electron number density assuming a single temperature plasma. In terms of the positions in relation to the thruster electrodes, point #1 was about halfway between the electrodes in the radial direction, and about 3 cm beyond the exit plane of the thruster. Point #2 was located fairly close to the tip of the cathode. These points were chosen because they were close enough to the axis where error in the alignment of the probes would not be as great, they were positions which were believed to have produced good data, and point #2 corresponded to the location where there is a very slight possibility that some lower hybrid oscillations may have occurred.

Figure IV.5 shows plots of the classical conductivities vs the temperature ratio, T_e/T_i . As can be seen for the classically calculated values, deviations of temperature ratio from unity result in higher electrical conductivities. In addition, the conductivities calculated by the different methods differ by a factor of approximately two. Figure IV.6 shows the effective conductivities vs. the temperature ratio. Figures IV.5 and IV.6 are virtually identical with the exception that all values of conductivity for both thruster locations are lower for the effective cases.

To see the effect that temperature ratio has on effective conductivity, one may look at Figure IV.7, a plot of the ratio of effective to classical conductivity vs. temperature ratio for

both thruster locations. As can be seen, neither method shows much variation at these locations for either case. The only noticeable effect is that the mean free path method predicts that conductivity will be approximately 12 per cent lower than for the Bose method at these points. Higher or lower temperature ratios will, of course produce greater effects on these ratios of conductivity; however, the temperature ratios shown are indicative of those occurring in an MPD thruster. Although temperature ratio does have a small effect on the effective conductivity, examination of figure IV.5 seems to indicate that the classical effects of temperature ratio are much more significant than any effects temperature ratio has on anomalous transport.

One may note that both of these locations are characterized by fairly low Hall parameters and rather high electron temperatures and number densities. As anomalous transport seems most strongly related to Hall parameter, it appears that in high power devices such as the one used in this work, anomalous transport may not have much of an effect. However, this analysis seems to show that the observable effects of anomalous transport at high power levels are less if the Bose method is used than if the mean free path method is used. In a spatial sense, however, effective conductivity calculated by the Bose method seems to exhibit more of a spatial dependence than that calculated by the mean free path method. This dependence is evidenced by the larger separation between curves representing different locations

in Figure IV.7 for the Bose case than for the mean free path case.

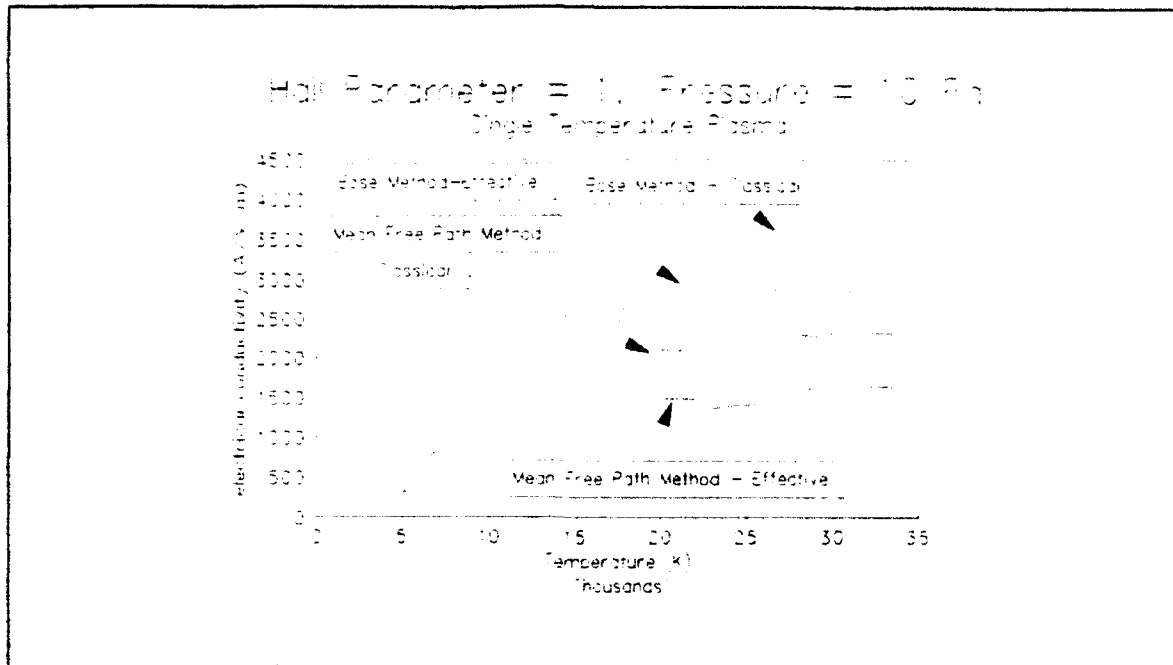


Figure IV.1 - Electrical Conductivity vs. Electron Temperature for a one temperature plasma at a pressure of 10 Pa. Results for both effective and classical results based on both the Bose and mean free path methods are shown.

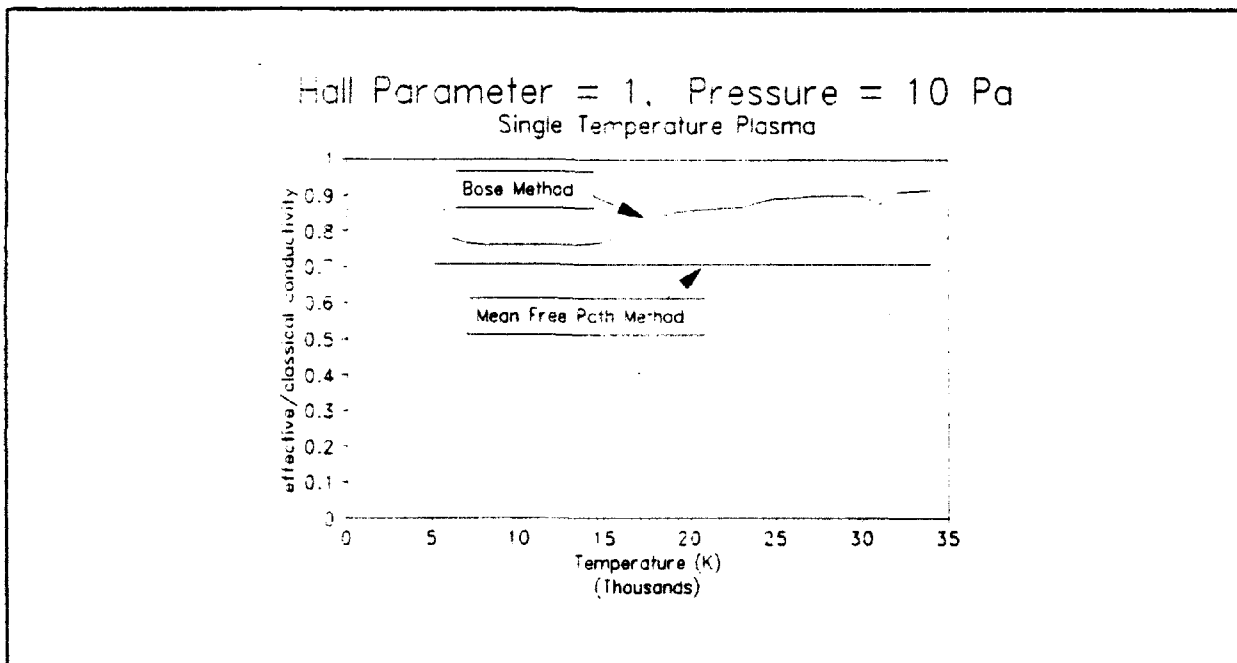


Figure IV.2 - Ratio of effective/classical electrical conductivity vs. electron temperature for both the Bose and mean free path methods.

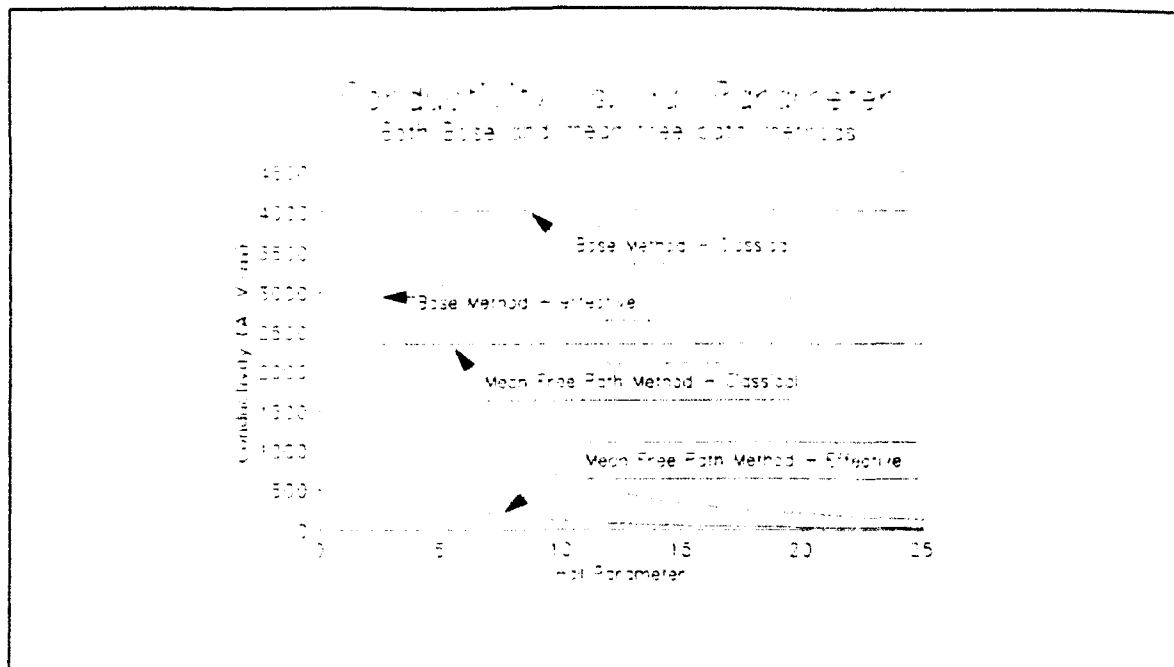


Figure IV.3 - Electrical conductivity vs. Hall parameter for a one temperature plasma at a pressure of 10 Pa. Results for both the Bose and mean-free path methods are shown.

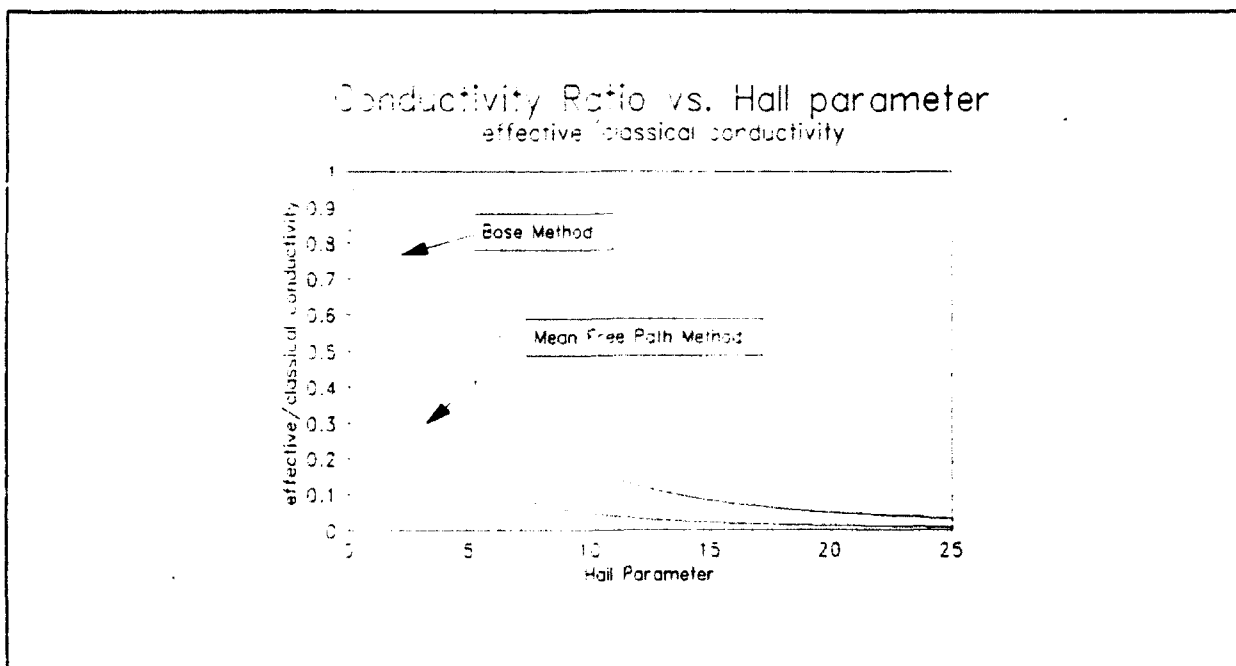


Figure IV.4 - Ratio of effective to classical conductivity vs. Hall parameter for pressure = 10 Pa, single temperature plasma at 31500 K. Both the Bose method and mean free path method are shown.

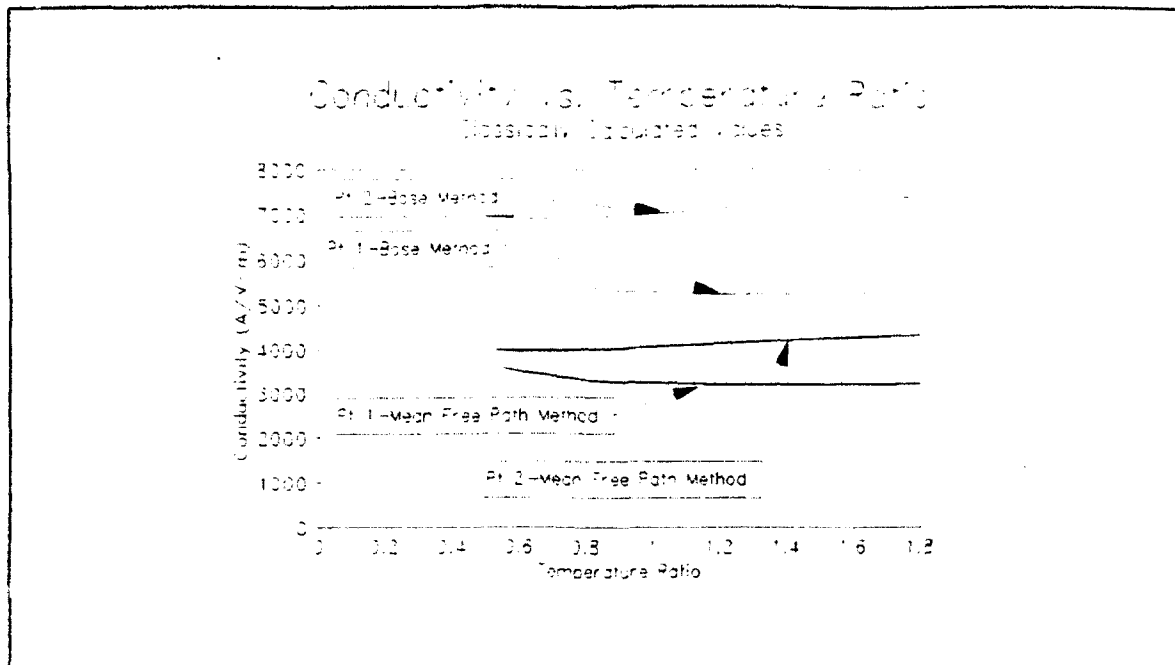


Figure V.5 - Classical electrical conductivities vs. ratio of electron to heavy particle temperature by both the Bose method and mean free path method. Point 1 and Point 2 are two different locations in the thruster.

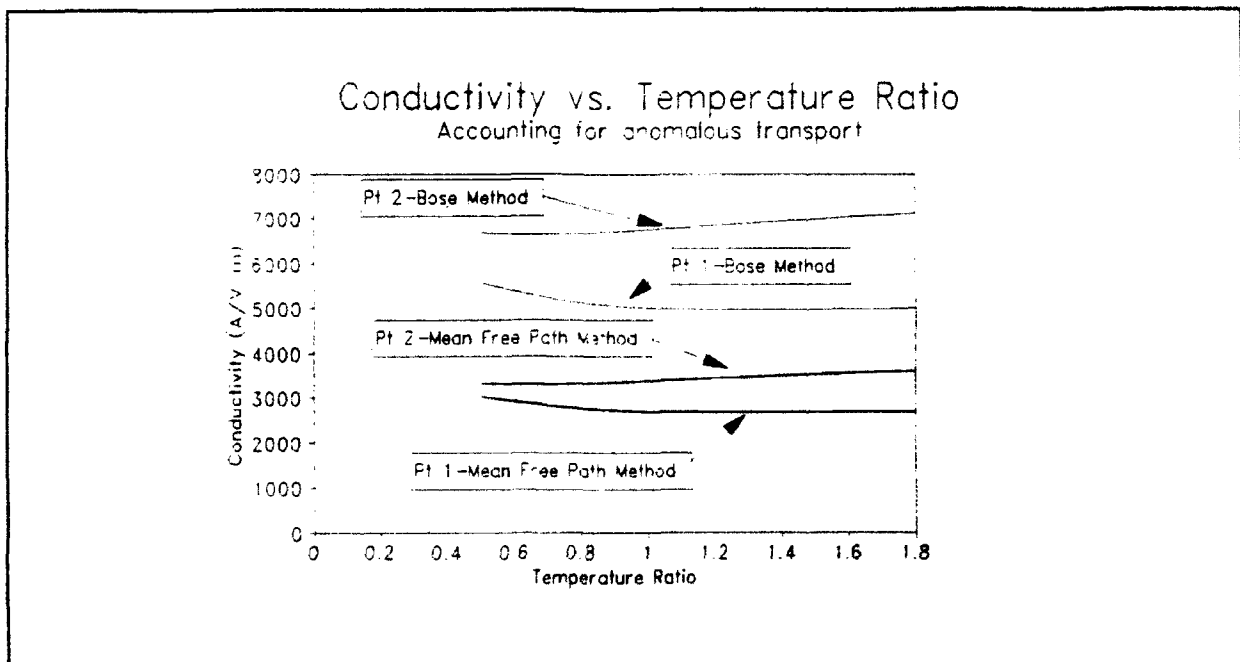


Figure IV.6 - Effective electrical conductivity vs. ratio of electron to heavy particle temperature by both Bose and mean free path methods. Point 1 and Point 2 are two different locations in the thruster.

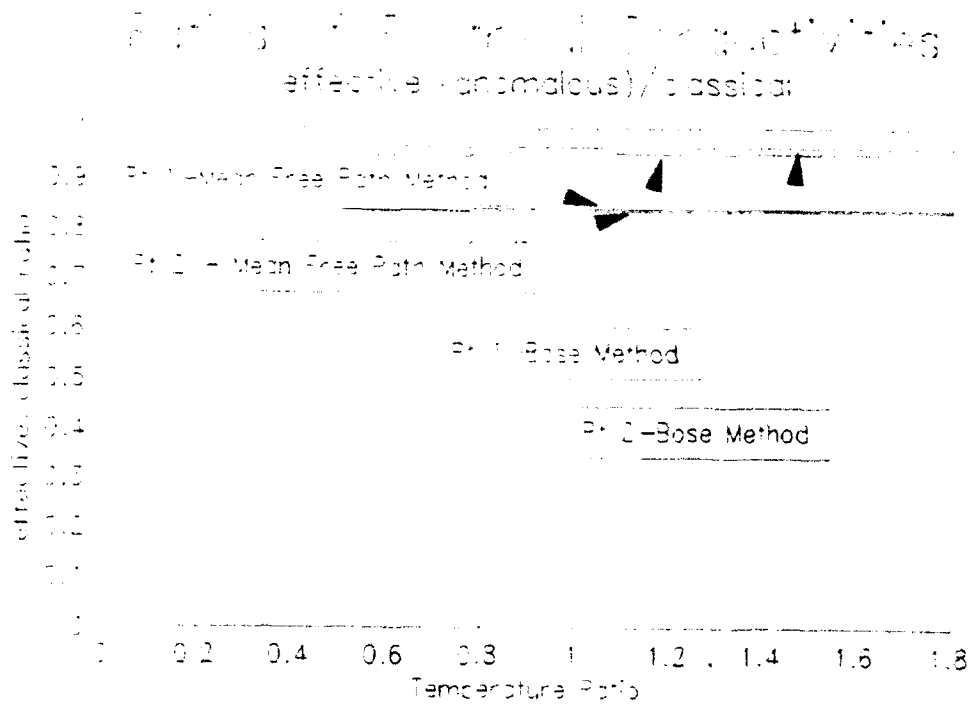


Figure IV.7 - Ratio of effective to classical electrical conductivity vs. ratio of electron to heavy particle temperature. Point 1 and Point 2 are two different thruster locations.

V. Discussion and Recommendations

V.1 Tentative Conclusions

Some tentative conclusions may be drawn from both the experimental and theoretical results of this work.

1) Microinstabilities do not seem to occur anywhere in the MW level thruster at operating conditions slightly below onset; however, much lower frequency instabilities do appear to exist, and are probably related to onset. Investigations at different power levels and repeatability studies are required to determine if the lack of microinstabilities is a function of high power devices in general, a function of operating at conditions closer to onset than attempted in previous work [1,30], or just an erroneous test run.

2) Unlike the situation where a "stinger" is introduced into an MPD flow field, which delays onset[40], it appears that the insertion of electrical conductors into the flow field near the anode acts to induce onset.

3) Effective conductivity appears to have an indirect temperature dependence which is greater than its direct dependence on temperature ratio and Hall parameter. This temperature dependence results from a variance in species number densities with temperature and does not seem to arise unless electron-electron and electron-neutral interactions are taken into account.

4) Finally, for conditions which appear to be present inside a MW level MPD thruster and in its near plume, the effect of

anomalous transport induced by lower hybrid microinstabilities seems to be less significant than had been anticipated. Assuming that ionization occurs according to classical methods, if microinstabilities are present there is only a small reduction in conductivity for conditions present in a MW level device, on the order of a 5 per cent. It must be kept in mind, however, that if ionization does not occur according to classical methods, the effect of anomalous transport may be as great as anticipated.

V.2 Recommendations

In the realm of experimental work, many improvements can be made. First and foremost, the effect of power level on microinstabilities needs to be investigated, as well as verification of the results presented in this paper. Secondly, a means of aligning a Langmuir probe with the flow will greatly increase the accuracy of measurements of mean electron temperature and electron number density. Thirdly, a study of the perturbation effects of an electrical conductor placed in the current paths of the thruster would help make evaluation of any interior thruster data more accurate. Fourth, the use of a large number of replacement probes when taking measurements inside the thruster would greatly reduce the problems involved with probe contamination. Finally, if microinstabilities are detected at different power levels in this device, phase and wavelength data would complement the frequency data to perhaps identify specifically which microinstability was operating.

On the theoretical side of this paper, although the Bose method shows clearly the effect of accounting for different types of collisions throughout the entire range of temperatures likely to be seen in an MPD thruster, a small modification of the mean free path method used by Caldo and Choueiri method could increase the applicability of their results while increasing the work infinitesimally. This modification would be to account for electron-electron collisions in the mean-free path formula. Rule of thumb formulas for electron-electron collision frequency are available from many sources, such as Mitchener and Kruger [32], and Chen[6]. The electron-ion and electron-electron collision frequencies may be added by superposition to yield an electron collision frequency. However, just adding this term will only work well only in the fully, but singly, ionized regime. In addition, if absolute values of conductivity are desired, whether classical or effective, the values may still be off by as much as a factor of 2.

If only the relationship between anomalous and classical transport is desired in all regimes, not absolute values, a compromise between the Bose method and Caldo method can be used to reduce the work involved in the Bose method. If the electron-electron collisions are accounted for as explained in the above paragraph, the mean free path formula for conductivity can be used and produce a good deal of accuracy in determining the effect of anomalous effects on transport. However, the mole fractions of neutrals and multiply ionized ions must be

calculated by some means. As MPD thrusters almost always operate in the fully ionized regime, neutrals can be neglected for practical comparisons. The multiply ionized mole fractions are necessary because they are directly linked to increases in electron mole fractions at higher temperatures.

Unfortunately, if absolute values of electrical conductivity are desired as well as determining the effects of anomalous transport, the method used in this paper is probably required. It takes a good deal more time to calculate results, as well as being difficult to understand, but it accounts for almost all interactions while providing fairly accurate results for both classical and effective electrical conductivity.

If some slight modifications are made to this method, the effects of anomalous transport on other transport properties which involve electron-ion interactions, such as thermal conductivity and diffusion, could probably be accounted for fairly easily. This is because the Bose method calculates all transport properties based on collision cross sections, and the cross-sections for electron-ion collisions have already been modified for anomalous effects to find electrical conductivity. The calculation of other transport properties was not attempted in this paper because one of the major aims was to compare the effects of the method of calculation on determining the effects of anomalous transport, and this author has not seen any work done by others regarding the effect of anomalous transport on transport properties other than electrical conductivity in an MPD

thruster. However, for some quantities which rely on collisions transferring energy rather than momentum, a different curve fit must be used. Such a curve fit is also shown in Caldo and Choueiri's paper [28,29], so modification of this method would not be too difficult. Using this curve fit, they have examined ion heating due to anomalous transport. To make these type of calculations may be something for the interested researcher to attempt.

To have more confidence in the results from the method used in this paper, it would be necessary to get cross section data while anomalous effects (i.e microinstabilities) are present, experimentally. Although microinstabilities were not seen at the higher power levels examined in this experimental work, others [17] at Princeton University have seen them at lower power levels, and Caldo and Choueiri have predicted where they should occur theoretically. Collision cross sections to account for anomalous effects should be measured in the regions shown by the Princeton work, both experimental and theoretical, in order to more accurately predict anomalous transport properties.

Lastly, the means of ionization in the MPD plasma needs to be determined. If it appears to occur according to classical methods, no further modification to this method other than what is mentioned above should be necessary. However, if anomalous ionization occurs, the portion of the Bose method which calculates the quasi-equilibrium species compositions must be modified to account for anomalous ionization.

REFERENCES

1. Tilley, Dennis L. An Investigation of Microinstabilities in a kW level Self-Field MPD Thruster. Masters Thesis, Princeton University, October 1991.
2. Choueiri, Edgar Y. "An Introduction to the Plasma Physics of the MPD Thruster." Lecture Notes for MAE 538, Physics of Electric Propulsion, Princeton University, November 1991.
3. Sovey, J.S. and Mantieniks, M.A. "Performance and Lifetime Assessment of MPD Arc Thruster Technology". Journal of Propulsion and Power, Vol 7, No. 1, 1991, pp. 71-83.
4. Choueiri, Edgar Y. Electron-Ion Streaming Instabilities of an Electromagnetically Accelerated Plasma. Ph.D. Thesis, Princeton University, October 1991.
5. Tilley, Dennis L. Telephone Interview. 7 May 92.
6. Chen, Francis F. Introduction to Plasma Physics and Controlled Fusion. Volume 1: Plasma Physics. New York: Plenum Press, 1984.
7. Cap, F. Handbook on Plasma Instabilities, Vol. 1. New York: Academic Press, 1978.
8. Boyle, M.J., Clark, K.E., and Jahn, R.G. "Flowfield Characteristics and Performance Limitations of Quasi-Steady Magnetoplasmadynamic Accelerators." AIAA Journal. Vol 14., No. 7, July 1976. pp. 955-962.
9. Malliaris, A.C., John, R.R., Garrison, R.L., and Libby, D.R. "Performance of Quasi-Steady MPD Thrusters at High Powers." AIAA Journal. Vol. 10, No. 2, Feb 1972, pp. 121-122.
10. Rempfer, D., Auweter-Kurtz, M., Kaeppler, H.J., and Maurer, M. "Investigation of Instabilities in MPD Thruster Flows using a linear dispersion relation." IEPC Paper No. 88-071, 20th International Electric Propulsion Conference, October 3-6, 1988.
11. Murthy, S.N.B., Shoureshi, R., and Pourki, F. "An Approach to MPD Engine Instabilities." AIAA Paper No. 87-0384, 25th Aerospace Sciences Meeting, Jan 12-15, 1987.
12. Schiele, H.O., Auweter-Kurtz, M, and Kurtz, H.L. "Stability Problems in Magneto Plasmadynamik ARC Thrusters." AIAA Paper No. 85-1633, 18th Fluid Dynamics and Plasmadynamics and Lasers Conference, July 16-18, 1985.

13. Wagner, Henri P., Auweter-Kurtz, Monika, Roesgen, Thomas, Messerschmid, Ernst W., and Kaeppler, H.J. "Gradient Driven Instabilities in Stationary MPD Thruster Flows." AIAA Paper 90-2603, 21st International Electric Propulsion Conference, July 18-20, 1990.
14. Wagner, Henri P., Auweter-Kurtz, Monika, Messerschmid, Ernst W., and Kaeppler, H.J. "Gradient Influenced Space Charge Instabilities in MPD Thrusters." IEPC Paper No. 91-101, 22nd International Electric Propulsion Conference, Oct. 14-17, 1991.
15. Kuriki, K. and Iida, H. "Spectrum Analysis of instabilities in MPD Arcjet." IEPC Paper No. 84-28, 17th International Electric Propulsion Conference, Tokyo, Japan, 1984.
16. Mikhailovskii, A.B. and Timofeev, A.V. "Theory of cyclotron instability in a non-uniform plasma." Soviet Physics JETP, Vol 17, No. 3, Sep. 1963, pp. 626-627.
17. Aref'ev, V.I. "Instability of a Current-Carrying Homogenous Plasma." Soviet Physics-Technical Physics, Vol. 14, No. 11., May 1970.
18. Lashmore-Davies, C.N. "Instability in a Perpendicular Collisionless Shock Wave for Arbitrary Ion Temperature." Physics of Fluids, Vol. 14, No. 7, July 1971, pp. 1481-1484.
19. McBride, John B., Ott, Edward, Boris, Jay P., and Orens, Joseph H. "Theory and Simulation of Turbulent Heating by the Modified Two Stream Instability." Physics of Fluids, Vol. 15, No. 12, December 1972. pp. 2367-2383.
20. Aref'ev, V.I. and Chernov, A.A. "Anomalous resistivity of a transverse plasma current at electron-cyclotron harmonics." Soviet Physics-Technical Physics, Vol. 19, No. 12, June 1976, pp. 1522-1528.
21. Shishkin, G.G. and Gerasimov, V.F. "Plasma instabilities in accelerators with closed electron drift." Soviet Physics-Technical Physics, Vol. 20, No. 9, Sep. 1977, pp. 1171-1174.
22. Davidson, R.C., Gladd, N.T., Wu, C.S., and Huba, J.D. "Effects of finite plasma beta on the lower-hybrid drift instability." Physics of Fluids, Vol. 20, No. 2, Feb. 1977, pp. 301-310.
23. Gladd, N.T., and Huba, J.D. "Finite beta effects on the drift-cyclotron instability." Physics of Fluids, Vol 22, No. 5, May 1979, pp. 911-22.
24. Hsia, J.B., Chiu, S.M., Hsia, M.F., Chou, R.L., and Wu, C.S.

- "Generalized lower-hybrid-drift instability." Physics of Fluids, Vol 22, No. 9 Sep 1979, pp. 1737-1746.
25. Wu, C.S., Zhou, Y.M., Tsai, S.T., Guo, S.C., Winske, D., and Papadopoulos, K. "A kinetic cross-field streaming instability." Physics of Fluids, Vol. 26, No. 5, May 1983, pp. 1259-1267.
 26. Hastings, David E. and Niewood, Eli. "Theory of a Modified Two-stream Instability in a Magnetoplasmadynamic Thruster". Journal of Propulsion and Power, Vol. 7, No. 2, 1990, pp. 258-268.
 27. Niewood, E.H., Preble, J., Hastings, D.E., and Martinez-Sanchez, M. "Electrothermal and Modified Two-Stream Instabilities in MPD Thrusters." AIAA Paper No. 90-2607, 1990.
 28. Caldo, Giuliano, Choueiri, Edgar Y., Kelly, Arnold J., and Jahn, Robert G. "An MPD Code with Anomalous Transport.", IEPC 91-102, 22nd International Electric Propulsion Conference, October 14-17, 1991.
 29. Caldo, Giuliano, Choueiri, Edgar Y., Kelly, Arnold J., and Jahn, Robert G. "Numerical simulation of MPD thruster flows with Anomalous Transport." AIAA Paper No. 92-3738, 28th Joint Propulsion Conference, July 6-8, 1992.
 30. Diamant, K. "Anode Region Wave Processes." MAE 1776.35 Electric propulsion Laboratory, Progress report, Princeton University, January-February 1992.
 31. Tilley, D.L., Choueiri, E.Y., Kelly, A.J., and Jahn, R.G. "An Investigation of Microinstabilities in a kW level Self-Field MPD Thruster." IEPC Paper 91-122, 22nd International Electric Propulsion Conference, October 14-17, 1991.
 32. Mitchener, M. and Kruger, Charles H. , Jr. Partially Ionized Gases. New York: John Wiley & Sons, 1973.
 33. Choueiri, E.Y., Kelly, A.J., and Jahn, R.G. "MPD Thruster Plasma Instability Studies." AIAA Paper 87-1067, 19th International Electric Propulsion Conference, May 11-13, 1987.
 34. Castillo, Salvador, Capt., USAF. Establishment of MPD Performance. Philips Laboratory Final Report, December 1991.
 35. Tilley, D. L., Kelly, A.J., and Jahn, R.G. "The Application of the Triple Probe Method to MPD Thruster Plumes." AIAA Paper, 1990.

36. Peterson, E.W. and Talbot, L. "Collisionless Electrostatic Single Probe and Double Probe Measurements." AIAA Journal, Vol. 8, No. 12, 1970, pp. 2215-2219.
37. Chen, Francis F. "Electric Probes." Plasma Diagnostics. ed. Huddleston and Leonard, 1965, pp. 113-200.
38. Clark, K.E., DiCapua, M.S., Jahn, R.G. "Quasi-steady Magnetoplasmdynamic Arc Characteristics." AIAA Paper 70-1095, AIAA 8th Electric Propulsion Conference, 31 Aug-2 Sep, 1970.
39. Boyle, M.J. Clark, K.E., and Jahn, R.G. "Flowfield Characteristics and Performance Limitations of Quasi-Steady Magnetoplasmdynamic Accelerators." AIAA Journal, Vol. 14, No. 7, July 1976.
40. Rudolph, L.K., Jahn, R.G., Clark, K.E., and von Jaskowsky, W.F. "Onset Phenomena in Self-Field MPD Arcjets. AIAA Paper 78-653, 13th International Electric propulsion Conference, 25-27 Apr 1978.
41. Tahara, H., Yasui, H., Kagaya, Y., and Yoshikawa, T. "Experimental and Theoretical Researches on Arc Structure in a Self-Field Thruster." AIAA Paper 87-1093, 19th International Electric Propulsion Conference, 11-13 May 1987.
42. Bose, Tarit K. "Thermophysical and Transport Properties of Multi-Component Gas Plasmas at Multiple Temperatures." Progress in Aerospace Sciences, Vol. 25, 1988, pp. 1-42.
43. Bose, Tarit K. "Two Temperature Gas Plasma Properties." Computer Code, Version 1987.
44. Monti, R. and Napolitano, L.G. "Generalized Saha Equation for non-equilibrium two-temperature plasma." XV International Astronautical Conference, 1964, pp. 517-537.
45. Veis, S. "The Saha equation and lowering of the ionization energy for a two-temperature plasma." Proceedings of the Czechoslovak Conference on Electronics and Vacuum Physics, 1968, pp. 105-109.
46. Tilley, Dennis L. Telephone Interview. 3 Nov 92.
47. Hirschfelder, J.O., Curtiss, C.F., and Bird, R.B. Molecular Theory of Gases. John Wiley & Sons, 1956.
48. Botticher, W. "Measurement of Magnetic Fields in Plasmas". Plasma Diagnostics, New York: John Wiley and Sons, 1968, pp. 617-665.

49. Lovberg, R.H. "Magnetic Probes." Plasma Diagnostics, ed. Huddleston and Leonard, 1965, pp. 69-112.

APPENDIX AFacility

The pulsed multi-megawatt MPD facility, known as chamber #2 at the United States Air Force Philips Lab-Electric Propulsion Laboratory, consists of a power supply and conditioning system, vacuum pumping equipment, propellant flow system, and a pulsed magnetoplasmadynamic (MPD) thruster.

A.1 Vacuum Equipment:

The chamber is a 2.438 m (8 ft) diameter by 3.658 m (12 ft) long stainless steel cylinder. It has one door and 6 view ports. Four of these viewports are transparent, allowing for visual observation of the thruster both directly and with the aid of a mirror placed inside the chamber. The other two are occupied by interfaces which equipment is plugged into. A diagram of the setup is shown in figure A.1 [34].

The equipment to produce the near-vacuum in the chamber are a Stokes 412H-10 Mechanical Pump, a Roots 615 RGS Blower, and two Varian 0185 .3048 m (12 inch) diffusion pumps. These pumps can reduce the chamber pressure to 0.006666 Pa (5×10^{-5} Torr). After .6 g of argon is exhausted by the thruster, the chamber can return to this pressure in 5 minutes [34].

A.2 Propellant Feed system:

The propellant system consists of a 9.232 m³ (326 ft³) argon T-bottle and regulator, with .793 m³ (28 ft³) bottles of

hydrogen, helium, neon, xenon, and krypton also plumbed into the system [1]. The propellant lines feed into a $.02367 \text{ m}^3$ (.8359 ft^3) plenum located outside the chamber. A thermometer at the plenum takes the temperature of the argon. The pressure drop per gas pulse is also measured here, giving the mass flow at the plenum. A solenoid valve allows the gas to enter the thruster when firing.

A.3 Power Supply and Conditioning:

A Del Electronics Corp. HPS-1-8000-3 power supply provides up to 8 kW of Power to a Pulse Forming Network (PFN). The PFN is a ten-section LC (Inductor-Capacitor) Network with a nominal output impedance of 0.01Ω . Each section consists of three 2000 μF Maxwell 33800 capacitors connected in parallel. With the addition of a 5 turn, $0.53 \mu\text{H}$ inductor in each section, the network will produce a 1 millisecond current pulse at up to 40 kA and 400 V to the thruster assuming a perfectly matched load [34]. The power supply is isolated from the PFN once the PFN has acquired the desired voltage level. A schematic diagram of the pulse forming network is shown in figure A.2.

A high voltage power supply (low current) provides the voltage for the spark trigger. Typically, it is operated at between 700-1000 volts. It is connected to a tungsten wire and the cathode of the thruster by means of a mechanical high voltage relay when the thruster is fired.

A.4 Timing and control:

Timing and control are accomplished through the use of a pushbutton control panel, Tektronix PEP-301 IBM compatible microcomputer, and two Rapid Systems 4000 timing boxes. The PFN is connected to the high voltage power supply by a relay controlled through pushbuttons on the control panel. A potentiometer is used to control the power supply voltage, and in turn the PFN voltage. Once the PFN is at the desired level, the power supply is disconnected.

The microcomputer has two pulse types stored in a file, one for the gas pulse, and another for the spark trigger. The gas pulse is eighty milliseconds long, and the spark trigger pulse lasts two seconds. The spark trigger also incorporates a 20 millisecond delay after the gas pulse is initiated. These files are downloaded into the timing boxes which produce the desired pulses. Both pulses are initiated when the fire button is depressed.

A.5 Thruster

The thruster itself is a self-field magnetoplasmadynamic (MPD) thruster. The annular copper anode has a 10.2 cm (4 inch) outer diameter and a 7.62 cm (3 in) inner diameter, with a length from injection plate to end of 3.81 cm (1.5 in). The boron-nitride injection plate fits snugly against the anode surface, and has a half inch radial displacement from the 1.27 cm (0.5 in) diameter, thoriated tungsten cathode. The tip of the cathode is

.635 cm (.25 in) from the end of the anode in an axial direction. Some photographs of the thruster are shown in figure A.3.

The entire thruster is imbedded in a plexiglass mounting which may swing in the axial direction or remain fixed depending on the operator's preferences. An accelerometer may be imbedded in the plexiglass to make measurements as well. The propellant lines are inserted into the rear of the thruster. The PFN is connected to the thruster by means of a copper cross attached to the cathode with a screw, and loops of copper wire pressed against the anode by a metal plate, attached to the anode with screws. In addition, a tungsten wire protrudes through the injection plate to provide the high voltage spark trigger for thruster ignition. It forms the spark with the cathode.

A.6 Measurement Devices

Various forms of instrumentation were used. Chamber pressure is measured with a Varian 843 vacuum ionization gauge. Pearson Electronics 301x Pulse transformers measure the current flowing through the thruster. Voltage across the thruster is measured by 1000:1 voltage probes attached to the PFN. A Tektronix DSA-601 digital signal analyzer and a Tektronix 11403 digitizing oscilloscope can be used to capture data from the instrumentation. Signal conditioning for the various measurement devices is aided by the use of Tektronix AM501 operational amplifiers.

A Klinger stepper motor assembly allows positioning of various measurement devices inside of the chamber. The arm is level with the thruster axis and can be translated and rotated. Each translational step is 2.54×10^{-5} m, and each step in rotational mode is .001 deg.

A.7 Method of Operation

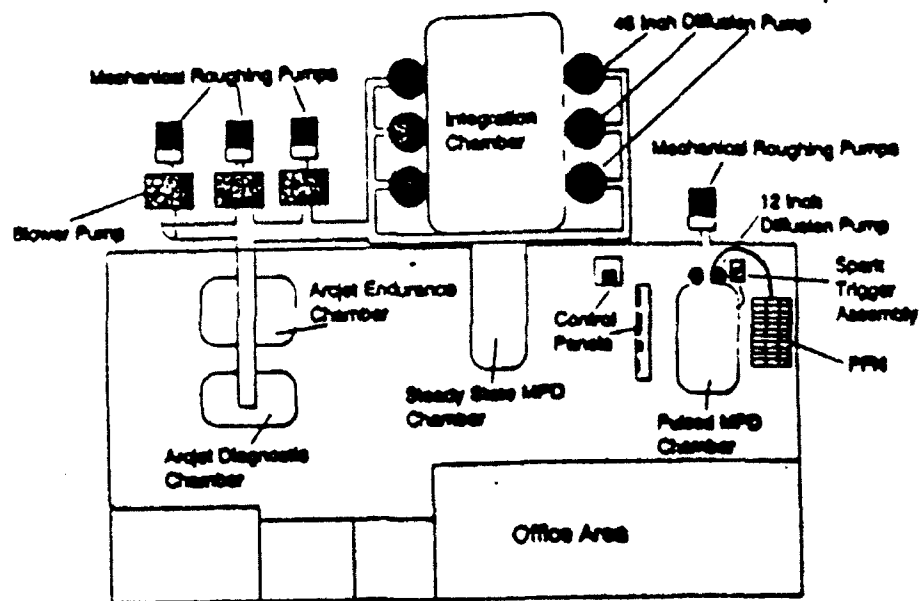
The firing procedure begins by charging the PFN through a connection with the power supply until a desired PFN voltage is reached, at which time the PFN is then disconnected from the power supply. The voltage present in the PFN is directly applied to the anode and cathode of the thruster. The operator also ensures that the pumps have brought the chamber pressure down to approximately 5×10^{-4} torr.

When the fire button is depressed, the timing boxes initiate their pulses. The gas pulse signal opens the solenoid valve, and twenty milliseconds later, the spark pulse is initiated. The resultant gas pulse has exponential growth and decay. With the additional lag time resulting from the mechanical relay between the high voltage power supply and thruster, the spark occurs when the gas pulse has reached steady state. This spark ionizes the plasma initially, allowing the higher currents from the PFN to flow between the anode and cathode.

Current measurements are taken using the Pearson coils. These are low frequency response devices; therefore, most noise

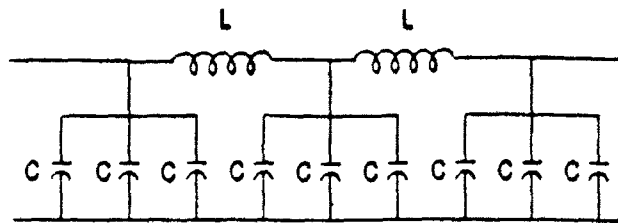
A-6

is filtered out of the current trace. However, the voltage probes have a high frequency response, and onset can be detected by looking at the voltage fluctuations in the steady state region of the voltage trace.

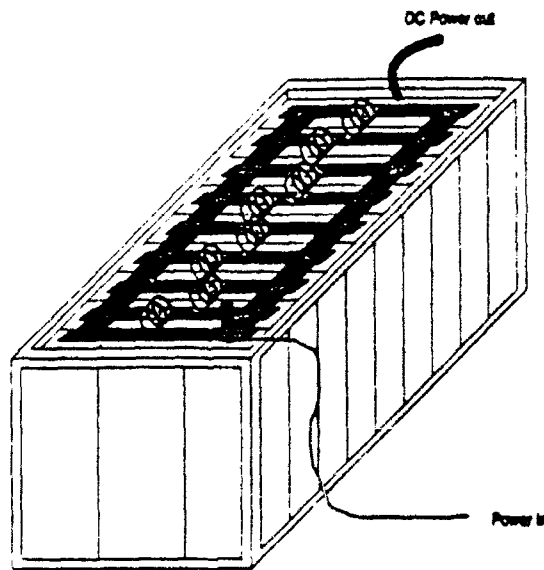


Facility Layout

Figure A.1 - Diagram of MPD Facility



Schematic-Pulse Forming Network



Pulse Forming Network

Figure A.2 - Schematic diagram of pulse forming network

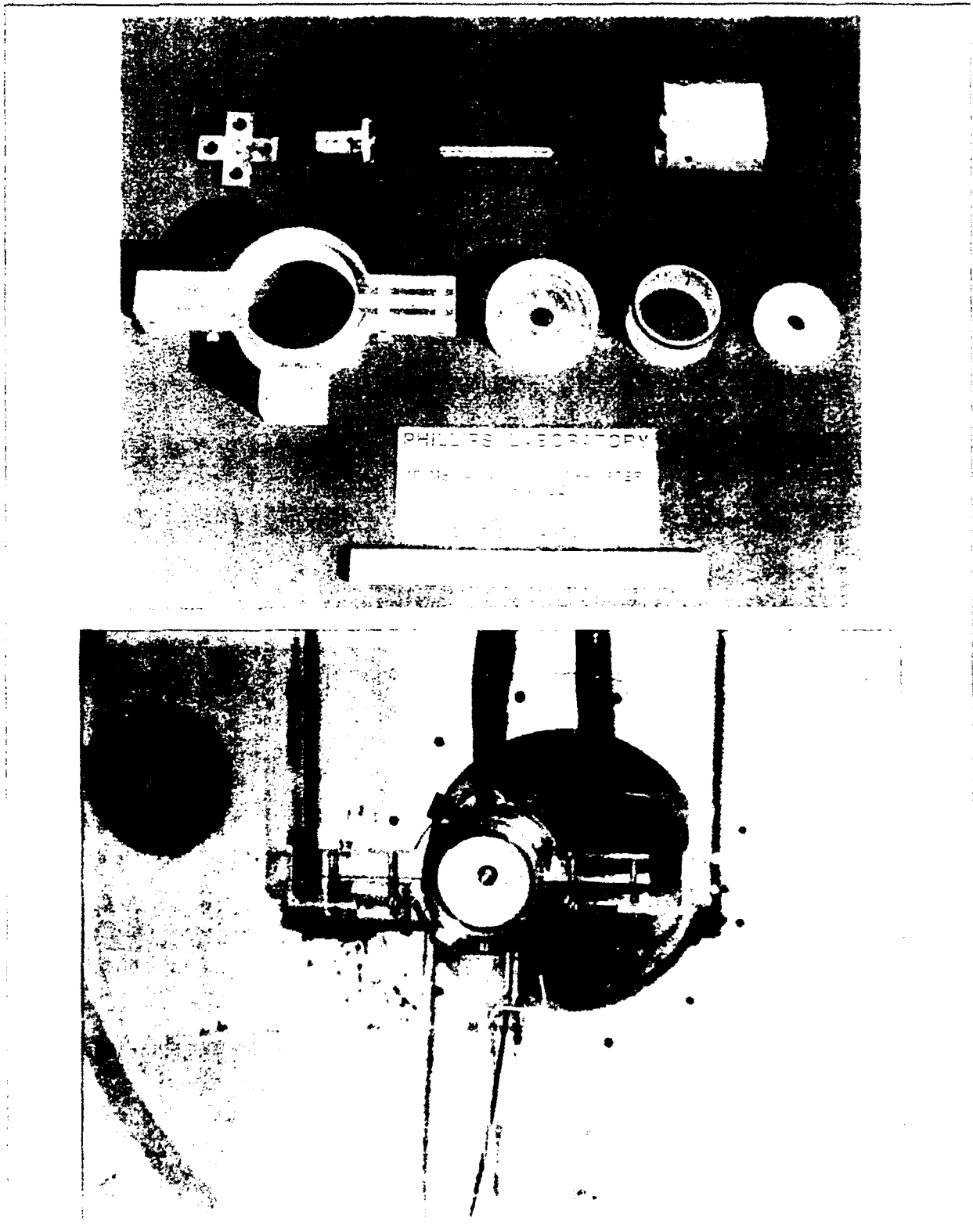


Figure A.3 - Self field MFD chamber

APPENDIX BMagnetic Probes

In order to calculate the lower hybrid frequency of the plasma, it is necessary to know the magnetic field at a particular point. To accomplish this, two different types of probes were used: a Hall probe and an induction probe.

B.1 Hall Probe**B.1.1 Theory**

The Hall generator works on the principle known as a Hall effect. Consider a flat plate conductor placed in a magnetic field with the normal to the surface of the conductor aligned with the magnetic field lines. If a current is simultaneously applied through the plate at opposite ends, a potential difference is created in the plate on the sides parallel to the direction of current flow.

The reason for this is fairly simple. The force generated by the current flowing through the magnetic field is

$$\mathbf{F} = \mathbf{I} \times \mathbf{B} \quad (\text{B.1})$$

where \mathbf{F} = magnetic force, \mathbf{I} = current vector, and \mathbf{B} = magnetic field vector. This force is applied to the charged particles in the conductor. However, since the ions do not move easily, the electrons are assumed to be the only particles that move. Since this force is applied perpendicular to the current path, the electrons are forced to move to one of the edges of the plate

which is parallel to the current; they cannot travel any further from the path than the edge of the plate. The predominance of electrons on one side and the absence of those electrons on the other creates a potential difference on those sides of the plate. However, the potential difference will make those electrons want to travel back to the other side of the plate. The only force preventing that is the magnetic force. At equilibrium conditions, the magnetic force will equal the electromotive force produced by the potential difference. Thus, the potential difference is directly proportional to the magnetic field in the perpendicular direction. This potential difference can be measured in many ways, but if it is measured by an oscilloscope, a trace of magnetic field vs. time can be acquired as well.

The Hall probe has been used successfully in steady state MPD plasmas at the kW level. Its primary advantage is that the B field strength may be calculated directly from the observed voltage. However, calibration is required in a known magnetic field in order to use it later in fields of unknown strength.

B.1.2 Experimental Use

In the experiments discussed in chapter III, a Bell BH-205 Hall generator was used. A factory calibration came with the probe (about .91 $\mu\text{V}/\text{Gauss}$ at 100 mA current), but a calibration performed in the laboratory using a Helmholtz Coil operated between 10 and 50 gauss showed a relationship of .87 $\mu\text{V}/\text{Gauss}$ at 100 mA. It should be noted that one disadvantage of the Hall

probe is that the probe sensitivity decreases with temperature. One reason for the discrepancy in calibrations is that isothermal operation of the probe was not possible in the laboratory; the current running through the probe heated it slightly above the temperature at which it was calibrated at the factory. This heating would decrease the sensitivity slightly, which is accounted for in the reduction of slope of the calibration relation.

The first attempts to measure the magnetic field strength in the azimuthal direction involved the use of a Hall probe. Another disadvantage of the Hall probe is its extremely low signal voltage, on the order of microvolts. Unfortunately, the electrical noise resulting from the start-up of the thruster was an order of magnitude higher than the signal which was observed during calibration of the Hall probe.

To ensure that the unexpected signal was due to extraneous noise rather than an actual magnetic field fluctuation, the probe was removed from its location in the near-plume of the thruster and placed approximately 1.5 m directly to the side of the thruster. At this location, the magnetic field should have been almost non-existent. The thruster was then fired and the signal was compared to the signal where the noise was first observed.

Almost the same signal resulted. The noise eventually disappeared, but the settling time of the noise was on the order of a millisecond, which happened to be the length of the steady state portion of the current pulse. Thus, only the ending

transient of the magnetic field signal was discernible, which was of no use in determining the magnetic field strength during the steady-state portion of the pulse.

In an attempt to eliminate this electrical noise, the probe was placed outside of the chamber and the thruster was fired. The large noise spike occurred, but it damped out well within the duration of the current pulse. The noise was at an acceptable level during the latter half of the steady-state region of the pulse. Because the chamber was, in essence, a large electrostatic shield, it was hoped that additional shielding of the electrical leads of the probe could reduce the noise to an acceptable level. This additional shielding took the form of a layer of aluminum foil connected to ground, wrapped around all of the coaxial cables. In addition, wires were twisted in an attempt to eliminate ground loops, which could also introduce spurious magnetic field signals. Although these actions reduced noise slightly, the effects were negligible; these actions still did not reduce noise to an acceptable level.

All of the leads were attached to a the interior wire of a coaxial cable. It might help to acquire triaxial cable and attach the leads to both the interior cable and the first coaxial layer of wire, with the third layer used as shielding. In addition, about 10 inches of the probe was unshielded except for a twisting of the voltage and current leads about themselves, but this problem could not be easily eliminated. A better probe design might try to account for the need for shielding of the

leads which are directly attached to the Hall generator.

It appears that this noise is not produced by the quasi-steady operation of the thruster, but instead is caused by the high voltage spark which breaks down the gas to allow current to flow in the quasi-steady pulse. If a less noisy means of start-up were devised, it is conceivable that the Hall probe could be used satisfactorily in a pulsed device even without the additional shielding. The premise that the spark ignition of the engine is what produces the electrical noise seems to explain why Hall probes have been used to measure magnetic fields satisfactorily in steady state MPD devices; the time at which magnetic fields are measured are typically long after the start-up. These transient effects of the spark trigger may also explain why this author has not seen any mention of Hall probes being used in pulsed MPD devices; induction-type magnetic probes are the only type mentioned. Since the Hall probe did not produce any usable results, an induction-type probe with an analog integrator circuit was constructed.

B.2 Induction Probe

B.2.1 Theory

An induction probe is very simple in its construction; it is merely a small cylindrical coil of wire. In fact, this coil is so small, it is assumed that the magnetic field strength does not vary over its cross section. As a result, the voltage induced by the introduction of a magnetic field through the probe can be

represented by [48]

$$V_i = -A_{eff} \frac{d}{dt} B_z(t) \quad (B.2)$$

where V_i \equiv induced voltage, A_{eff} \equiv effective cross sectional area of the coil, and B_z \equiv magnetic field perpendicular to the coil. In this relation, the voltage is proportional to the time derivative of B, rather than directly proportional to B. As a result, the signal must be passed through an integrator to get B as a function of voltage. It is not necessary to calculate the effective cross sectional area of the probe; if the probe is calibrated in a known magnetic field while the signal is passed through the integrator, a calibration curve for $B(V_i)$ can be produced. In fact, this method is preferred. Not only is it hard to get accurate measurements of the probe diameter for small cross-sectional areas, but the presence of the integrator may alter the signal slightly. As long as the signal is calibrated with the integrator in the circuit, anomalies due to the integrator's presence will be accounted for.

In general, induction probes can produce voltages much higher than the electrical noise level of the plasma [48], but the actual level of voltage is a function of the effective area of the coil and dB/dt . One way to increase the signal level is to increase the effective area of the coil cross section. This can be done in one of two ways. First, the coil size can be increased. Unfortunately, if this route is attempted, the spatial resolution will decrease. The second way is to increase

the number of turns of wire about the core. However, one effect of adding more turns of wire is to decrease the frequency response of the probe.

B.2.2 Experimental Use

The induction probe used in the measurements in chapter III was 1/16" long by 1/16" dia, with 75 turns of wire. This design produced a fairly high signal to noise ratio with a frequency response on the order of 100s of MHz. The frequency response of the probe was not very important, though, because only the mean field strength in the steady state region of the pulse was required. In addition, the integrator used an operational amplifier which had an effective cutoff frequency of 10 MHz. Thus, the circuit was limited in response by the operational amplifier, not the probe.

Unfortunately, this high frequency signal attenuation caused some error in integration. Since very high frequency fluctuations and spikes are attenuated, the integrated signal will neglect these fluctuations, and the level will be either lower or higher than what is actually seen. Although this has the benefit of eliminating noise, which theoretically would average out to zero over the integration, there may be some very fast rise times in the magnetic field strength in the initial portion of the current pulse which may be attenuated or eliminated entirely producing a small error in measurement.

Obviously, the stronger the magnetic field, the stronger the

signal. On the other hand, the time it takes for the B-field to reach that strength also comes into play. Based on this dependence, one can see that it is not really possible to apply an induction type-probe in a steady state device; theoretically, there is no change in magnetic field with time. However, it is ideal for a pulsed discharge. As the rise time of the current in the quasi-steady thruster used in chapter III is on the order of microseconds, dB/dt is fairly large at most locations in the thruster and plume. However, this dependence on dB/dt caused some problems in the probe calibration.

Initially, calibration was attempted in the Helmholtz coil as was done for Hall probe calibration. However, the power supply which powered the Helmholtz coil proved to be a limiting factor. First, the power supply could only operate up to 5 A, which limited the produced magnetic field to 50 Gauss based on the calibration for the Helmholtz coil. The magnitude of the known field posed no problem; plume measurements are within this range, and the signal was expected to be larger closer to the thruster. Unfortunately, the limiting factor was the time it took for the power supply to reach the desired current level: on the order of several milliseconds, depending on the current. As this is about 3 orders of magnitude slower than the rise time inside the thruster, which is what the probe was designed for, a signal was not discernible for calibration in the Helmholtz coil.

To overcome this problem, the probe was calibrated in the thruster itself. To do this, it was assumed that if the probe

was placed at the back plate of the thruster near the anode, all of the current going to the thruster would be enclosed by a circle corresponding to the radius of the probe location. Although this assumption is very reasonable, there is an error on the order of about 1% on the enclosed current. To find the magnetic field strength at the probe location, the following formula was used:

$$B_{\theta} = \frac{\mu_o I}{2\pi R} \quad (B.3)$$

where B_{θ} = magnetic field in azimuthal direction and R = the radial distance from the thruster axis. The magnetic field was varied by changing the input current to the thruster. The resultant calibration curve was 1.869 mV/Gauss, significantly larger than that for the Hall probe.

Although this method had some error involved in the "known" magnetic field, it also had some benefits that calibration in the Helmholtz coil did not. First and foremost, calibration of the probe through almost the entire range of magnetic field strengths was possible. The Helmholtz coil produced very accurate calibration data up to 50 Gauss, but much larger magnetic fields were expected. If the calibration curve was completely linear, the Helmholtz data would have been adequate, but if it wasn't, there would have been significant error in the range of high magnetic field strengths. By calibrating throughout the entire range of expected field strengths, this source of error was eliminated. The additional benefit is that the signal strength

B-10

in comparison to the noise level could be observed prior to actual magnetic field measurements.

APPENDIX CLangmuir Probes

The triple Langmuir probe is a measurement device which can be used to determine number density and electron temperature in the plasma. Before going into the configuration which was used in the experiments, it is important to discuss the theory of Langmuir probes in general.

C.1 Theory

The simplest form of a Langmuir probe is simply an exposed wire. In order to measure electron temperature and number density, the probe must be "floating". In other words, no net current is transferred between the probe and the plasma. Since current is the net movement of charge into the wire, in order to make the probe "float", the number of electrons and ions absorbed into the probe must equal the amount leaving the probe. At first glance, it would appear that this can be accomplished by setting the probe at a potential which is the same as the plasma. Although doing so does not produce a floating probe, it is useful to understand what would happen in such a case. With no potential difference, and consequently, no electric field present, electrostatic forces would not cause a predominance of one type of charged particle at the probe surface. Logically, the only particles which would impact on the probe surface would result from the random thermal motion of the plasma. Since the number of particles which would impact on the probe is a function

of the number of particles present locally in the probe's vicinity, and also a function of their temperature, the measured current and potential can indicate the local number density and electron temperature.

Unfortunately, there is a complication. Since electrons are so much lighter than ions, for a given temperature in an isothermal plasma, more electrons than ions will impact the probe surface. This is why merely setting the probe at the plasma potential will not result in a floating probe. In order to make it float, the probe must be biased at a negative potential with respect to the plasma; this negative potential will repel enough electrons through electrostatic forces to allow an equal number of electrons and ions to impinge on the probe surface.

However, the presence of a sheath leads to further complications of the situation. One of the properties of a plasma is to maintain macroscopic charge neutrality, and the formation of sheaths about potential sources is the mechanism the plasma uses to accomplish this end. The sheath is not a problem; particles move freely outside the sheath region, but the electric fields present inside the sheath prevent too many electrons from hitting the surface. This results in the plasma remaining largely undisturbed by the presence of the probe, while still allowing the probe to measure number density and electron temperature. The problems arise because the measured current, specifically the number of ions hitting the probe, depends on the size of the sheath relative to the size of the probe. Different

theories must be used to relate current to electron temperature and number density depending on the relative sizes of the mean-free path, sheath thickness, and probe size.

In the MW level MPD thruster, the number densities and electron temperatures have been shown to produce mean free paths on the order of a mm, and debye lengths around a μm . Since it is very difficult to get a wire which is on the order of a debye length which will retain any durability, the probe theory which is used is based upon the assumption of a thin, collisionless sheath. In thin sheath theory, the assumption can be made that the ion current is independent of sheath potential.

For the triple probe, all of the probes are biased with a negative potential relative to the plasma. Figure C.1 shows the configuration of the triple probe the key potential differences. Electrode 2 is floating, while there is a current path flowing into electrode 1 and out of electrode 3. No net charge is lost from the plasma because the charge that is lost by electrode 1 is regained at electrode 3. Using Kirchoff's Law, equations can be written for the three electrodes.

$$\text{ELECTRODE 1: } \frac{I_{probe}}{A_1} = J_{eo} \exp(-\chi_1) - J_i(\chi_1) \quad (C.1)$$

$$\text{ELECTRODE 2: } 0 = J_{eo} \exp(-\chi_2) - J_i(\chi_2) \quad (C.2)$$

$$\text{ELECTRODE 3: } \frac{I_{probe}}{A_3} = -J_{eo} \exp(-\chi_3) + J_i(\chi_3) \quad (C.3)$$

where

$$\chi_j = \frac{e|V_j - V_p|}{kT_e}$$

$$J_{eo} = \text{electron current at sheath edge} = n_e e \sqrt{\frac{kT_e}{2\pi m_e}}$$

$$J_i = \text{ion flux at electrode surface} = \exp(-0.5) en_e \sqrt{\frac{kT_e}{M_i}}$$

For these equations, V_j is the potential of electrode j , V_p = plasma potential, χ_j = dimensionless potential of electrode j , and J_i is based on Bohm's sheath criteria.

Using this system of equations, T_e and n_e can be solved for if the following assumptions are made:

- 1) J_i is independent of χ_j in the thin sheath limit.
- 2) $A_1 = A_3$
- 3) V_{d3} is set by the experimenter.

Solving this system of equations yields the following relations between n_e , T_e , V_{d3} , I , and A_1 :

$$2 \cdot \exp\left(\frac{eV_{d2}}{KT_e}\right) - 1 = \exp\left(\frac{eV_{d3}}{KT_e}\right) \quad (C.4)$$

$$n_e = \frac{\frac{I_{probe}}{A_1} \cdot \exp(0.5)}{e \sqrt{\frac{KT_e}{M_i}} \cdot (1 - \exp(\chi_{d2} - \chi_{d3}))} \quad (C.5)$$

Equation (C.4) must be solved implicitly to find T_e .

C.2 Experimental Use

The probe used in the experiments in chapter III consisted of three 0.125 mm dia tungsten wires aligned parallel to each other having an exposed length of 4 mm. The ends of the wires were aligned in axial position as well. Insulation of the wires was provided by alumina tubes of 0.25 mm inner dia and 1 mm outer diameter. EPOTEK high temperature epoxy was used to attach the wires to the alumina tubes, fixing the area of exposed wire at $A_1 = 0.5\pi \text{ mm}^2$. The alumina tubes were attached to a 4 hole alumina holder with 1.5 mm dia holes and 6 mm outer diameter by Ceramabond 671 ceramic paste. In addition, the tungsten wires were attached to coaxial cables at the base of the alumina holder to provide electrostatic shielding, and to allow the use of BNC connectors for the vacuum feedthrough. The probe itself was housed in a plexiglass holder attached to a translational X-Y table, where the tip of the probe was approximately 19-20 cm from the probe holder. The inter electrode spacing was 3 mm between 1 and 2, 1.5 mm between 2 and 3, and 2.5 mm between 1 and 3 in a

triangular configuration.

The probe was designed to meet the following criteria.

$$\frac{r_p}{\lambda_i} > 1 \quad (\text{C.6})$$

$$\frac{\lambda_{ii}}{r_p} > 1 \quad (\text{C.7})$$

$$\tau = \frac{L_p}{r_p} \sqrt{\frac{Z_i K T_e}{M_i}} \frac{1}{U_{ii}} > 1 \quad (\text{C.8})$$

$$\frac{S}{\lambda_d} > 1 \quad (\text{C.9})$$

$$\frac{r_{Le}}{r_p} > 1 \quad (\text{C.10})$$

$$\frac{eV_{d3}}{K T_e} > 1 \quad (\text{C.11})$$

where r_p = radius of the probe, λ_{ii} = ion-ion mean free path, τ = end effect parameter, Z_i = charge of the ion, L_p = length of the probe, and S = inter-electrode spacing. Each if these equations allow one or more assumptions to be made if they are satisfied. (C.6) is the condition which is necessary to use thin sheath theory, (C.7) assures that the sheath is collisionless, (C.8) allows end effects to be ignored, (C.9) assures that the sheaths surrounding the electrodes do not significantly interfere with each other, (C.10) makes sure that the presence of a magnetic field does not significantly hinder the movement of electrons to

the probe, and (C.11) insures that a finite electron temperature can be calculated from V_{ij} , and that the electron flux is negligible compared to the ion flux. The probe described above was designed to meet these conditions based on expected conditions in the thruster plume.

It must be noted that the underlying assumption which allows the use of thin sheath theory is that the ion flux is independent of χ_2 . However, the functional dependence of J_i depends on several factors. The conditions in (C.6-11) allow some of these functional dependencies to be assumed negligible, but χ_2 can still come into play. The ratio of ion velocity which is perpendicular to the probe axis over the most probable ion thermal velocity also plays a role. In addition, electron retarding current can be significantly affected by magnetic fields, electron drift, and electron-ion collisions [35]. However, in the experimental work, V_{ij} was set rather high so that the electron flux at electrode 3 is negligible compared to the ion flux. This allows the formation of an explicit relation for V_{i2} .

$$\frac{eV_{d2}}{KT_e} = \ln\left(\frac{I_{i1} + I_{i3}}{I_{i2}}\right) + \ln\left(\frac{A_2}{A_1}\right) + \ln\left(\frac{o_e(\chi_2)}{o_e(\chi_1)}\right) + \frac{e\Delta V_{cont.}}{KT_e} \quad (C.12)$$

where I_{ij} \equiv ion current to electrode j , A_j \equiv collection area of electrode j , and $\Delta V_{cont.}$ \equiv contact potential difference. The first term reduces to $\ln 2$ in the thin sheath limit, the second term takes into account the effect of unequal probe areas, the third takes into account deviation of the electron flux from

$A_j J_{e0} \exp(-\chi_j)$, and the last term takes into account the contact potential difference when the probe is contaminated. To use the simplified theory, the assumption is made that the last 2 terms are negligible for a clean probe, and the probe was designed so that electrodes have equal areas. This means the second term is negligible as well. Thus, the simple relation $eV_{d2}/KT_e = \ln 2$, from which electron temperature can be directly calculated, is all that remains.

C.3 Laframboise's Exact Theory

For locations where $\chi_j > 3$ and r_p/λ_c is between 5 and 100, Laframboise's theory accompanied by the Peterson-Talbot curve fits [36] may be used. This theory does take into account sheath potential and the results are considered exact. The curve fits are:

$$J_i(\chi_j) = [B_p + \chi_j]^\alpha \quad (C.13)$$

where

$$\alpha = \frac{2.9}{\ln\left(\frac{r_p}{\lambda_d}\right) + 2.3} + 0.07 \left(\frac{T_i}{Z_i T_e} \right)^{0.75} - 0.34$$

$$B_p = 1.5 + \left(0.85 + 0.135 \left[\ln\left(\frac{r_p}{\lambda_d}\right) \right]^3 \right) \left(\frac{T_i}{Z_i T_e} \right)$$

This theory also makes the assumption that only one ionized species exists and end effects and sheath interactions are negligible. To make this probe theory work, the following equations must be solved simultaneously.

Implicit Relation for electron temperature :

$$\frac{1}{2} = \frac{1 - \frac{1}{2} \left([1 - \beta_p V_{d2}]^{\frac{1}{2}} + [1 + \beta_p (V_{d2} - V_{d1})]^{\frac{1}{2}} \right) \exp(-\chi_{d2})}{1 - \exp(-\chi_{d1})} \quad (C.14)$$

where

$$\beta_p = \frac{e \eta_{probe}}{k T_e} \quad (C.15)$$

$$\eta_{probe} = \left(\frac{dJ_i^z(\chi_j)}{d\chi_j} \right) \frac{1}{J_i^z(\chi_f)}$$

and χ_i = dimensionless floating potential.

From the Peterson-Talbot curve-fit:

$$\eta_{probe} = \frac{2\alpha}{B_p + \chi_f} \quad (C.16)$$

The condition based on equal electron and ion currents for a floating probe:

$$[B_p + \chi_f]^{2\alpha} - \frac{M_i}{m_e} \exp(-2\chi_f) = 0 \quad (C.17)$$

The number density:

$$n_e = \frac{1}{e} \sqrt{\frac{2\pi M_i}{k T_e}} \frac{\frac{I_{probe}}{A_j}}{([B_p + (\chi_{d1} - \chi_{d2}) + \chi_f]^\alpha - [B_p + \chi_f] \exp[\chi_{d2} - \chi_{d1}])} \quad (C.18)$$

When these equations are solved numerically, the last check is to make sure that r_p / λ_e is consistent. This must be updated to a new value based on the n_e and T_e calculated above, and the calculations must be repeated until convergence occurs.

The last point which must be made is that the exact theory assumes that the probe is aligned with the flow. A non-alignment of the probe with the flow can lead to an error on the order of 2 in both T_e and n_e . However, this situation will also result no matter which theory is used, because sheath theory has not progressed far enough to account for the effects of an asymmetric sheath. In general, Laframboise's theory may be considered exact between r_p/λ_c of 5 and 100, but it is still valid for values above 100, although there is a small error involved. Another method may be used above this area as well, but it is felt that the error in using Laframboise's theory is well within the experimental error for the Triple probe in the MPD temperature and density regime. It should be noted that for $\chi_3 < 3$, numerical solutions for the above equations do not converge self-consistently with r_p/λ_c . Thus at these locations, which corresponded to locations inside the thruster for the experiments performed in chapter III, simple thin sheath theory is used, although the error is more significant. This sacrifice of accuracy is necessary in order to get any values in this region. In addition, thin sheath theory is valid to much lower potentials because it assumes ion flux is independent of potential. Laframboise's theory could be used in this region of the thruster if V_{d3} were increased to a much higher value, but this was not done in the experiments discussed in this paper.

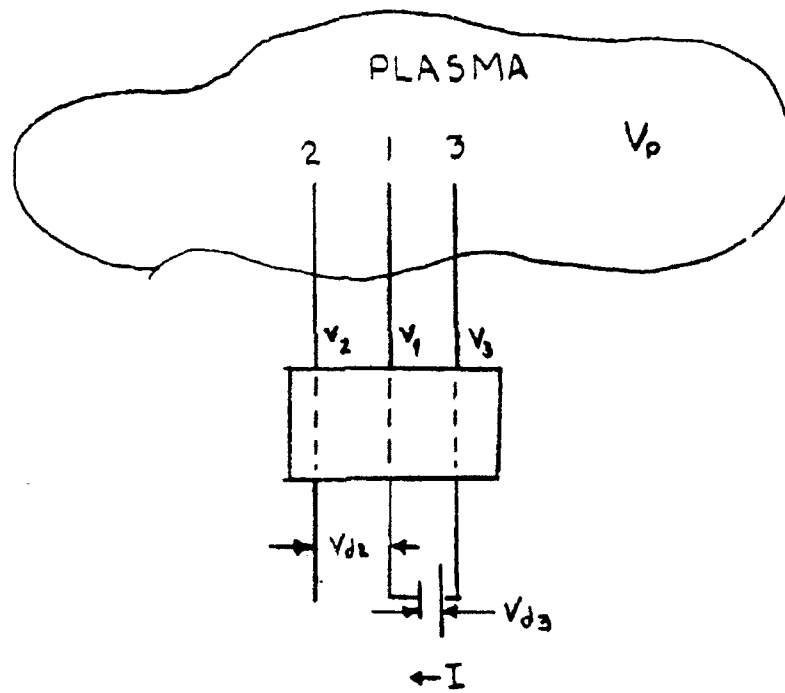


Figure C.1 - Schematic diagram of Langmuir probe electrodes and potentials

APPENDIX D

Documentation of Computer Code

D.1 Introduction

This program package for calculation of thermophysical and transport properties of a two-temperature plasma was written by Dr.-Ing. Tarit Kumar Bose, Professor of Aeronautical Engineering, Indian Institute of Technology, Madras, India with the help of his students in 1987. The present modification of this code to account for microinstabilities was accomplished by Erik C. Bowman, a graduate student of Dr. S.N.B. Murthy in the School of Aeronautical and Astronautical Engineering at Purdue University in West Lafayette, Indiana.

One of the earlier versions of the program was written in connection with the doctoral work of R.V. Seeniraj, and the files are designated with the words SEEN or SEENIRAJ. The Seeniraj files are for noble gases only, but simpler forms of the mixture properties are used; for atom-ion collision, however, the charge-transfer collision data are used, and for atom-atom collisions the exponential repulsive potential data (Monchik tables), which are available for noble gases, are used. Later programs may be used for the calculations for more general dissociated and ionized gas mixtures, and they use Lennard-Jones 6-12 potential for both atom-atom and atom-ion collisions. They also use more complex transport property mixing rules. Because of using complex property mixing rules, which require the solution of the ratio of two large valued determinants to get a small value of the ratio, they are known to give erratic results under certain circumstances. For example, for a high degree of ionization, the heat conductivity coefficient for heavy particles gives a very small negative value. Similarly the electrical conductivity may become negative for a small degrees of ionization. These later programs also allow calculation of thermophysical and transport properties for almost thirty different primary components, by appropriately combining the data for these different components in the data file PLASMA2.DAT.

Therefore, the user has a choice. If calculation of the properties of noble gases as accurately as possible at all possible temperatures and pressures is desired, use the SEENIRAJ programs. The later programs can also be used for the calculation of the properties of noble gases. However, for any other gas plasma, only the later programs are to be used.

All of the programs in this package have been compiled, linked and run with the help of Microsoft software (Microsoft FORTRAN 77 version V3.13 dated Aug. 5, 1983 + Objectlinker version V2.01) and IBM software (IBM Professional Fortran version 1.21 and corresponding linker). The Microsoft FORTRAN compiler has the limitation of block space for both instructions and data, and may require splitting of the file PLASMA1.FOR.

Alternatively, you may compile everything with the help of IBM software with ./B option. The 1992 modification used Microsoft FORTRAN version 5.1; PLASMA1.FOR did NOT have to be split if this compiler is used. A memory model designated LARGE is recommended if this compiler is used, however. Compilation was also attempted on Lahey Personal FORTRAN version 2.0. Although it could be compiled, it could not be linked due to a 64K limit on the sum of all object segments to be linked. After contacting Lahey, it appears that even later versions of the compiler may have this limitation, and it is recommended that Microsoft or IBM compilers should be used, unless the user has information on how to get around the limit on block size. For the purpose of compatibility with both of the above software, initially an asterisk refers to the console terminal with keyboard, but after calling the program OUTPUT by the main program, the console terminal with the keyboard is referred to as unit 4 and the output file (con = console; prn = printer; and any other disk output file) is referred to as unit 6. While running the programs, the input data files PLASMA1.DAT and PLASMA2.DAT must remain in the default disk or hard drive directory.

There are a number of test programs (main programs) being supplied in this program package, which can be compiled, linked and executed to familiarize the user with the programs. In actual practice the main program in the particular combination has to be replaced by a user supplied main program.

For any questions about the methodology, the following references may be consulted:

1. D. Kannappan and T.K. Bose, Transport properties of two-temperature argon plasma, Physics of Fluids, Vol. 20, No. 10, Part 1, Oct. 1977, pp. 1668-73.
2. D. Kannappan and T.K. Bose, Transport properties of two-temperature helium plasma, Physics of Fluids, Vol. 23, No. 7, July 1980, pp. 1473-74.
3. T.K. Bose and R.V. Seeniraj, On reactive conductivity coefficient of multiple ionized two-temperature argon plasma, Waerme- und Stoffuebertragung, 1985, pp. 3-8.
4. T.K. Bose, Thermodynamic analysis of a seeded magnetogasdynamic combustion plasma, AIAA/ASME 4th Joint Thermophysics and Heat Transfer Conf., Boston/Mass., 1986, AIAA-86-1333.
5. T.K. Bose, Thermophysical and transport properties of multiple component gas plasma at multiple temperatures, Progress in Aerospace Sciences, 1987 (in press).

D.2 List of Files and Subroutines

D.2.1 Data files:

(to be stored in default disk during execution):

PLASMA1.DAT : file containing collision cross-section data.

PLASMA2.DAT : file containing individual gas data:

1. Ionization energy, statistical weight and excitation energy (referred to as Part I)
2. gas-kinetic cross-section for electron-atom collision (referred to as Part II)
3. enthalpy-entropy data (in kJ/kmole for temperature upto 15000K). (referred to as Part III)

D.2.2 Subroutine files:

PLASMA1.FOR : principal subroutines to calculate two-temperature plasma properties.

PLASMA2.FOR : auxiliary subroutines to organize calculation of properties containing atoms and/or molecules.

AIPLASMA.FOR: auxiliary subroutine to organize calculation of properties of air up to 15000K.

SEENIRAJ.FOR: auxiliary subroutines to organize calculation of properties of noble gases by previous method.

SEENMICR.FOR: auxiliary subroutines to organize calculation of properties of noble gases by previous method while accounting for the effects of anomalous electrical conductivity resulting from the presence of lower hybrid microinstabilities.

D.2.3 Demonstration main routine files:

SEENTEST.FOR: to calculate properties of noble gases by earlier method (link: SEENTEST+SEENIRAJ+PLASMA1).

NOBLE.FOR : to calculate properties of noble gases by later method (link: NOBLE+PLASMA1+PLASMA2).

AIRTEST.FOR : to calculate properties of air plasma(up to 15000K) (link: AIRTEST+AIPLASMA+PLASMA1).

ATOMTEST.FOR: to calculate properties of atomic and ionic air plasma (beyond 15000K to 50000K)(link: ATOMTEST+PLASMA1+PLASMA2).

MGDTEST.FOR : to calculate properties of seeded combustion plasma (upto 6000K)(link: MGDTEST+PLASMA1+PLASMA2).

MICRTEST : to calculate electrical conductivity both classically and including anomalous transport due to lower hybrid microinstabilities. The other transport properties are only calculated classically by the SEENIRAJ method.

While the above demonstration programs are all interactive in nature, and the results are either displayed on the CRT terminal or printed on the printer, some additional information follows which may be quite useful:

AIRTEST.FOR: This is to determine air plasma composition for a single temperature plasma. Calculation is done in three ranges up to 15000K.

Range I: N₂, O₂, N, O, NO

Range II: N₂, O⁺, e⁻, N, O, O₂, NO, N⁺

Range III: N⁺, O⁺, e⁻, N, O

ATOMTEST.FOR: This is for a multi-temperature air plasma in the temperature range beyond that in AIRTEST. The species being considered are:

e⁻, N⁺, O⁺, N, O, N⁺⁺, O⁺⁺

With increasing temperature, ionization level is automatically changed and the correspondingly higher ionized nitrogen and oxygen ions are obtained.

MGDTEST.FOR : This is for calculation of the plasma for combustion of different fuel gas (Water gas, Lurgi, Koppers-Totzek, Producer gas and methane) with oxygen enriched air and alkali metal seed (either pure metal or specific salt). The following gas components are considered:

CO₂, O₂, N₂, H₂, K⁺, e⁻, CO, O, N, NO, H, H₂O and CH₄

NOBLE.FOR : For the calculation of multi-temperature noble gas plasmas (He, Ne, Ar, Xe, Kr) at different temperatures and pressures, but reactive heat conduction is not considered.

SEENTEST.FOR For calculation of multi-temperature noble gas plasma (He, Ne, Ar, Xe, Kr) at different temperatures and pressures, including reactive heat conduction.

D.3 Content of each file

PLASMA1.DAT : non-dimensional collision cross-section tables for various potentials (Lennard-Jones 6-12 potential, Monchik tables for exponential repulsive

potential, and repulsive and attractive Coulomb potential).

PLASMA2.DAT : data (Table 1) for various gases (Table 2).

PLASMA1.FOR : contains the subroutines as follows:

RDITAB : to read data from PLASMA1.DAT

RDECCS : to read data from PLASMA2.DAT

ELAT : to calculate electron-atom collision cross-sections.

LENJON : to calculate collision cross-sections for Lennard-Jones 6-12 potential

MONCH : to calculate collision cross-sections for exponential repulsive potential (Monchik tables)

CRGCRS : to calculate collision cross-sections for attractive or repulsive Coulomb potential

IONAT : to calculate charge-transfer cross-section
 for atom-ion collisions
 EQUCOM : to evaluate equilibrium mole fraction
 XEGRDT : to evaluate the partial derivative with
 respect to T_e and T_h (electron/heavy
 temperatures)(used for single species
 plasma only)
 DETERM : to evaluate determinants
 AILGTB : to interpolate in tables by Aitken-Neville
 or Lagrange method (WARNING: an error in
 interpolation was observed when using this
 subroutine in 1992. Unfortunately, not
 enough was known about this interpolation
 method to correct it. It appears that the
 right magnitudes are given, but the sign
 is SOMETIMES wrong)
 SOLEQ : to solve simultaneous linear equations
 OUTPUT : to define output files
 BROKAW : to calculate mixture transport properties
 and internal heat conductivity coefficient
 for molecules by the Brokaw formulas
 TTGPTP : general organization routine to calculate
 transport properties of the plasma
 PLASMA2.FOR : ATOMPL : general organization routine to calculate
 thermophysical and transport properties
 for gas plasmas with multi-species atomic
 components (change of ionization level for
 individual components; reactive heat
 conductivity coefficient included, but
 radiation not included)
 MOLGAS : general organization routine to calculate
 thermophysical and transport properties
 for gas plasmas in which there is at least
 one molecular component (change of ioniza-
 tion level not allowed; reactive heat
 conductivity coefficient included, but
 radiation not included). (valid upto 15,
 000K)
 AIPLASMA.FOR: AIRPR1 : initialization subroutine for air plasma
 AIRPR2 : air properties calculation subroutine
 (valid upto 15000K)
 APRHLP : auxiliary subroutine to APRHLP
 SEENIRAJ.FOR:RDSEEN : to read from PLASMA1.DAT and values for a
 single noble gas from the file PLASMA2.DAT
 for use in Seeniraj routines
 ELATOM : to calculate electron-atom collision cross
 section
 INSPPR : to calculate for individual gas components
 the transport properties
 ECMTTP: equilibrium composition for noble gas
 plasmas
 FCMTTP : frozen composition mixture

enthalpy-entropy for noble gas plasma
 TPSSIP : organization subroutine for calculation of
 transport properties of a noble gas plasma
 MGDTEST.FOR SEEDCP : organization subroutine for selected
 seeded combustion plasma

D.4 Running Demonstration Routines

D.4.1 Explanation of Inputs:

For noble gas plasma calculations (SEENTEST, MICRTEST, or NOBLE), a guess of the electron mole fraction for electrons, x_e , is required. This may be done by starting from a sufficiently high temperature to one, where error is found. As an example, at 1 bar and electron temperature = heavy particle temperature, the following guess values of x_e for different noble gases are given:

He: $7.587e-7$ at 8000K; Ne: $8.631e-8$ at 6000K; Ar: $8.713e-7$ at 5000K; Xe: $4.560e-8$ at 4000K; and Kr: $2.569e-4$ at 4000K.

SEENTEST calculates the transport properties over a range of electron temperatures, pressures, and temperature ratios. The inputs require the following units, and/or ranges:

Number of Temperatures: (No. of Temp)	This is the number of temperatures at which the calculation of transport properties are desired. The number can range between 1 to 32767, but they increase linearly according to the temperature difference entered.
Initial Temperature: (Temp1)	This is the first temperature at which calculation of transport properties are desired. The units are in Kelvin.
Temperature Difference: (Temp. Diff.)	This is the temperature increment between the temperatures transport properties are calculated at. The units are in Kelvin.
Number of Temperature Ratios: (No. of Temp. Rat.)	This is the total number of temperature ratios at which transport properties are desired. However, there is no input for a starting temperature ratio. It assumes the initial value is one and will increase from there by 1 each time.
Number of Pressures : (No. of Press.)	This is the total number of pressures at which calculations are desired. This number can range from 1 to 32767.
Initial Pressure : (Press1)	This is the first pressure at which transport properties are desired. The units are in bar (1 bar = 10^5 Pa)

Pressure Factor (P-Factor) : The program increases pressure logarithmically rather than linearly, so P-factor represents the factor the previous pressure is multiplied by to get the next value of pressure at which calculations are to be performed.

MICRTEST has all of the values assigned internally. If the user would like to change them, the following variable names are associated with the above properties. The same variable names are used in SEENTEST.

DTE:	Temperature Difference
NPRES:	Number of Pressures
NTEMP:	Number of Temperatures
NTR:	Number of Temperature Ratios
PIBAR:	Initial Pressure
PFAC:	Pressure Factor
TEMIN:	Initial Temperature
XEl:	Initial guess of mole fraction

For running the program AIRTEST limiting values of N2LIM and O2LIM are 1.e-5.

D.4.2 Flowcharts:

The following are the flow charts of the demonstration routines:

[illegible]

```

ATOMTEST <----> OUTPUT
                  ATOMPL <----> RDITAB <----> PLASMA1.DAT
                                RDECCS <----> PLASMA2.DAT
                                PARTI
                                SOLEQ
                                TTGPTP <----> LENJON
                                                CRGCRS
                                                ELAT
                                                DETERM
                                                BROKAW

```

```
MGDTEST    <----> OUTPUT  
              MOLGAS <----> RDITAB <--- PLASMA1.DAT  
                                RDECCS <--- PLASMA2.DAT  
                                PARTI  
                                SOLEO
```

D-8

```

                                TTGPTP <----> LENJON
                                CRGCRS
                                ELAT
                                DETERM
                                BROKAW

MICRTEST <----> RDSEEN <----> RDITAB <----> PLASMA1.DAT+PLASMA2.DAT
                                OUTPUT
                                ECMTTP
                                TPSSIP <----> LENJON
                                                MONCH
                                                IONAT
                                                CRGCRS
                                                ELATOM
                                                DETERM

NOBLE      <----> OUTPUT
                                ATOMPL <----> RDITAB <----> PLASMA1.DAT
                                                RDECCS <----> PLASMA2.DAT
                                                PARTI
                                                SOLEQ
                                                TTGPTP <----> LENJON
                                                                CRGCRS
                                                                ELAT
                                                                DETERM
                                                                BROKAW

SEENTEST <----> RDSEEN <----> RDITAB <----> PLASMA1.DAT+PLASMA2.DAT
                                OUTPUT
                                ECMTTP
                                TPSSIP <----> LENJON
                                                MONCH
                                                IONAT
                                                CRGCRS
                                                ELATOM
                                                DETERM
```

D.5 Description of records (lines of data) in data files :

Table 1: Description of records in PLASMA2.DAT. For a qualitative description of what types of information are in Parts I, II, and III, see section D.2.1 on data files . A more complete description of what variables these values are assigned to is given in the explanations of variables in subroutine RDSEEN in section D.6.

Record 1: NCODE, NCARD, NCARDE, NENER, IDIM, NCARDC, NELATL,
 NCARDE, NENP
 where

NCODE : code number of gas

NCARD : number of records (lines of data) for each gas
 : NCARDE+NCARDC+NCARDP+2

NCARDE: number of records in Part I for each gas
 NENER : number of ionization levels
 IDIM : energy dimension code (IDIM = 1, in J; =2, in cm**(-1); =3, in °K; =4, in eV)
 NCARDC: number of records in Part II for each gas
 NELATL: number of electron-atom gas-kinetic energy levels
 NCARDP: number of records in Part III for each gas
 NENP : number of enthalpy (MJ/kmole) and entropy (MJ/kmole-K) values for temperatures upto 15,000K in 3 ranges (15,000 to 6,000K: temp. interval = 500K; 6,000 to 3000K: temp. interval = 200K; 3,000 to 400K: temp. interval = 100K; 298.15K; and 0K)

Record 2: Text

Record NCARDE (Part I for each gas):

total number of ioniz.level; no. of gi,Ei in each level
 ionization potential
 (gi,Ei) values in each level

Record NCARDC (Part II for each gas):

number of electron-atom gas-kinetic energy ranges
 initial energy in the range; energy step size
 electron-atom gas-kinetic collision cross-section

Record NCARDP (Part III for each gas):

NENP enthalpy values
 NENP entropy values

Table 2: List of gases for which data is in PLASMA2.DAT

Code No.	Gas	Part	Code No.	Gas	Part
1	He	I, II	16	Cl2	II
2	Ne	I, II	17	NO	II, III
3	Ar	I-III	18	N2O	II
4	Kr	I, II	19	NH3	II, III
5	Xe	I, II	20	H2O	II, III
6	Li	I, II	21	CO	II, III
7	Na	I, II	22	HCl	II
8	K	I, II	23	CH4	II, III
9	Cs	I, II	24	CO2	II, III
10	H	I-III	25	OH	III
11	N	I-III	26	Ar+	III
12	O	I-III	27	H+	III
13	H2	II, III	28	N+	III
14	O2	II, III	29	O+	III
15	N2	II, III	30	e-	III

D.6 Description of Subroutines:

AILGTB

Call for the subroutine is:

```
CALL AILGTB(XT,YT,NT,NZ,X,Y,N,IFL,IAL)
```

where

XT(NT) : Table of x-values. INPUT

YT(NT,NZ) : Two-dimensional array of y-values. INPUT

NT: number of rows in the table of Y values and number of x values

NZ : number of columns in the table of Y values. INPUT

X : Value of x at which interpol. values are required. INPUT

Y(NZ) : interpolated y-values. OUTPUT

N : order of interpolation. INPUT

IFL: out of range extrapolation done/error. (IFL = 0, no extrapolation; = -1, extrapolation at near end; = -2, extrapolation at far end; = 2, monotonicity not present: error). OUTPUT

IAL: index for interpolation by Aitken-Neville/Lagrange method (IAL = 0, A.N. method; .NE. 0, Lagrange

method). OUTPUT

Internal Variables:

A: This variable has several different assignments:

- 1) The difference between the first and last values of

x
 2) The product of all delta x's of adjacent points in the immediate vicinity of the desired x
 3) The difference between adjacent delta x's
 B: Product of all possible differences between delta x's of adjacent points
 JA: the number of points - half of the order of interpolation
 JB: the number of points + half of the order of interpolation
 K: Loop variable representing a column of Y data
 N1: Half of the order of interpolation
 Sign: Indicator as to whether x-values are increasing or decreasing(+1 = increasing, -1 = decreasing)
 WA(N-1): difference between the current x-value and the previous one examined
 WB(N-1,NZ): Y value at each point surrounding the interpolation point.
 WC(N1): I don't know. Ask Dr. Bose.
 WD(N): Ratio of product of delta x's over product of all possible differences between delta x's
 YA: difference between last and second to last points
 YB: difference between second to last and third to last points
 YC: difference between last and third to last points
 YD(NZ): First derivative (Slope) used in far-side extrapolation
 YDD(NZ): Second derivative(numerical) used in extrapolation

AIRPR1

Call for the subroutine is:

CALL AIRPR1(NP,NPG,TT,CPRT,XPG)

where

NP : printing index (=0, print data input values; .NE. 0, do not print). INPUT
 NPG(8,4) : contains in each row: charge (for molecules, value put is -2), index for Part I-III data in Plasma2.DAT to be stored. INPUT
 TT : temperature table. OUTPUT
 CPRT : specific heat (MJ/kmole-K) table. OUTPUT
 XPG(8,8) : contains in each row: mole mass, Lennard-Jones potentia parameter, molecular dia (in Ang.). 3 cols.
 INPUT. On OUTPUT in each row (cols. 4-8) it contains:
 mole fraction, molar spec. heat (MJ/kmole-K), molar enthalpy (MJ/kmole), mean free path (m), and species diffusion coeff. (before mix. rule is applied)(m²/s).

AIRPR2

Call for the subroutine is:

```
CALL AIRPR2(NPG,TT,CPRT,XPG,T,PBAR,IRANGE)
```

where

NPG,TT,CPRT,XPG : see AIRPR1
 T : temperature (deg.K). INPUT
 PBAR : pressure in bar. INPUT
 IRANGE : an index to indicate extrapolation in the interpolation subroutine. INPUT

APRHLP

Call for the subroutine is:

```
CALL APRHLP(NTOT,NPRIM,XNMX,HMX,SV,CPRV,X,XPG,NPG,IND,T,PBAR,EPLN)
```

where

NPG,XPG,T,PBAR : see AIRPR1 and AIRPR2
 NTOT : total number of components. INPUT
 NPRIM : number of primary components. INPUT
 SV,CPRV : specie enthalpy, entropy and spec. heat. INPUT
 X : mole fraction. INPUT/OUTPUT
 EPLN : relative accuracy of calculation of mole fraction.
 IND : index table to refer to the row number in NGG,XPG.
 INPUT

ATOMPL

Call for the subroutine is:

```
CALL ATOMPL(NTOT,NPRIM,NSPEC,NTEMI,IFLAG,NP,NBRKW,NPT,NCHRG,IND,XPRIM,XPRAT,XMOL,POTX,SIGX,HS0,NPG,XPG,HMX,XNMX,PBAR,TE,TH,ENTHM,ENTRM,XMOLM,DENS,VISCOS,XKTH,XKTE,GAMEH,ELCOND,PLFR,GAUSS)
```

where

NTOT,NPRIM,NPG,XPG,PBAR,TE,TH : see APRHLP
 NSPEC : number of element specie. INPUT
 NTEMI : direction of change of temperature (increasing: NTEMI = 1; decreasing: NTEMI = -1). INPUT
 IFLAG : an index (IFLAG = -1: read data through RDITAB and RDECCS; IFLAG = 0: initialize guess values and other variables; and IFLAG = 1: normal calculation). INPUT
 NP : printing index (=1: only final results; = 0: no print; = -1: print all values except input data; and = -2: print everything). INPUT
 NBRKW : = 0

NPT : table of data input code for different components used
 by RDECCS. INPUT
 NCHRG : initial charges of NSPEC elements
 IND : index table used by Subr. TTGPTP
 XPRIM : guess mole fraction of primary comp. (incl. elec.)
 XPRAT : ratio of mole fraction of elements
 XMOL,POTX,SIGX,HSO : for each element mole mass, Lennard-
 Jones potential function, molecular diameter, and heat
 of formation at absolute temperature. INPUT
 ENTHM : mix. enthalpy (MJ/kg). OUTPUT
 ENTRM : mix. entropy (MJ/kg-K). OUTPUT
 XMOLM : mix. mole mass (kg/kmole). OUTPUT
 DENS : mix. density (kg/m³). OUTPUT
 VISCOS : dyn. viscosity coeff. (kg/ms). OUTPUT
 XKTH : total heavies heat cond. coeff. (kW/mK). OUTPUT
 XKTE : total electron heat cond. coeff. (kW/mK). OUTPUT
 GAMEH : coll. frequency (s⁻¹). OUTPUT
 ELCOND : elec. cond. (A/Vm). OUTPUT
 PLFR : plasma freq. (s⁻¹). OUTPUT
 GAUSS : magnetic induction (Gauss). INPUT. (If required,
 ECYCF = cyclotron freq./coll. freq. can also be ob-
 tained by changing the subr. arguments).

BROKAW

Call for the subroutine is:

CALL BROKAW(NIN,M1,M2,NMOL,IELEC,IND,XPG,WA,WB,VISCOS,XKCH)

This subroutine is an auxiliary subroutine for TTGPTP to use Brokaw mixing formulas for calculation of the transport properties, where there is at least one molecular component.

CRGCRS

Call for the subroutine is:

CALL CRGCRS(TREF,TH,TE,PBAR,XE,QBAR,Z1,Z2,NRANGE)

where

TE,TH : electron and heavy particles temperature, respective-
 ly. INPUT
 TREF : reference temperature (=TE, if at least one collision
 partner is electron; otherwise = TH). INPUT
 XE : electron mole fraction. INPUT
 Z1,Z2 : charge for collision partners.
 QBAR : collision cross-section (Ang²). OUTPUT
 PBAR : pressure (bar). INPUT

Internal Variables:

NRANGE: Out of range indicator requested

Pi: 3.14159265358979
 QB(11): Internal values of collision cross section
 TEXA(26,11): Attractive coulomb potential omega integrals
 TEXR(26,11): Repulsive Coulomb potential omega integrals
 TS: Dimensionless Temperature this corresponds to X when
 AILGTB is called to interpolate values
 TTS3(26): First column of Repulsive Coulomb potential
 tables. This corresponds to XT when AILGTB
 is called to interpolate values.
 TTS4(26): First column of attractive Coulomb potential
 tables. This corresponds to XT when AILGTB
 is called.
 XA: Several assignments:
 1) A portion of the denominator of the debye length
 2) Dummy variable = \ln of XL
 3) Area of influence for shielded coulomb potential
 XB: Dummy variable = XL^{**2}
 XL: dummy variable = $4*TS$
 ZZ: product of charges

DETERM

Call for the subroutine is:

```
CALL DETERM(A,MXD,N,DETL,SIGN,IER)
```

where

A(MXD,MXD) : coefficient matrix. INPUT
 N : order of A. INPUT
 DETL : natural logarithm of absolute(determinant). OUTPUT
 SIGN : sign of determinant. OUTPUT
 IER : output error flag (=0, no error). OUTPUT

ECMTTP

Call for the subroutine is:

```
CALL ECMTTP(I,ITC,IER,NP,PBAR,TE,TH,XMASS,XE,XI,XII,XIII,
  XN,EIGT,ENTHT,ENTRT,XMOLT,HJ,XKHR,XKER,XEDTE,XEDTH,EPS,NITMX
,NSAHA,NDI)
```

where

I : minimum ionization level for input, but the actual
 ionization level for output(=1 for neutrals).
 INPUT/OUTPUT
 ITC : number of iteration done. OUTPUT
 IER : output error code (=0, no error). OUTPUT
 NP : printing index (>0, no print; = 0, final values). INPUT
 XMASS : mole mass of the heavy particle. INPUT
 XE,XI,XII,XIII : mole fractions of electrons and heavy

	species.	INPUT/OUTPUT
XN :	number density (m^{-3}).	OUTPUT
ENTHT,ENTRT,XMOLT :	enthalpy (J/kmole), entropy(J/kmole-K) and mole mass of the mixture plasma.	OUTPUT
HJ :	individual component enthalpy (kJ/kmole).	OUTPUT
NITMX :	max. number of iteration.	INPUT
NSAHA :	index for using Kerrebrock/Veis equilibrium formula (=0, use Veis formula).	INPUT
NDI:	index number for using "lowering of ionization potential" (=0, lowering enabled).	INPUT
EPS:	relative tolerance for equilibrium composition calculation	INPUT

Internal Variables

A: Dummy variable = $(1-i)/i$
 AA: Several assignments
 1) Dummy variable for upper energy limit (ELIM)
 2) Dummy variable for ionization potential (EIT(NENER))
 3) Dummy variable for electron mole fraction (XE)
 4) Dummy variable for heavy mole fraction (XII)
 AB: Working variable for $\ln(i-1/i)$
 AE: Dummy variable = $XE+XI+XII$
 ALXE: Natural log of electron mole fraction
 ALX2I: Natural log of XII
 AI: Dummy variable for Ionization level in REAL format
 B: Dummy variable for $(1+i)/i$
 DBK(2): delta b from equation (16) in reference [5]
 DFS: Difference between actual and desired values for the Newton iteration method of solving implicit relations
 EFACT: Energy conversion factor to convert to °K
 IDIM = 1: EFACT = °K/J
 IDIM = 2: EFACT = °K/cm**(-1)
 IDIM = 3: EFACT = °K/°K
 IDIM = 4: EFACT = °K/eV
 EIT(NENER): Array of Ionization potential of each energy level
 EIGT(NENER): Sum of all lower ionization potentials up to the current energy level.
 ELIM: Maximum excitation Energy that has to be considered to evaluate the partition function
 FS: Implicit function for electron mole fraction used in Newton's method solution
 FSD: Derivative of FS for Newton's method solution
 GKK(2,2): Matrix represented by equation (16a) in reference [5]
 GT(NT): Statistical weight of E(i); known as g(i) in statistical thermodynamics; the degeneracy of an energy level
 IDIM: Energy units code
 J = 1
 cm**(-1) = 2
 °K = 3

ev = 4
 IJ: Loop variable for newton method
 IMAX: Maximum ionization level
 IMIN: Minimum ionization level
 IMN1: Dummy Variable for I
 K: Loop variable representing the current g_i, E_i pair for the current ionization level
 K1: Upper limit of DO loop corresponding to NENER-1
 K2: Two assignments
 1) Loop variable
 2) Flag for the number of ionization levels
 KA: Loop variable representing the current energy level
 KB: The current energy level + i-1
 KC: The number of g_i, E_i pairs in the energy level corresponding to KB
 KIT: Dummy variable for the number of iterations performed
 NAA: Flag for AA if electron mole fraction is within limits
 NENER: Number of ionization levels
 NT: Number of g_i, E_i pairs in each ionization level
 NTEST: Flag for deltas(=0, small delta, = 1, large delta)
 ST(3): Saha functions for each heavy species
 TA: Working Variable for Temperature Ratio
 TE: Electron Temperature
 TH: Heavy Particle Temperature
 Third: Decimal value for 1/3
 UT(NT,NENER): E_i value for each energy level
 XA: 2 assignments
 1) Dummy variable for UT
 2) coefficient in calculation of XEDTE, XEDTH
 XB: two assignments
 1) Dummy variable for individual component enthalpy, HJ
 2) coefficient used in calculating XEDTE, XEDTH
 XC: coefficient used in calculating XEDTE, XEDTH
 XD: coefficient used in calculating XEDTE, XEDTH
 XEDTE: Partial derivative of XE w/ respect to TE
 XEDTH: Partial derivative of XE w/respect to TH
 XEN: New guess for electron mole fraction in newton iteration
 XEQ: Equilibrium electron mole fraction
 XEX: Dimensionless energy = $-E_i/KT_e$
 XEX1: $\exp(-E_i/KT_e)$
 XKER: Intermediate value of reactive heat conductivity for electrons.
 XKHR: Intermediate value of reactive heat conductivity for heavy particles.
 XLD: Lowered mole fraction, maybe? (from lowering of ionization potential)
 XMASS: Molar mass of the heavy particle
 XMOLT: Mole mass of the mixture plasma
 XM: Dummy value for temperature ratio
 XN: Number density in m^{*-3}
 ZLN(3): Energy weighted partition function

ZT(3): Partition function

ELAT & ELATOM

Call for the subroutines is:

```
CALL ELAT(TE,QBAR,KS)
CALL ELATOM(TE,QBAR)
```

where

```
TE : electron temperature (K). INPUT
QBAR : electron-neutral collision cross-section. OUTPUT
KS : index for the neutral. INPUT
```

Internal Variables:

```
AA: REAL value of ICOUN
AAK: REAL value of ICOUN/2
AKB: Boltzmann's constant
AIN(25): Integrand of equation (35), reference (5)
AINI(5): Initial energy in electron-atom gas-kinetic range
AINTE: Integral in equation (35), reference [5]
AN: multiplier (by eV) to get dimensionless E/KT
ANIT: Dummy variable for initial energy in electron-atom gas
      kinetic range
AQ(25,5): Electron-Atom gas-kinetic collision cross sections
          for given range and level
DH: Dummy value for energy step size
DHI(5): Energy step size
E: Charge of an electron in coulombs
EV(25): Value of energy at a given step
GG: Dimensionless energy E/KT
I: Loop Variable
ICOUN: I don't see a use for this variable--ask Dr. Bose
IJ: Loop variable
IOE: Error Flag, but for what, I have no idea--ask Dr. Bose
J: Counter representing current electron-atom gas-kinetic
   level
JJ: Multiplicative counter
L: Counter for loop variable I + 1
M: Column number of collision matrix
MF(10): (i+1)!, where i = .1,2,..9
NELATL: Number of electron-atom gas-kinetic energy levels
NELAT: Dummy variable for NELAT
NOL: Dummy variable for NOV-1
NOM(5): Number of electron-atom gas-kinetic energy ranges
NOV : Dummy value for NOM
OBDMR: I Don't know, but a guess is the denominator term to
       convert s values of the Q matrix to array form.
OBNMR: I Don't Know, but a guess is the numerator term to
       convert s values of the Q matrix to the array
```

form.

OMF: Multiplication factor $\equiv(m+1)!$

Pi: 3.14159265358979

Q(25): Electron-Atom Gas-Kinetic Cross section for a given range and level--each element represents a different range in the same level

S: Floating Point version of M

SEVEN: Even element integrands

SODD: Odd element integrands

TE: Electron Temperature

XEX: $\exp(-E/KT)$

EQUCOM

Call for the subroutine is:

CALL EQUCOM(NIN,NTOT,NPRIM,DLNMX,XJ,XLNX,XLNKX,XNU,HIJ)

where

NIN : dimension of arrays (must be \leq NTOT). INPUT

NTOT : number of total components. INPUT

NPRIM : number of primary components. INPUT

DLNMX : relative tolerance. INPUT

XJ : mole fraction. OUTPUT

XLNX : guess value of logarithm of primary mole fraction. INPUT

XLNKX : logarithm of equilibrium constant. OUTPUT

XNU : chemical valency matrix. INPUT

HIJ : compatibility equations matrix

FCMTTP

Call for the subroutine is:

CALL FCMTTP(I,NDI,NSAHA,PBAR,TE,TH,XMASS,XE,ENTHT,ENTRT,XMOLT,XEQ,XNQ,ENTHTQ,ENTRTQ,XMOLTQ)

where the arguments are equivalent of ECMTTP, except that the last letter Q refers to equilibrium values.

INSPPR

Call for the subroutine is:

CALL INSPPR(INDEX,PBAR,Z,Q)

where

INDEX : signifies type of collision ($=1,i-1$; $=2,(i+1)-(i+1)$);

=3,e-e; =4,i-e; =5,(i+1)-e; =6,i-(i+1)); (i=ionization index; value of INDEX refers to row number of Z). INPUT

PBAR : pressure(bar). INPUT

Z : auxiliary array, for which columns in each row denote:
(col.1:ref.temp.,col.2:ref.mole mass,cols.3 &

4:charge;

col.5:heat cond.coeff.,col.6:viscos.coeff.,col.7:diff. coeff.). INPUT/OUTPUT

Q : collision cross-section (for details of locations, see IONAT). INPUT

IONAT

Call for the subroutine is:

CALL IONAT(TH,PROPT,QBAR,NRANGE)

where

TH : heavy particles temperature (K). INPUT

NRANGE : out of range indicator requested. INPUT

PROPT:species properties array (col.1:heavies mole mass;
col.2:neutral particles dia.;col.3:Lennard-Jones
potential;cols.4 to 11:data for use of Monchik
tables).INPUT

QBAR : collision cross-section $Q^{(1,s)}$ (ang.²) with column-
wise distribution of (1,s) as follows:

I=	1	2	3	4	5	6	7	8	9
(1,s)=	(1,1)	(1,2)	(1,3)	(1,4)	(1,5)	(1,6)	(1,7)	(2,2)	(2,3)
I=	10	11	12	13	14				
(1,s)=	(2,4)	(2,5)	(2,6)	(3,3)	(4,4)				

In above, all columns are not filled up by all the subroutines.
These are given in the following:

col. no.	1	2	3	4	5	6	7	8	9	10	11	12	13	14
Subr.:														
LENJON	x	x	x	x	x			x	x	x				x
MONCH	x	x	x	x	x			x	x	x				x
IONAT	x	x	x	x	x	x	x	x	x	x				
CRGCRS	x	x	x	x	x	x	x	x	x	x	x	x	x	x
ELATOM	x	x	x	x	x	x	x							

Internal Variables:

A: Constant = propt(10)
 B: Constant = Propt(11)
 Beta(8): Summation, determined from equation (36a) in
 reference [5]
 Eta(8): Summation, determined from equation (36a) in
 reference [5]
 Phi1: Potential value #1 (propt(6))
 Phi2: Potential value #2 (propt(8))
 R01: Radial position #1 (Propt(7))
 R02: Radial Position #2 (Propt(9))
 QBA(14): Monchik Cross section #1
 QBB(14): Monchik Cross Section #2
 XA: Dummy Variable for ln (TH/MH)

LENJON

Call for the subroutine is:

CALL LENJON(TH,POT,SIGMA,QBAR,NFL,NRANGE)

where

TH,QBAR,NRANGE : see IONAT
 POT : Lennard-Jones potential parameter (K). INPUT
 SIGMA : molecular diameter (ang.). INPUT
 NFL : out of range flag. OUTPUT

MOLGAS

Call for the subroutine is:

CALL MOLGAS(NP,NPT,NINI,KHS,NHS,NCP,NTOT,NPRIM,IFLAG,NBRKW,
NHS1,IND,NPG,XPG,HMX,XNMX,TC,PBAR)

where

NP : optional printing index(=0,-2,-1,1 for no printing, all
 printing, all printing except input data, only final
 results). INPUT
 NPT(NINI,2) : reading from PLASMA2.DAT for NINI number of
 gases; rowwise col.1: species code ICODE, col. 2: row
 no. of (NPG,XPG). INPUT
 KHS(NHS1,2) : NHS (=NHS1.LE.5) values of enthalpy-entropy
 data are to be calculated and stored (in
 addition to directly read from PLASMA2.DAT)
 for atom and ion (referred to by KF (for atoms
 only) and KT in NPG table, referred by the two
 column values per row in KHS). INPUT
 NCP : total number of spec. heat to be computed. INPUT
 NTOT,NPRIM : total number of components, prim.comp. INPUT
 IFLAG : initialize also, if IFLAG=0. INPUT

NBRKW : use Brokaw mixing formula, if NBRKW = 1. INPUT
 IND(NTOT) index for current data (compatible with NPG)
 NPG,XPG : see ATOMPL
 TC : current temperature (K). INPUT
 PBAR : pressure (bar). INPUT

Output results are obtained with the help of COMMON /RESULT/ as follows:

ENTHT : mix. enthalpy (MJ/kg)
 ENTRT : mix. entropy (MJ/kg-K)
 XMOLT : mix. mole mass (kg/kmole)
 VISCOS : dyn. viscosity coeff. (kg/ms)
 XKT : total heat cond. coeff. (kW/mK)
 DENS : mix. mass density (kg/m³)
 DENLG = Log10(DENS)
 PLFR : plasma freq. (s⁻¹)
 GAMEH : coll. freq. (s⁻¹)
 PRAN = Prf: frozen Prandtl number
 ELCOND : elec. cond. (A/Vm)
 CPEFF : effective spec. heat (MJ/kg-K)
 RATIO = cycl.freq./coll.freq. (calculated on the basis of
 the value of GAUSS (magnetic induction in Gauss) as INPUT)
 XT : mole fraction of different specie

MONCH

Call for the subroutine is:

CALL MONCH(TH,PHIO,RO,QBAR,NFL,NRANGE)

where

TH,QBAR,NFL,NRANGE : see LENJON
 PHIO,RO : species parameter for using Monchik tables. INPUT

Internal Variables:

ALPHA: Collision parameter = $\ln \phi_0/kT$; corresponds to x when
 AILGTB is called
 FLS(9): Value in denominator of equation (34b) in reference
 [5]
 Pi: = 3.14159265358979
 QB(9): Internal values of collision cross section
 TMONCH(50,9): Exponential repulsive potential omega
 integrals
 TTS2: First column of Monchik Tables. Corresponds to x_t
 when AILGTB is called
 XA: effective cross sectional area

OUTPUT

Call for the subroutine is:

CALL OUTPUT

PARTI

Call for the subroutine is:

```
CALL PARTI(NCHRG,KF,TE,TH,XE,PBAR,XMOL,HSPR,SSPR,ZEXC,EION,
EIONC)
```

where

```
NCHRG : charge index INPUT
KF : column number of (stat.weight, excit.energy)
TE,TH,XE,PBAR,XMOL : elec.temp.,heavies temp.,elec.mole fra
      ction,pressure(bar),heavies mole mass. INPUT
HSPR,SSPR : (e thalpy,entropy)/universal gas const. OUTPUT
ZEXC : excitation partition function. OUTPUT
EION,EIONC : ioniz. energy, total ioniz. energy (from ground
      level). OUTPUT
```

RDECCS

Call for the subroutine is:

```
CALL RDECCS(INPUT,NP,ICODE,KF,KS,KT)
```

where

```
INPUT : input channel unit no. INPUT
NP : optional print, if NP=0. INPUT
ICODE : species code no. (for PLASMA2.DAT). INPUT
KF,KS,KT : column numbers (for storing input data). INPUT
```

RDITAB

Call for the subroutine is:

```
CALL RDITAB
```

Internal Variables

```
I: Loop variable
Title(72): Dummy variable for the title of the type of
      table
TEXA(26,11): Attractive coulomb potential omega
      integrals
TEXR(26,11): Repulsive coulomb potential omega
      integrals
TLEN(82,9): Lennard Jones 6-12 Potential Omega
      Integrals
TMONCH(50,9): Exponential repulsive potential omega
      integrals
TTS1(82): First column in Lennard Jones tables
```

TTS2(50): First column in Monchik tables for
exponential repulsive potential
TTS3(26): First column in repulsive coulomb potential
tables
TTS4(26): First Column in attractive coulomb potential
tables

RDSEEN

Call for the subroutine is:

CALL RDSEEN

Internal Variables:

AINI(NELATL): Initial energy in electron-atom gas-kinetic
range

AQ(NOV,NELATL): electron-atom gas-kinetic collision cross
section for a given range and level.

DHI(NELATL): energy step size

EIT(NENER): Ionization potential in cm, (see the CRC
handbook of Chemistry and Physics, pp. 10-210 to
10-211 in 1991 version.)

GT(NT(I),NENER): degeneracy of each energy level(g, value)
for each ionization level.

I: Loop variable (This subroutine only)

IC: Flag for the gas used

=1, argon
=2, Helium
=3, Neon
=4, Xenon
=5, Krypton

ICT: Gas code read from data statement

=1, Helium
=2, Neon
=3, Argon
=4, Krypton
=5, xenon

IDIM: energy dimension code

J = 1
cm**(-1) = 2
°K = 3
ev = 4

NCODE: Code number of gas

=1, Helium
=2, Neon
=3, Argon
=4, Krypton
=5, xenon

NCARD: total number of lines of data for each gas

NCARD = NCARDE+NCARDC+NCARDP+2

NCARDC: number of lines of data in Part II of Plasma2.Dat

for each gas
 NCARDE: number of lines of data in Part I of Plasma2.Dat
 for each gas
 NCARDP: number of lines of data in Part III of Plasma2.Dat
 for each gas
 NELATL: Number of electron-atom gas kinetic energy levels
 NENER: Number of ionization levels
 NENP: Number of enthalpy(MJ/mole) and Entropy(MJ/kMol-°K)
 values for temperatures up to 15000 K in 3 ranges
 15000-6000 K : 500 K intervals
 6000-3000 K : 200 K intervals
 3000-400 K : 100 K intervals
 also at 298.15 and 0 K
 NOM(NELATL) : Number of electron-atom gas kinetic ranges
 NOV: Number of ranges in current electron-atom gas-kinetic
 energy level
 NT(NENER): number of g.,E. pairs in each ionization level
 PRO(11,5): Table of properties for the 5 noble gases read
 in from a data statement
 PROPT(11): Gas properties for one gas (Determined based on
 IC)
 UT(NT(I),NENER): E_i value for each ionization level

SOLEQ

Call for the subroutine is:

CALL SOLEQ(R,A,MD,N,DET)

where

R(MD) : right hand side vector (replaced by result). INPUT
 A(MD,MD) : coefficient matrix (destroyed). INPUT
 N : number of equations (N.LE.MD). INPUT
 DET : determinant. OUTPUT

TPSSIP

Call for the subroutine is:

CALL TPSSIP(I,XE,XI,XII,PBAR,TE,TH,PROPT,ELCOND,XKCE,XKCH,
 XMUT,XKRE,XKRR,XKHR,XKER,DAMB,Q,Z,GAMEH,NRANGE)

where

I : ionization index (=1 for neutrals). INPUT
 XE,XI,XII : mole fraction of electrons and ions. INPUT
 PBAR,TE,TH : pressure(bar), elec.temp.,heavies temp. INPUT
 PROPT,Q,Z,NRANGE : see IONAT and CRGCRS. INPUT
 ELCOND : elec. conductivity (amp/volt-m). OUTPUT
 XKCE,XKCH : heat cond. coeff. (by pure conduction) for elec.
 and heavies, respectively (kW/mK). OUTPUT

XKRE,XKRRH : respective reactive heat cond. coeff. OUTPUT
 XMUT : viscosity coeff. (kg/ms). OUTPUT
 XKHR,XKER : intermediate values from ECMTPP.
 DAMB : ambi-polar diff. coeff. (m²/s). OUTPUT
 GAMEH : electron-heavies coll. freq. (s⁻¹). OUTPUT

Internal Variables:

AI: REAL equivalent of

1) i-1

2) i

ASJK: A-star (j,k) used in calculating viscosity and thermal conductivity

BSJK: B-Star (j,k) used in calculating thermal conductivity

C1,C2: I don't know. Ask Dr. Bose

DEE: 4th order electron-electron diffusion coefficient

DET: Thermo-diffusion coefficient

DTL1: ln of QA

DTL2: ln of QB

DTL3: ln of QC

DTL4: ln of QD

IER1: Output error flag in calculating QA

IER2: Output error flag in calculating QB

IER3: Output error flag in calculating QC

IER4: Output error flag in calculating QD

IFL: Don't know. Ask Dr. Bose

IFLAG: Dummy value for NIN used to determine type of cross-section in if-then statements

IB1: Dummy variable for row of Z

IBIG: Loop variable for row of Z

J: Loop variable for Row of QB

J1: Dummy value for row of QB

J2: Dummy value for row of QB

JA: Loop variable for row of Z

JB: Loop variable for column of Z,Q

K: Loop variable for column of QB

K2: Dummy variable for column of QB

NIN(6): Flag for what kind of Collision cross section to use.

1=> Lennard Jones 6-12 potential

2=> Monchik Tables

3=> Charge transfer cross section for ion-atom collisions

4=> Attractive repulsive coulomb potential

5=> Electron-atom cross section

NRANGE: Out of range indicator for interpolation of tables

PEAR: Pressure in Bar

PHI: Value used in calculating exponential repulsive potential cross sections

POT: Dummy value used in calculating Lennard Jones 6-12 Potential cross sections

PROPT(1): Molecular Mass of Heavy particles

PROPT(2): Diameter of neutral particles in angstroms

PROPT(3): Lennard-Jones 6-12 potential
 PROPT(4-12): Data for use in Monchik Tables
 Q: Collision cross section
 QA(4,4): 4th order Sonine Polynomial expansion in matrix form
 QB(3,3): First minor of QA
 QC(3,3): 5th minor of QA
 QD(3,3): 6th Minor of QA
 R0: Radial position for use in Monchik Tables
 SIGMA: Dummy value for diameter of neutral particles in angstroms
 SIGN1: Sign of QA
 SIGN2: Sign of QB
 SIGN3: Sign of QC
 SIGN4: Sign of QD
 TR: Temperature Ratio
 TREF: Reference temperature used in calculation of collision cross sections
 U1,UY,UZ: I don't know. Ask Dr. Bose
 XA: 1) weighted heavy particle cross section
 2) Dummy variable for XI,XII
 XE: Electron Mole fraction
 XK: I don't know. Ask Dr. Bose
 XKD: Correction to XKCE
 XI,XII,XIII: mole fractions of three heavy species being examined. XI could be either neutral if $I = 1$, or an ion mole fraction if $I > 1$.
 XMLR: Reference molecular mass
 XN: Number density in m^{-3}
 XTQ: SQRT(TE)
 XXMU,YK,YXMU,ZK,ZXMU: I don't know, ask Dr. Bose
 Z(6,7): Auxiliary matrix
 col 1: reference temperature
 col 2: reference molecular mass
 col 3,4: charge of colliding partners
 col 5: heat conductivity coefficient
 col 6: viscosity coefficient
 col 7: Diffusion coefficient
 row 1: heavy species 1-heavy species 1 collision
 row 2: heavy species 2-heavy species 2 collision
 row 3: electron-electron collision
 row 4: heavy species 1 - electron collision
 row 5: heavy species 2 - electron collision
 row 6: heavy species 1-heavy species 2 collision

For the modifications made for microinstabilities, the following variables were also used:

CALDOCON: effective conductivity calculated by mean free path formula (used by Caldo and Choueiri)
 COND: classical conductivity calculated by mean free path formula

DEEAN: effective electron-electron diffusion coefficient
 DETAN: Effective thermo-diffusion coefficient
 effcl: ratio of effective to classical resistivity
 elcond: effective electrical conductivity
 elcyc: electron cyclotron frequency in radians/sec
 IERAN1: Output error flag in calculating |QAAN|
 IERAN2: Output error flag in calculating |QBAN|
 IERAN3: Output error flag in calculating |QCAN|
 IERAN4: Output error flag in calculating |QDAN|
 ji: loop variable for collision type
 ki: loop variable for cross section type
 Hall: electron Hall parameter
 GAMANP: anomalous momentum exchange collision frequency
 QAAN: Sonine polynomial expansion for effective collision
 cross sections in matrix form
 QAN: effective collision cross section
 QANP: anomalous momentum exchange collision cross section
 QBAN(3,3): First minor of QAAN
 QCAN(3,3): 5th minor of QAAN
 QDAN(3,3): 6th Minor of QAAN
 SIGNAN1: Sign of |QAAN|
 SIGNAN2: Sign of |QBAN|
 SIGNAN3: Sign of |QCAN|
 SIGNAN4: Sign of |QDAN|
 vthe: electron thermal velocity
 vthi: ion thermal velocity

TTGPTP

Call for the subroutine is:

```
CALL    TTGPTP(NN,M1,M2,M3,IFL,TE,TH,PBAR,VISCOS,XKCH,XKCE,
GAMEH,ELCOND,DEE,DET,NPG,XPG,WA,WB,WC,WD,GAUSS,ECYCF,RATIO,
PLFR,IDN)
```

where

IDN(NN) : index for different species (to refer to NPG,XPG).
 INPUT
 NPG(M1,4),XPG(M1,8): see ATOMPL. INPUT
 (WA,WB)(M2,M2),(WC,WD)(M3,M3): working locations.
 TE,TH,PBAR,XKCH,XKCE,GAMEH,ELCOND : see TTSSIP.
 VISCOS : viscosity coeff. (kg/ms). OUTPUT
 DEE,DET : electron molar and thermo-diff. coeff. OUTPUT
 GAUSS : magnetic field (Gauss). INPUT
 ECYCF : cyclotron frequency. OUTPUT
 RATIO : ratio of cyclotron to collision freq. OUTPUT
 PLFR : plasma frequency. OUTPUT

XEGRDT

Call for the subroutine is:

CALL XEGRDT(NCHRG,NSAHA,TE,TH,XE,ENER,XEDTE,XEDTH)

where

NCHRG : charge index. INPUT
 NSAHA : Kerrebrock(.NE.0)/Veis(=0) formulation to be used.
 TE,TH,XE : elec.temp.,heavies temp.,elec.mole frac. INPUT
 ENER: ioniz. energy (K). INPUT
 XEDTE,XEDTH : partial derivative of XE with respect to TE
 and TH. OUTPUT